The atomic and electronic structure of contaminants at the mineral-fluid interface

by

Sarah Marie Walker

A dissertation submitted in partial fulfillment
of the requirements for the degree of
Doctor of Philosophy
(Earth and Environmental Sciences)
in The University of Michigan
2017

Doctoral Committee:

Professor Udo Becker, Chair
Professor Joel D. Blum
Assistant Professor Brian Robert Ellis
Professor Donald Jason Siegel

Sarah Marie Walker

smwalk@umich.edu
ORCID ID: 0000-0002-6726-3142

ACKNOWLEDGEMENTS

First and foremost I would like to thank my advisor, Udo Becker, for the opportunity to join his group and for his continued guidance and support over the past few years. Udo has always been patient with me and has helped me develop invaluable critical thinking and problem solving skills, not to mention creative ways to get the job done. I would also like to thank my committee members, Joel Blum, Brian Ellis, and Don Siegel, for their thoughtful feedback and advice along the way.

I am especially grateful for all of my lab mates past and present: Ke Yuan, Sandy (Fernando) Taylor, Will Bender, Ben Gebarski, YoungJae Kim, Peter Cook, Evan Killeen, Saumitra Saha, Krish Arumugam, Kate Turner, and Sulgiye Park. Thank you for the many lunch outings, help with experiments, inspiration, and endless encouragement. Special thanks goes to Maria Marcano for keeping all of us organized and safe and for all of her help in the lab. She has been a great mentor for me. Gordon Moore and Jerry Li have provided tremendous support with my analyses EMAL, and thank you to Greg Dick for the generous use of his lab.

Many thanks to our department administrators and staff, especially Nancy Kingsbury for her help with finances and to Anne Hudon for her many words of wisdom; thank you to Mike Messina for answering all of my computing questions; and thank you to Bill Wilcox for his dedication to this department and literally making things run smoothly. Additional thanks to Joel and to Adam Simon for having me as a GSI at Camp Davis; I am exceedingly grateful for two summers in the Tetons.

It has been a pleasure sharing an office with Will and Sean the past two years, and I am lucky to have a great group of friends (and climbing partners) in the department. Finally, I would also like to thank Sam Haugland, my parents, Bruce and Betsy, and the rest of my family for their unconditional love, encouragement, and support. Thank you all very much!

TABLE OF CONTENTS

LIST OF TABLES

LIST OF FIGURES

LIST OF APPENDICES

ABSTRACT

The mobility of environmental contaminants is largely controlled by chemical reactions at the mineral-fluid interface. How a contaminant interacts with a mineral surface is fundamentally dependent on the molecular-level structure and properties of both the contaminant and the mineral surface. This dissertation explores different types of adsorption/incorporation processes and contaminant species (U, Np, Cr, and an organometallic compound as a proxy for oil) in order to understand specific mechanisms that may lead to contaminant (im)mobilization at the mineral-fluid interface. New applications of high-resolution experimental approaches and molecular modeling are developed in order to achieve a detailed understanding of mineral-fluid interface reactions.

Contaminants that are structurally incorporated into a host mineral remain immobilized until mineral dissolution, which has significant implications for the long-term sequestration of mobile contaminants. Chapter 2 describes a new method to model the incorporation aqueous uranium U(VI) and neptunium Np(V) into carbonate and sulfate minerals. Here, we use quantum mechanics to calculate the equilibrium energetics and thermodynamics of incorporation reactions and to consider the structural and electronic changes in the host mineral. U and Np incorporation is more likely to occur at crystallographic defect sites, such as vacancies or impurities. It was also found that the ionic radius of the replaced cation is not necessarily an indicator (as it is often used) of improved incorporation energies due to the influence of hydration.

Dissolved contaminants may also be immobilized through redox reactions catalyzed by mineral surfaces. The interaction between chromium (Cr) and the surface of the Fe(II)-bearing mineral magnetite, $Fe(II)Fe(III)_2O_4$, as an example catalyst, are investigated using electrochemical atomic force microscopy (Chapter 3). With this method, the reductive precipitation of Cr on the magnetite surface is imaged over time as a function of redox potential and pH of the solution. The redox transitions between Cr(III) and Cr(VI) at pH 7 are in agreement with the Eh conditions predicted from thermodynamic calculations, yet these predictions break down at more extreme pH conditions (pH 3 and 11), demonstrating the need for more robust thermodynamic databases of contaminant speciation.

Mineral surface wettability, which describes whether a surface is hydrophilic (water-wet) or hydrophobic (so-called oil-wet), determines the distribution and mobility of oil in contaminated soils and groundwater and in hydrocarbon reservoirs. The adsorption of the polar components of oil or other surface-active agents, such as hexamethyldisilazane ($(CH_3)_3SiNHSi(CH_3)_3$, HMDS), can result in a change in wettability and how easily oil can be extracted from a particular formation. Using calcite as a substrate, changes in the mineral surface structure and surface potential are observed as the calcite surface undergoes wettability alteration from water-wet to oil-wet. For the first time, surface potential measurements were used to interpret how mineral surfaces react to wettability alteration. Atomic force microscopy and computational modeling reveal that the surface structure, primarily edges and corner sites, determine where HMDS can be adsorbed on the surface. Therefore, calcite substrates with higher densities of edges and corner features, such as fine-grained chalk, may be more likely to become

mixed-wet or oil-wet after hydrocarbon migration. Molecular simulations reveal that the HMDS molecule is amphoteric and capable of interacting with both H^+ and OH^- surface groups, meaning that this molecule may function as an efficient wettability modifier at a range of pH conditions.

CHAPTER 1
Introduction

Minerals and, in particular, mineral surfaces are one of the most fundamental controls on the identity, distribution, and mobility of elements in the environment. The geochemical reactions that occur at the interface between the mineral surface and the surrounding fluid strongly affect how elements are transported and their ultimate fate in naturally occurring and anthropogenic systems. These surface reactions influence not only natural processes such as chemical weathering, soil development, nutrient cycling, ore deposit and hydrocarbon reservoir formation, but they also play a major role in industrial operations like flotation (and other ore processing technologies), enhanced oil recovery, and waste disposal and containment. The mineral-water interface has also become increasingly important in evaluating the dispersal and evolution of anthropogenic contaminants in environmental media. The improper disposal of hazardous wastes and accidental spillages (and, in some cases, elevated levels of naturally occurring contaminants) have lead to widespread contamination of soils, surface water, and groundwater in the United States and around the world (Bjerg et al., 2014; Callender, 2014; Watts and Teel, 2014). In order to accurately determine the possible fate of environmental contaminants and pollutants, it is crucial to characterize the interaction between contaminants and mineral surfaces and how mineral surfaces can mitigate the effects of contamination.

Contaminant migration in groundwater systems

EPA studies suggest that migration into groundwater is the principle release pathway of contaminants at hazardous sites (US EPA, 1998). While the inadequate storage of waste (*e.g.*, unlined landfills or leaky wastewater retention ponds) cause most instances of groundwater contamination, other point sources include mine tailings and tailings ponds, corroded underground oil tanks and pipelines as well as sewage and septic systems (Bjerg et al., 2014; Cozzarelli et al., 2014; Ta and Yan, 2014). Despite more modern regulations on these possible sources, accidental spills and legacy contamination still pose a significant hazard to many groundwater systems, which accounts for 37% of the public water supply and nearly 98% of water supplied to rural communities in the United States (Maupin et al., 2010). The environmental, ecological, and related human-health impacts of contaminated groundwater can persist for decades when contaminants migrate slowly through the subsurface and/or have slow rates of degradation. Particularly recalcitrant organic contaminants (for example, PCBs) and inorganic contaminants, such as metals and radionuclides (which are not biodegradable) can remain in the subsurface indefinitely; the risk associated with these compounds is only mitigated through their physical removal or through their transformation into a more stable, less toxic substance. Therefore, it is essential to understand the fundamental processes that govern what makes a contaminant more (or less) mobile and more (or less) toxic.

While the movement of contaminants through groundwater depends in part on advective, dispersive, and diffusive transport processes, geochemical reactions between the contaminant species, other fluids in the subsurface, and the minerals that comprise the aquifer can further accelerate or retard contaminant migration. Elements dissolved in

water exist as different chemical forms including cations, anions, neutral molecules or aqueous complexes. The specific compounds present in solution, also called the speciation, is regulated by local geochemical conditions (*e.g.*, pH, total organic carbon, the oxidation-reduction potential, temperature, and the concentration of other dissolved species, just to name a few). Under certain conditions, some contaminants will remain in solution as dissolved, mobile species, while other conditions allow for contaminants to form bonds and adsorb or precipitate onto mineral surfaces or transform into a less soluble phase and fall out of solution. The presence of other non-polar, organic fluids, which are commonly contaminants themselves, may further complicate a contaminant's speciation and solubility (Cozzarelli et al., 2014; Ta and Yan, 2014). Light non-aqueous phase liquids (LNAPLs) such as gasoline, benzene, or other hydrocarbons are less dense than water and therefore float on top of the water table, while dense non-aqueous phase liquids (DNAPLS), which include polychlorinated biphenyl (PCBs), chlorinated solvents, mercury, and extra heavy crude oil, sink below the water table until they reach an impenetrable aquitard or bedrock (Cozzarelli et al., 2014; Ta and Yan, 2014). These fluids, with physicochemical properties different than those of water, come into contact with mineral surfaces and affect how well the fluid "sticks" to a mineral surface, a property known as wettability. Wettability influences how easily fluids flow through pore spaces and how easily certain species can be removed from pore surfaces (through pumping for example) both in contaminated aquifers and in oil reservoirs deep beneath the surface.

Why study mineral surfaces

As described above, contaminated groundwaters are highly complex systems; in order to fully understand the processes that affect contaminant migration, information from the atomic scale is required. How a contaminant interacts with a mineral surface is fundamentally dependent on the molecular-level structure and properties of both the contaminant in question and of the mineral surface. It is therefore necessary to learn about small-scale phenomena in order to better control and design remediation programs and for more accurate risk assessment and management at the field scale. By applying nanoscale (10^{-9} m) techniques that tell us about the interface between solids and fluids, this dissertation explores the specific mechanisms that may lead to contaminant immobilization at the mineral-fluid interface.

The surfaces of minerals have properties that are intrinsically different than those of the bulk crystal. Minerals typically have a well defined, repeating periodic structure; however, the termination of a crystal at a surface results in surface atoms that are under coordinated relative to their bulk counterparts. So-called dangling bonds leave the valence electrons of these surface atoms unsatisfied and therefore highly reactive (Lannoo, 1990). Dangling bonds also produce a net charge and corresponding surface potential that strongly influences the behavior of dissolved species in the surrounding fluid and the fluid itself. Depending on the pH of the fluid, the surface charge will be positive, negative, or neutral if excess hydrogen ions (H^+) or hydroxide ions (OH^-) adsorb, or bond, with this surface. (Additionally, the pH where the number of H^+ and OH^- are equal and produce a neutral charge is termed the point of zero charge). The structure of the mineral at the surface also changes; surface "relaxation" occurs such that atoms at

the surface redistribute themselves in order to achieve a more energetically favorable geometric arrangement. In other words, the surface atoms change their position relative to their surrounding atoms to lower their overall energy. At the atomic level, mineral surfaces have topography that further influences their enhanced reactivity relative to the bulk mineral. Even when a mineral has perfect cleavage, the cleaved surface is typically far from flat. The classical terrace-ledge-kink (TLK) model describes an atom's position on the surface based on its bonding with neighboring atoms (Burton et al., 1951). While this model is based on assumption that are only valid under certain conditions, it is generally accepted that there are flat terraces, ledges (also called steps) where ions or molecules are added when a crystal is growing, kink atoms, and vacancies (De Yoreo et al., 2009). These different sites have slightly different geometries and reactivities, which control how elements are incorporated into the crystal structure or adsorbed onto the mineral surface (Paquette and Reeder, 1995).

Sorption processes at the mineral-fluid interface

When an ion, contaminant or otherwise, comes into contact with a mineral surface, there is a continuum of adsorption processes that may occur; a brief description of these adsorption processes follows here. Dissolved ions in aqueous solution are usually surrounded by a group of water molecules, known as a hydration sphere. An ion with its hydration sphere fully intact may become loosely associated with the surface (primarily through electrostatic interactions) in a process known as outer-sphere complexation, one of the weaker types of adsorption (Sposito, 1989). Comparatively, inner-sphere complexation takes place when part of the hydration sphere is lost, and the ion bonds directly with the surface. An inner-sphere complex may be monodentate, where the ion is

bonded with only one atom on the surface, or bidentate (bonded with two surface atoms) and is generally considered slightly more stable that outer-sphere complexation (Sposito, 1989). As a point of clarity, adsorption refers to individual ions/molecules, monolayers or thin films of ions/molecules attached to a surface while precipitation involves the formation of a secondary phase, which, in this case, is on top of another solid mineral substrate. Precipitation includes the growth of either crystalline or amorphous phases. For precipitation to occur, the concentrations of the solute ions must be great enough so that they is supersaturated with respect to the equilibrium solubility of the precipitating phase. Both adsorption and precipitation, collectively referred to as sorption, are possible mechanisms for contaminant immobilization. Once the contaminant is adsorbed or precipitated on the mineral surface, it is no longer free to move in solution; however, these processes are reversible should the local geochemical conditions change. On the other hand, contaminant ions that are structurally incorporated into a host mineral remain immobilized until mineral dissolution, which has significant implications for the long-term sequestration of mobile contaminants, such as radionuclides (Atkinson, 1985; Bruno et al., 2007). Incorporation, also known as coprecipitation, occurs when an impurity ion occupies a lattice site normally occupied by an ion of the host mineral. These foreign impurities result in a crystallographic defect in the mineral structure and are particularly important with relatively low concentrations of contaminants are present (such that it is unlikely that a contaminant-dominated phase will precipitate). Incorporation specifically refers to very minor or even trace amounts of impurity ions; when higher concentrations of impurities are present, this is usually considered a solid-solution.

Surface-catalyzed redox reactions

In combination with adsorption, another important class of geochemical reactions that can occur on mineral surfaces are electron-transfer reactions. Many inorganic contaminants, particularly transition metals and radionuclides like uranium (U) and neptunium (Np), as well as some organic contaminants are redox-active, which means that their speciation is sensitive to the oxidation-reduction potential of their environment. For these elements, solubility and mobility are often dependent on oxidation state. One relevant example of this type of redox-sensitive geochemical behavior is chromium. In reducing environments, chromium exists as a trivalent ion (Cr^{3+}), which is much less soluble and much less toxic than oxidized, hexavalent chromium (Cr^{6+}) that usually occurs as a very soluble (and mobile) oxyanion $CrO_4^{2-}{}_{(aq)}$ or $Cr_2O_7^{2-}{}_{(aq)}$. The mineral-surface mediated redox transformations between Cr^{3+} and Cr^{6+} are discussed in detail in Chapter 3. Petroleum hydrocarbons (including both high and low molecular weight compounds) and fuel oxygenates are also highly susceptible to oxidation via aerobic or anaerobic microbial biodegradation (Cozzarelli et al., 2014). Electron donors and acceptors available to promote redox reactions, *e.g.*, dissolved organic matter, sulfide (S^{2-}) or Fe(II)/Fe(III) are common in most aqueous environments; however, mineral surfaces are often needed to promote these redox reactions. Atoms at the surfaces of minerals may accept or donate electrons as active participants in the redox reactions, or the mineral surface may serve as a catalyst by facilitating electron transfer via an electron shuttle through the surface (Tessis et al., 1999; Becker et al., 2001; Vorlicek and Helz, 2002; Rosso and Becker, 2003). The chemical transformation of contaminants by means of

redox reactions on mineral surfaces illustrates another mechanism by which contaminants can be immobilized by interactions with minerals.

Dissertation outline and structure

The following chapters of this dissertation cover three different types of contaminant interactions with mineral surfaces: (Chapter 2) incorporation, (Chapter 3) reductive precipitation, and (Chapter 4) adsorption of organic molecules and wettability alteration. Although each contribution focuses on a different contaminant or molecule (which include U, Np, Cr, and an organometallic compound as a proxy for oil), the unifying concept is that these geochemical reactions are important mechanisms for changing the mobility of contaminants in solution (by causing a change in solubility or by changing the wetting preference of the surface). The methods used to investigate these processes include theoretical and experimental approaches (and a combination thereof) and, in some cases, are novel applications for studying the reactions that occur between contaminants and mineral surfaces.

Special methods applied to mineral surfaces

In order to study the atomic-scale processes at the mineral-fluid interface, we must implement approaches that can capture information at these very high spatial resolutions. In addition to the traditional methods used to identify minerals (*e.g.*, optical microscopy, x-ray diffraction, and electron microbeam techniques), mineral surface investigations call for special approaches that are surface sensitive, that is focus only on the top few nanometers of the sample. Since their development in the 1980s, scanning probe methods, chiefly atomic force microscopy (AFM), have become indispensable for characterizing the nanoscale topography and the atomic and electronic structures of

mineral surfaces (Binnig et al., 1986; Jupille, 2014). Atomic force microscopy does not rely upon the interaction of light with a sample, but instead uses a soft cantilever to "feel" the topography surface and measure the very small forces between the cantilever tip and the sample. With AFM, the sample surface is probed with an atomically sharp tip using a piezoelectric scanner. The tip is mounted on a flexible, reflective cantilever, whose location is monitored through a laser aimed towards the back of the cantilever and reflected over a photodetector. As the scanner moves back and forth and across the sample, interactions between the tip and the sample surface cause the cantilever to bend. This displacement corresponds to a deflection of the laser beam on the photodetector and is interpreted as a change in the topography. A distinct advantage of AFM for studying environmental systems is that experiments can be performed *in situ* with the mineral surface in contact with a fluid phase. This means that observations of the mineral surface can be made in real time under carefully controlled laboratory conditions. In addition to topography, other properties of the mineral surface can be resolved with AFM. Newly-developed applications of AFM to study redox reactions (Chapter 3) and surface potential in the context of oil adsorption (Chapter 4) are explored later in this dissertation.

One disadvantage of AFM is that this technique does not provide any chemical information about the surface. Consequently, complementary tools are frequently employed to understand the composition of mineral surfaces. X-ray photoelectron spectroscopy (XPS) and Auger electron spectroscopy (AES) have become two of the most widely used surface analytical techniques today (Hochella, 1995). XPS, which is available both commercially and at synchrotron sources, can provide information about the elemental composition, the local bonding environments, and the oxidation state of

surface atoms. AES also produces elemental compositions of mineral surfaces, but because an electron beam is used to probe the sample (which is easier to manipulate than an x-ray), the spatial resolution for AES is greatly improved from that of XPS (*i.e.*, analysis areas as small as 100s of Ångsroms, 10^{-10} m, for AES *vs.* 10s-100s of microns, 10^{-6} m, for XPS). The principles of AES and XPS are similar in that core electron vacancies are created (with either x-rays or electron beams), and the vacancy is subsequently filled by an electron from a higher energy level. The energy released from this electronic transition may be used to create a photon (which ejects a photoelectron, the basis of XPS) or may may be used to eject an electron from a higher energy level known as an Auger electron. These electrons have relatively low kinetic energies, so that only Auger electrons from surface or very near-surface atoms may be detected (Hochella et al., 1986). Although XPS and AES have limitations, such as the condition of ultra high vacuum environments, relatively high detection limits (~1% of the surface), the inability to measure H or He, and charging effects (AES), these techniques are crucial tools in mineral surface science and understanding the changes in composition and chemical state of surface species after mineral-fluid interactions. Both XPS and AES are used to characterize mineral surfaces before and after reactions with dissolved contaminants in Chapters 3 (XPS and AES) and 4 (XPS).

While high-resolution experimental techniques allow us to observe and analyze the products of reactions between mineral surfaces and contaminants in solution, computer-based molecular simulations fundamentally advance our understanding of the mechanisms that control mineral-fluid interface processes. Molecular modeling offers a higher degree of control and more access to the details of the reaction thermodynamics

and (sometimes) kinetics, resulting molecular or crystal structures, electronic and magnetic properties, and energetics (Wogelius and Vaughan, 2000). The basic premise behind this approach is calculating the total energy of the system under investigation based on the interactions between individual atoms (Cygan, 2001). In short, this may be done in two ways: molecular mechanics and quantum mechanics. Molecular mechanics is based on classical physics and depends on analytical expressions to describe the interactions between atoms. These expressions are parameterized by empirical values or even by quantum mechanical calculations. On the other hand, quantum mechanical methods calculate the energies and distributions of electrons by attempting solving the Schrödinger wave equation (with varying degrees of assumptions and approximations) (Tossell and Vaughan, 1992; Hochella, 1995; Wogelius and Vaughan, 2000). With quantum mechanics, we can calculate and predict a system's properties without relying on empirical parameters, which is why quantum mechanical calculations are sometimes called from *first-principles*. Models of mineral surfaces can be either a small cluster of atoms that retain the most important characteristics of the surface, such as edges or kink sites, (known as cluster models), or an infinite repeating unit that makes use of the two-dimensional periodicity of a real mineral surface (periodic models) (Tossell, 1995). Additionally, these models can be calculated as isolated gas phase ions/molecules or as a hydrated species (Cygan, 2001). A critical component of using molecular modeling to describe natural systems is validating the model results against experimental data. To do this, we must first identify what information from computational models and calculations can be compared with experimental results. Possible points of comparison include the structure and lattice parameters of the bulk mineral (measured with x-ray diffraction), the

bonding environment of the species adsorbed on the surface (XPS can confirm oxidation state and x-ray adsorption spectroscopy can identify specific coordination environments and nearest neighbor distances), and electronic configuration (which can be probed with conductivity experiments or XPS/ultraviolet photoelectron spectroscopy). Even so, one must be careful as it is difficult to verify if experiments have achieved equilibrium conditions and if experimental error is comparable to (or sometimes greater than) computational error. Chapters 2 and 4 demonstrate how quantum mechanical models are used to model how contaminants interact with mineral surfaces and how to reconcile this information with experimental observations.

Chapter 2: Uranyl (VI) and neptunyl (V) incorporation in carbonate and sulfate minerals: insight from first-principles

In Chapter 2, the incorporation of the radionuclide contaminants U and Np into sulfate and carbonate minerals is investigated using quantum mechanical modeling (Walker and Becker, 2015). Incorporation of chemical species into minerals plays an important role in governing the immobilization and release pathways of contaminants in low-temperature geologic environments. Additionally, U incorporation into carbonates has led to the development of U-series dating in corals and speleothems, which allows geochemists to reconstruct high-precision records of Earth's past (Bourdon et al., 2003; Dorale et al., 2004; van Calsteren and Thomas, 2005). Geochemists have studied and modeled incorporation reactions in relation to a variety of applications ranging from acid mine drainage to nuclear waste sequestration. Traditionally, incorporation has been modeled as a periodic, solid phase reaction, in which the source of the contaminant and the sink for the replaced host species are both solids. While solid source and sink phases can be present in nature, it is significantly more likely that a mineral surface interacts

with dissolved species in solution, *i.e.* hydrated ions. Furthermore, incorporation experiments may not reach equilibrium conditions within a reasonable amount of time, thus convoluting experimentally-derived equilibrium thermodynamics. To address this, this chapter details and applies a recently-developed method for quantum-mechanically modeling the incorporation of aqueous radionuclide contaminant species into a periodic mineral phase. We introduce a systematic series of reactions required to transform periodic solid sources and sinks to charged, aqueous species and calculate equilibrium energetics and thermodynamics of incorporation reactions. We also consider the structural and electronic changes in the host mineral upon incorporation of the radionuclide and provide a discussion of the limitations and possible errors associated with this approach. In summary, this chapter applies an improved method to model the incorporation of aqueous radioactive contaminants into solid mineral hosts. The description and comprehensive examples of this new approach can serve as a template for future incorporation studies.

Chapter 3: Imaging the reduction of chromium (VI) on magnetite surfaces using in situ electrochemical AFM

Chapter 3 examines the reductive precipitation of chromium (Cr) on the surface of the mixed-valence iron mineral magnetite (Walker et al., 2016). As mentioned, redox potential and solution pH play an essential role in governing the solubility and mobility of metal contaminants in aqueous environments, particularly for the metal contaminant Cr, which is typically soluble and toxic as Cr(VI) and insoluble and more benign as Cr(III). To study the redox-dependency of heterogeneous Cr precipitation, we have developed and applied a method to image the deposition of Cr(VI) on the surface of magnetite (Fe_3O_4) as a function of redox potential and pH. Electrochemical atomic force

microscopy (EC-AFM) is a type of redox-sensitive scanning probe microscopy in which *in situ* observations of a surface can be made in real time. Through precisely controlling the redox potential (using an electrode setup in the AFM reaction container), pH, and solution chemistry (by applying these parameters to the actual solution), we investigate morphological changes in the magnetite surface and measure growth kinetics of adsorbate formation along a given Eh/pH path. In addition, we have supplemented this technique with batch chemistry experiments to examine the amount of Cr removed from solution and surface sensitive spectroscopy (XPS and AES) to analyze the chemical composition of Cr precipitates on the surface.

Chapter 4: Understanding molecular-level mechanisms for wettability alteration on calcite through surface potential measurements and molecular simulations

Chapter 4 is a slight departure from Chapters 2 and 3 in that the focus is on how the mineral surface responds to the adsorption of a particular molecule. Mineral wettability, *i.e.*, whether a mineral is hydrophilic (water-wet) or hydrophobic (oil-wet), determines the distribution and mobility of oil in contaminated soils and groundwater and in hydrocarbon reservoirs. Wettability affects how oil flows through porous materials and is an important factor to consider when designing remediation projects or when extracting oil during the recovery process. Because wettability is dependent on many factors (*e.g.*, hydrocarbon composition, asphaltene content, pH, temperature, and pressure), predicting mineral wettability is often difficult. In Chapter 4, we look at changes that occur on the mineral itself, specifically changes in the surface structure and surface potential, when a mineral undergoes wettability alteration from water-wet to oil-wet. Our goal is to better understand the molecular-level processes involved and to identify trends that are useful for predicting wettability alteration of calcite under certain conditions. Nanoscale surface

imaging is combined with Kelvin probe force microscopy (KPFM) to characterize changes in topography and surface potential before (water-wet) and after treatment with a wettability modifier hexamethyldisilazane ($(CH_3)_3SiNHSi(CH_3)_3$, HMDS), which renders the calcite surface oil-wet. In order to achieve a true atomistic understanding not possible with most experimental approaches, computational modeling is used to identify favorable surface sites for HMDS adsorption, characterize the bonding between HMDS and the surface, and evaluate possible changes in the surface potential before and after wettability alteration.

References

Atkinson A. (1985) The time dependence of pH within a repository for radioactive waste disposal. *United Kingdom At. Energy Res. Establ. Rep. AERE-R117777*.

Becker U., Rosso K. M. and Hochella Jr M. F. (2001) The proximity effect on semiconducting mineral surfaces: a new aspect of mineral surface reactivity and surface complexation theory? *Geochim. Cosmochim. Acta* **65**, 2641–2649.

Binnig G., Quate C. F. and Gerber C. (1986) Atomic Force Microscope. *Phys. Rev. Lett.* **56**, 930–933.

Bjerg P., Albrechtsen H.-J., Kjeldsen P. and Christensen T. (2014) 11.16 – The Biogeochemistry of Contaminant Groundwater Plumes Arising from Waste Disposal Facilities. *Treatise on Geochemistry*, 573–615.

Bourdon B., Turner S., Henderson G. M. and Lundstrom C. C. (2003) Introduction to U-series geochemistry. *Rev. Mineral. Geochemistry* **52**, 1–21.

Bruno J., Bosbach D., Kulik D. and Navrotsky A. (2007) Chemical thermodynamics of solid solutions of interest in radioactive waste management. *OECD Nucl. Energy Agency Rep.*

Burton W. K., Cabrera N. and Frank F. C. (1951) The Growth of Crystals and the Equilibrium Structure of their Surfaces. *Philos. Trans. R. Soc. London A Math. Phys. Eng. Sci.* **243**, 299–358.

Callender E. (2014) 11.3 – Heavy Metals in the Environment – Historical Trends. In *Treatise on Geochemistry* pp. 59–89.

van Calsteren P. and Thomas L. (2005) Uranium-series dating applications in natural environmental science. *Earth-Science Rev.* **75**, 155–175.

Cozzarelli I. M., Mckelvie J. R. and Baehr A. L. (2014) 11.12 – Volatile Hydrocarbons and Fuel Oxygenates. In *Treatise on Geochemistry* pp. 439–480.

Cygan R. T. (2001) Molecular Modeling in Mineralogy and Geochemistry. *Rev. Mineral. Geochemistry* **42**, 1–36.

Dorale J. A., Edwards R. L., Alexander E. C., Shen C.-C., Richards D. A. and Cheng H. (2004) Uranium-Series Dating of Speleothems: Current Techniques, Limits, & Applications. In *Studies of Cave Sediments* pp. 177–197.

Hochella M. F. (1995) Mineral surfaces: their characterization and their chemical, physical and reactive nature. In *Mineral Surfaces* (eds. D. J. Vaughan and R. A. D. Pattrick). Chapman & Hall, London. pp. 17–60.

Hochella M. F., Harris D. W. and Turner A. M. (1986) Scanning Auger microscopy as a high-resolution microprobe for geologic materials. *Am. Mineral.* **71**, 1247–1257.

Jupille J. (2014) Analysis of Mineral Surfaces by Atomic Force Microscopy. *Rev. Mineral. Geochemistry* **78**, 331–369.

Lannoo M. (1990) The role of dangling bonds in the properties of surfaces and interfaces of semiconductors. *Rev. Phys. Appl.* **25**, 887–894.

Maupin M. A., Kenny J. F., Huston S. S., Lovelace J. K., Barber N. L. and Linsey K. S. (2010) USGS Circular 1405: Estimated Use of Water in the United States in 2010. *United States Geol. Surv.*

Paquette J. and Reeder R. J. (1995) Relationship between surface structure, growth mechanism, and trace element incorporation in calcite. *Geochim. Cosmochim. Acta* **59**, 735–749.

Rosso K. M. and Becker U. (2003) Proximity effects on semiconducting mineral surfaces II:: Distance dependence of indirect interactions. *Geochim. Cosmochim. Acta* **67**, 941–953.

Sposito G. (1989) *The chemistry of soils*. First Edit., Oxford University Press.

Ta A. J. and Yan B. (2014) 11.13 – High Molecular Weight Petrogenic and Pyrogenic Hydrocarbons in Aquatic Environments. *Treatise on Geochemistry*, 481–509.

Tessis A. C., Penteado-Fava A., Pontes-Buarque M., De Amorim H. S., Bonapace J. A. P., de Souza-Barros F. and Vieyra A. (1999) Pyrite suspended in artificial sea water catalyzes hydrolysis of adsorbed ATP: enhancing effect of acetate. *Orig. Life Evol. Biosph.* **29**, 361–374.

Tossell J. A. (1995) Mineral surfaces: theoretical approaches. In *Mineral Surfaces* (eds. D. J. Vaughan and R. A. D. Pattrick). Chapman & Hall, London. pp. 61–86.

Tossell J. A. and Vaughan D. J. (1992) *Theoretical Geochemistry: Application of Quantum Mechanics in the Earth and Mineral Sciences*., Oxford University Press, New York.

US EPA (1998) *Report to Congress: Solid Waste Disposal in the United States, Vol. II, EPA/530-SW-88-011B*., Washington, D.C.

Vorlicek T. P. and Helz G. R. (2002) Catalysis by mineral surfaces: implications for Mo geochemistry in anoxic environments. *Geochim. Cosmochim. Acta* **66**, 3679–3692.

Walker S. M. and Becker U. (2015) Uranyl (VI) and neptunyl (V) incorporation in carbonate and sulfate minerals: Insight from first-principles. *Geochim. Cosmochim. Acta* **161**, 19–35.

Walker S. M., Marcano M. C., Bender W. M. and Becker U. (2016) Imaging the reduction of chromium(VI) on magnetite surfaces using in situ electrochemical AFM. *Chem. Geol.* **429**, 60–74.

Watts R. J. and Teel A. L. (2014) 11.1 – Groundwater and Air Contamination: Risk, Toxicity, Exposure Assessment, Policy, and Regulation. In *Treatise on Geochemistry* pp. 1–12.

Wogelius R. A. and Vaughan D. J. (2000) Analytical, experimental and computational methods in environmental mineralogy. In *Environmental Mineralogy* (eds. D. J. Vaughan and R. A. Wogelius). Eötvös University Press, Budapest. pp. 7–87.

De Yoreo J. J., Zepeda-Ruiz L. A., Friddle R. W., Qiu S. R., Wasylenki L. E., Chernov A. A., Gilmer G. H. and Dove P. M. (2009) Rethinking classical crystal growth models through molecular scale insights: Consequences of kink-limited kinetics.

Cryst. Growth Des. **9**, 5135–5144.

CHAPTER 2
Uranyl (VI) and Neptunyl (V) incorporation in carbonate and sulfate minerals: insight from first-principles

Abstract

The incorporation of radionuclides into low-temperature mineral hosts may strongly influence the concentration and migration of radioactive contaminants in the subsurface. One difficulty in evaluating the thermodynamics of incorporation is that experiments are often performed at high supersaturations and typically do not reach equilibrium. An alternative way to obtain the equilibrium thermodynamics is the quantum–mechanical analysis of the mineral host and the incorporated species before and after incorporation. In this contribution, density functional theory is used to calculate the energetics, resulting structures, and electronic configuration of uranyl (UO_2^{2+}) and neptunyl (NpO_2^{+}) incorporation into sulfate and carbonate minerals. In each host mineral, gypsum ($CaSO_4 \cdot 2H_2O$), anhydrite ($CaSO_4$), anglesite ($PbSO_4$), celestine ($SrSO_4$), barite ($BaSO_4$), calcite ($CaCO_3$), aragonite ($CaCO_3$), cerussite ($PbCO_3$), strontianite ($SrCO_3$), and witherite ($BaCO_3$), a divalent cation is replaced with either UO_2^{2+} or NpO_2^{+} (in the case of neptunyl, charge balance is maintained with an additional hydrogen ion). The source of the actinyl ion and the sink for the host cation are modeled as both solid and aqueous phases, the latter of which requires an expansion of previous descriptions of incorporation. By combining periodic and cluster computational methods, this newly-developed approach enables the quantum–mechanical simulation of reactions between charged, aqueous molecular species and solid mineral phases.

Among the host minerals considered, gypsum and aragonite are the most favorable hosts for both uranyl and neptunyl uptake ($\Delta E^{U}_{gyp,aq} = 0.19$ eV and $\Delta E^{U}_{arag,aq} = 0.27$ eV for incorporation from aqueous species compared with $\Delta E^{U}_{gyp,solid} = 1.88$ eV and $\Delta E^{U}_{arag,solid} = 1.94$ eV if solid sources and sinks are used; for neptunyl incorporation, $\Delta E^{Np}_{gyp,aq} = 0.36$ eV, $\Delta E^{Np}_{arag,aq} = 3.29$ eV; $\Delta E^{Np}_{gyp,solid} = 0.10$ eV, and $\Delta E^{Np}_{arag,solid} = 3.02$ eV). Incorporation into a vacancy site, for example by filling a cation–anion vacancy with a uranyl-(CO_3^2, SO_4^{2-}) or neptunyl-(Cl^-, HCO_3^-, HSO_4^-) pair, is energetically more favorable than cation substitution, mainly due to the thermodynamic instability of the defect site.

Uranyl and neptunyl incorporation decreases the band gap on the order of 3–5 eV by creating mid-bandgap states. The band gap for aragonite without actinyl incorporation is 4.35 eV; with UO_2^{2+} incorporation the band gap decreases to 1.12 eV and with NpO_2 incorporation to 1.08 eV. For anhydrite, the band gap decreases from 6.39 eV (no incorporation) to 2.24 eV for UO_2^{2+} incorporation and to 1.04 eV for NpO_2^+ incorporation. Vibrational entropy changes during incorporation from solid sources were calculated for selected examples; however, the entropy contribution does not significantly lower the reaction Gibbs free energy relative to the enthalpy of incorporation. $T\Delta S$ ranges from 0.01 eV for calcite to 0.04 eV for anglesite at room temperature. This correction is relatively small compared with other sources of error, in particular variations between different approaches to calculate hydration energies. While the presented approach may still include sources of uncertainty, especially with regard to changes in entropy and hydration, this methodology has promise as a valuable complement to determine the energetics of incorporation reactions.

1. Introduction

The geochemical composition of surface and near-surface environments, including the distribution and concentration of heavy-metal and radionuclide contaminants, is controlled by reactions that take place at the mineral–water interface. At this boundary, chemical species are partitioned between the aqueous phase and the solid phase via a continuum of sorption processes, which range from outer-/inner-sphere adsorption and surface precipitation to structural incorporation into the bulk mineral. In the case of incorporation, trace amounts of a foreign ion in solution are included into the crystal structure of a precipitating mineral in a process known as coprecipitation or through diffusion into the mineral substrate. While ions adsorbed to mineral surfaces may be remobilized through changes in pH or redox conditions, ions structurally incorporated into a host mineral remain insoluble until mineral dissolution. This type of solid solution-aqueous solution (ss-aq) formation has significant implications for the long-term sequestration of mobile contaminants.

The coprecipitation of radionuclides with host minerals (e.g., iron oxyhydroxides, clay minerals, carbonates, and sulfates, to name a few) is a process intrinsic to any setting contaminated with radioactive material and nuclear waste repository systems (Bruno et al., 2007). During the geochemical evolution of a repository, water in the subsurface dissolves trace amounts of radionuclides, such as uranium and neptunium (Atkinson, 1985). These metals readily oxidize to U(VI) and Np(V) and form linear dioxo cations, uranyl (UO_2^{2+}) and neptunyl (NpO_2^{+}), under oxidizing conditions (Silva and Nitsche, 1995; Burns et al., 1997; Antonio et al., 2001). Actinyl ions are then incorporated into solid mineral phases as host minerals dissolve and re-precipitate through contact with groundwater.

A number of experimental studies have explored penta- and hexavalent radionuclide incorporation into various minerals. In particular, uranyl coprecipitation with the calcium carbonates, calcite and aragonite, has received much attention. X-ray absorption and spatially-resolved luminescence spectra indicate that UO_2^{2+} coprecipitates more easily with aragonite than with calcite (Reeder et al., 2000; Reeder et al., 2001; Reeder et al., 2004; Balboni et al., 2015). Reeder et al (2000) suggest that the dominant form of uranium in a carbonate solution is the uranyl triscarbonato complex $[UO_2(CO_3)_3^{4-}]$, in which uranium is in bidentate coordination with three equatorial CO_3^{2-} groups (Allen et al., 1995). For uranyl incorporation into aragonite, the uranyl triscarbonato species remains intact during coprecipitation. In calcite, the uranyl triscarbonato structure is distorted, and the uranyl ion experiences a less stable coordination environment. Neptunyl behaves in the opposite way; NpO_2^+ is incorporated into calcite to a greater extent (Heberling et al., 2008).

Radionuclide incorporation has also been approached from a computational point of view, and several investigations have used ab initio techniques in order to understand the fate of radionuclides in a near-repository environment. Rák et al. have analyzed U, Np, and Pu incorporation into garnet, both naturally occurring and as a potential waste form ($X^{2+}{}_3Y^{3+}{}_2SiO_{12}$ where X is generally Ca, Fe^{2+}, Mn, or Mg and Y is Al, Cr, or Fe^{3+}) (Rák et al., 2011; Zs. Rák et al., 2013; Zs Rák et al., 2013). These incorporation studies employ first-principles methods to calculate crystal structures, electronic structures, as well as bonding properties to determine the mechanism of incorporation, specifically which cation site would most likely host the radionuclide contaminant. Iron oxides and iron hydroxides have also been popular hosts for quantum–mechanical incorporation

research (Nico et al., 2009; Skomurski et al., 2010; Kerisit et al., 2011). All of these studies deal only with solid-state incorporation.

Well-established thermodynamic formalisms of ss-aq systems typically rely upon experimentally-determined distribution coefficients and solubility relationships to resolve the partitioning behavior of a species in the aqueous phase and the solid periodic phase. While this strategy leads to equilibrium expressions for ss-aq partitioning, it is difficult to verify if experiments have reached thermodynamic equilibrium and if measurements of thermodynamic quantities reflect steady-state conditions. Alternatively, macroscopic, equilibrium thermodynamic parameters can be derived from atomistic simulations. Using ab initio methods, the thermodynamic properties of a system can be calculated independently of empirical parameters. Dealing with incorporation at the quantum–mechanical level, however, is challenging due to the combination of solid and aqueous systems; the incorporated species typically originates in solution, yet is incorporated into a solid mineral structure. In this light, the charged, aqueous source species is best represented by a quantum–mechanical cluster model, while the solid host phase is better treated using periodic boundary conditions. This same type of modeling difficulty applies to the ion in the host mineral that is replaced and released into solution. The challenge lies in how to apply uniform computational theory throughout the solid-aqueous incorporation reaction.

In this contribution, we have refined a quantum–mechanical approach to calculate the energetics and thermodynamics of uranyl and neptunyl incorporation into a suite of sulfate (barite, anglesite, celestine, anhydrite, and gypsum) and carbonate minerals (witherite, cerussite, strontianite, aragonite, and calcite). Because coprecipitation

reactions involve both 3D-periodic solids (i.e., the host mineral) and non-periodic molecular electrolyte species (i.e., the solute that is incorporated into the bulk) the design of the system model requires special attention. From a computational standpoint, each type of reactant and product must be treated independently with regard to their respective periodicity. Yet, in order to quantum mechanically calculate reaction energies (and other thermodynamic properties), the exact same system configuration and computational settings must be used for all species in the same chemical reaction. Our approach expands upon the methods developed by Shuller et al. (2013) in which charge-neutral periodic species and charged molecular species are calculated separately and then recombined into a single chemical equation. This procedure combines periodic and cluster models (as well as a model for hyd1ration) to simulate the incorporation of an aqueous ion into a solid mineral phase without the use of experimental data as fitting parameters. Once potential sources of error, such as the choice of computational settings or the treatment of hydration, are identified (discussed in Section 4), this method can be used for a number of mineralogical, petrological, and environmental applications concerning chemical reactions between minerals and dissolved species in solution at equilibrium. This computational approach is an independent insight into the thermodynamics of incorporation. Furthermore, the simulation of incorporation reactions can be used to screen mineral candidates that exhibit significant incorporation of aqueous contaminants.

2. Computational methods

The computational approach begins with solid sources and sinks for the actinides and the cations replaced in the mineral host. This allows for the comparison of the relative stability of the actinyl-incorporated mineral with the stability of the corresponding host and the oxide source and sink phases (described in Eqs. (2.1) and

(2.2) for uranyl and neptunyl incorporation, respectively). In both equations, the letter *X* represents the cation of each host mineral: Sr^{2+}, Ba^{2+}, Pb^{2+}, and Ca^{2+}. The reactants include a solid source of the actinide and a host mineral, and the products are the actinide-containing mineral and a sink for the cation displaced from the host. The energetics of all phases in such a reaction can be calculated using consistent computational parameters.

$$X_4(SO_4,CO_3) + UO_3 \Leftrightarrow X_3(UO_2)(SO_4,CO_3)_4 + XO \quad (2.1)$$

$$X_4(SO_4,CO_3) + ½\ Np_2O_5 + ½\ H_2O \Leftrightarrow X_3(NpO_2)(HSO_4,HCO_3)(SO_4,CO_3)_3 + XO \quad (2.2)$$

In most geochemical systems, co-precipitation takes place at the mineral–water interface, and the source and sink phases for the actinide and host cation are aqueous ions in solution. Therefore, the solid source and sink phases are subsequently replaced by aqueous source and sink phases. A necessary prerequisite for using a quantum–mechanical or any type of atomistic assessment of a geochemical process is that consistent methods and settings are used for all calculations, *i.e.*, all species in a chemical reaction must be treated and evaluated with identical computational parameters. For example, in a DFT calculation, consistent density functional, planewave energy cutoff or basis set, *k*-point density, pseudopotentials, atomic relaxation constraints, periodicity, solvation approach for aqueous species, and electron smearing, *etc.* must be the same across all phases involved in the reaction. Such internally-consistent equations can then be combined to obtain aqueous hydrated molecules and periodic solids in the same reaction equation.

2.1. Periodic calculations

Total-energy calculations and geometry optimizations of periodic phases were performed using the software packages CASTEP (Cambridge Serial Total Energy Package) (Segall et al., 2002) and DMol^3 (Local Density Functional Calculations on Molecules) (Delley, 1990). CASTEP is a density functional theory-based code that approximates the wave functions of valence electrons using a series of sinusoidal planewave functions of various wavelengths under periodic boundary conditions. The exchange–correlation potential was approximated with the generalized gradient approximation (GGA) scheme, parameterized by the Perdew–Burke–Ernzerhof (PBE) functional (Perdew et al., 1996). In this work, GGA was used for all geometry optimizations and qualitative comparison of the electronic structure before and after incorporation.

Increasing the kinetic energy cutoff from 500 eV to 800 eV decreased the final energy of the uranyl-incorporated anglesite unit cell by less than 0.01 eV. Therefore, to minimize computational expense, an energy cutoff for planewave expansion of 500 eV was used for all periodic calculations. Ultrasoft pseudopotentials were used to describe core electron behavior, while remaining valence electrons were treated explicitly. For example, 78 electrons are included in the uranium pseudopotentials, and the remaining 14 electrons comprise the valence band: [Xe] $5f^3\ 6s^2\ 6p^6\ 6d^1\ 7s^2$) (Vanderbilt, 1990). Pseudopotential generation algorithms are explained in detail by Vanderbilt (1990). For geometry-optimization calculations, the BFGS method was used (Pfrommer et al., 1997). A Monkhorst–Pack grid was used to generate the set of k-points used to sample the Brillouin zone. Grid parameters were derived such that the k-point separation was 0.05 $Å^{-1}$. Self-consistent field cycles were assumed to converge with an energy

difference of less than 10^{-4} eV. A spin-polarized approach was implemented for phases containing Np^{5+} in order for the two unpaired electron spins in the 5f orbitals to adopt the lowest-energy configurations. A Hubbard U correction was used to improve Coulomb repulsion among the Np 5f electrons (U = 4.25 eV and J = 0.6 eV). Spin–orbit interactions were neglected. Although spin–orbit coupling is important for heavy elements, such as U and Np (even though U contains no unpaired spins or f electrons), incorporation energies are based on total energy differences, and, in a separate study, we found that, if the bonding environment and oxidation state do not change, the errors introduced by neglecting spin–orbit coupling largely cancel out.

2.2. Cluster calculations

For the treatment of molecular and aqueous species, DMol[3] was used to calculate the relaxed geometries and energy minima of neutral and charged cluster configurations. Although CASTEP can be used to calculate non-periodic systems, rather than impose superficial periodicity on molecular species, using a cluster-based quantum mechanical code is a more efficient way to model charged, aqueous clusters. Using a cluster-based model eliminates additional energy contributions due to the interaction of the charge with a neutralizing background charge. As with the periodic calculations, the GGA-PBE potential was used with effective core potentials to account for core electrons (Dolg et al., 1987). Double Numerical plus d-functions (DND) were used as the numerical basis set to describe atomic orbitals.

Hydration energies were approximated by attaching explicit water molecules to each ion of interest according to Eq. (2.3). Water molecules were added until the first

hydration sphere was complete (typically $n = 6$; additional water molecules were "squeezed out" of this first hydration sphere surrounding the ion).

$$ion + n(H_2O) \Leftrightarrow ion \bullet (H_2O)_n \quad (2.3)$$

Alternatively, each ion was embedded in a dielectric fluid using COSMO (Conductor-like Screening MOdel) as implemented in DMol^3 (Klamt and Schuurmann, 1993; Renock et al., 2013). COSMO is a continuum solvation model in which the solute molecule or ion forms a cavity within a dielectric continuum, which represents the solvent. A dielectric constant of 78.54 at 25 °C was used to represent water. COSMO evaluates the electrostatic contribution to the free energy of solvation and uses the linear function of the cavity surface to correct for non-electrostatic energy contributions, such as the formation of the cavity and the effects of dispersion (Andzelm et al., 1995). An excellent review of continuum solvation models for quantum mechanical calculations can be found in Tomasi et al., 2005. Best comparison with experiment (where available) was obtained by combining discrete adsorbed water molecules with a dielectric fluid surrounding this first hydration sphere. For this reason, calculated hydration energies reported here are the results of this combined approach unless stated otherwise.

2.3. Vibrational entropy of solids

It should be noted that reaction energies calculated in CASTEP or in DMol^3 are not equal to the Gibbs free energy of the reaction. Total-energy calculations described here compute the total nuclear and electronic energy of atoms or ions in a vacuum at 0 K, though without the contribution from zero-point energies (Hirano, 1993). Zero-point energies are only included in the examples where we explore frequency space for calculating entropy contributions. In order to account for atomic and molecular vibrations

at temperatures above 0 K, harmonic frequencies are calculated from a Cartesian second-derivative matrix weighted for the masses of each atom (Wilson et al., 1980). With these frequencies, vibrational, rotational (linear and non-linear), and translational contributions to the entropy can be evaluated as a function of temperature. For example, the vibrational entropy is calculated according to Eq. (2.4), where R is the gas constant (8.314 J mol^{-1} K^{-1}), h is the Planck constant (6.626×10^{-34} J s), v_i is the ith normal vibration frequency, k is the Boltzmann constant (1.381×10^{-23} J mol^{-1}), and T is temperature.

$$S_{vib} = R \sum_i \left\{ \frac{\left(\frac{hv_i}{kT}\right)\exp\left(-\frac{hv_i}{kT}\right)}{\left[1-\exp\left(-\frac{hv_i}{kT}\right)\right]} - ln\left[1-\exp\left(-\frac{hv_i}{kT}\right)\right] \right\} \quad (2.4)$$

Additional formalisms are found in detail in Hirano (1993). The Gibb's free energy of the overall reaction can then be solved by computing the vibrational entropy for each phase involved in the incorporation process.

While this study deals explicitly with vibrational entropies of solids, other sources of entropy include changes in entropy associated with hydration as well as the entropy associated with different amounts of products and reactants. The hydration of an ion typically produces short-range ordering in the network of water molecules surrounding the ion, which reduces the overall entropy of the solvent. An imbalance between the number of reactant species and the number of product species may also cause a net change in entropy. These contributions are discussed further in Section 3.4.

3. Results and discussion

3.1. Energetics of incorporation

3.1.1. Solid oxide source and sink phases

First-principles total-energy calculations were performed for each species in the incorporation reaction defined in Eqs (2.1) and (2.2). The overall reaction energy, also defined as the incorporation energy, is the energy required to substitute one UO_2^{2+} or NpO_2^{+} ion for one cation inside the unit cell and is calculated as the difference in the sum of product energies and the sum of reactant energies. The phases UO_3 and Np_2O_5 were chosen as solid actinide oxide sources in which each actinide ion has the same oxidation state as the incorporated actinide species. The phase XO is the respective solid oxide sink phase. In the case of neptunyl incorporation, NpO_2^{+} replaces a divalent cation in the host mineral, and charge balance is maintained with the inclusion of an additional hydrogen ion into the structure as either HSO_4^{-} or HCO_3^{-}. During the subsequent geometry optimization, the H atom is free to find its most energetically favorable position, *e.g.*, near the anion (carbonate or sulfate or in the vicinity of the actinyl oxygen. As described by the symmetry elements of each space group, each cation in the host mineral is positioned in a symmetrically, and therefore electronically, identical environment. Consequently, all four locations available for cation-uranyl or cation-neptunyl substitution are computationally equivalent (however, the actual incorporation decreases symmetry, typically to P1). Geometry optimizations were used to refine the structure of each phase before and after incorporation. The incorporation energies for uranyl and neptunyl incorporation into select sulfate and carbonate minerals with solid oxide source and sink phases are listed in Table 2. 1.

Table 2. 1 indicates that among the sulfates, the lowest uranyl incorporation energies were calculated for anglesite, followed by gypsum and anhydrite. The fact that barite has the highest incorporation energy is somewhat surprising because, among the isostructural minerals (barite, celestine, and anglesite), barite has the largest cation radius and the lattice parameters. One would have expected that barite provides the most space for the bulkier actinyl ions. Gypsum is a relatively favorable host likely due to the water layers in this mineral that can relax and provide space for the actinyl ions (explained in more detail in Section 0). As for the carbonates, the Ba-containing structure is the least favorable host. One could then hypothesize that the Ba structures have the least freedom to relax about the incorporated defect.

Table 2. 1. Incorporation energies for UO_2^{2+} and NpO_2^{+} incorporation into selected sulfate and carbonate host minerals. The reaction energy is calculated from Eqs. (2.1) for uranyl and (2.2) for the coupled substitution of neptunyl.

Host Phase	$UO_2^{2+}{}_{(solid)}$ ΔE_{rxn} (eV)	$NpO_2^{+}{}_{(solid)}$ ΔE_{rxn} (eV)		$UO_2^{2+}{}_{(solid)}$ ΔE_{rxn} (eV)	$NpO_2^{+}{}_{(solid)}$ ΔE_{rxn} (eV)
barite ($BaSO_4$)	4.05	4.25	witherite ($BaCO_3$)	3.37	4.24
anglesite ($PbSO_4$)	1.52	2.24	cerussite ($PbCO_3$)	1.33	2.24
celestine ($SrSO_4$)	3.71	4.28	strontianite ($SrCO_3$)	2.48	3.73
anhydrite ($CaSO_4$)	2.37	4.77	aragonite ($CaCO_3$)	1.94	3.02
gypsum ($CaSO_4 \cdot 2H_2O$)	1.88	3.29	calcite ($CaCO_3$)	2.86	3.63

3.1.2. Aqueous source and sink phases

Although the chemical reactions in Eqs. (1) and (2) provide the adequate stoichiometric ratios needed to calculate incorporation energy, solid source and sink phases do not describe aqueous fluid-mineral equilibria. Co-precipitation occurs when minerals precipitate from solution and incorporate foreign solutes into their crystal structures. The conversion of solid sources and sinks to aqueous complexes models more appropriately uranyl and neptunyl incorporation in a geochemical aqueous-solid equilibrium system. However, this integration of neutral solids with charged molecular species calls for careful consideration. For any atomistic approach, the energy of a

reaction can only be evaluated if each species in the reaction is assessed identically with regard to computational parameters and system configuration (*e.g.*, either all species are periodic or all species are clusters). The transition from solid source and sink phases to aqueous sources and sinks therefore requires a series of chemical equations in which every species in a single equation shares the same periodicity (Shuller et al., 2013). These equations and their reaction energies are then combined to cancel unwanted terms and to compute an overall reaction energ for the incorporation of aqueous ions into periodic structures.

Figures 2.1 and 2.2 illustrate how this series of equations is combined to calculate the overall incorporation energy using $UO_2^{2+}{}_{(aq)}$ and $NpO_2^{+}{}_{(aq)}$ incorporation into anglesite as an example. The reaction energies for uranyl and neptunyl incorporation with solid oxide source and sink phases (shown in Table 2. 1) are calculated using a periodic quantum–mechanical approach (*e.g.*, CASTEP or $DMol^3{}_{periodic\ solid}$). The first step in the transition to aqueous phases is to substitute these solid-state sources and sinks with clusters or neutral molecules constrained by periodic boundary conditions. These so-called periodic molecules are gas-phase molecules placed in the center of a $10 \times 10 \times 10$ $Å^3$ unit cell and serve as placeholders in the substitution procedure. This large unit cell functions to minimize the interaction between molecules in adjacent unit cells, particularly when a dipole moment is present. Next, the periodic boundary conditions are removed, and the source and sink periodic molecules are converted to neutral (non-periodic) molecular species. At this step, reaction energies can be calculated using a cluster-type quantum–mechanical approach and consistent computational parameters (for example basis set, core electron treatment, labeled as *cluster*

configuration in Figures 2.1 and 2.2). Any reaction energy at this step is mainly due to molecular dipole–dipole interactions between periodic molecules and is ideally much less than the overall reaction energy. Since the transition from periodic to isolated molecules should not "produce" any additional energy and, in fact, their contribution to the overall energy is cancelled out in the end, the purpose of this transition is mainly to ensure that no significant computational artifacts are introduced (*e.g.*, change of basis set, DFT functional, level of theory for highly correlated systems, pseudopotential,…) during the transition from 3D to 0D periodic boundary conditions. This transition from solid source and sink phases to aqueous sources and sinks is shown in more detail in Table 2.A1 in

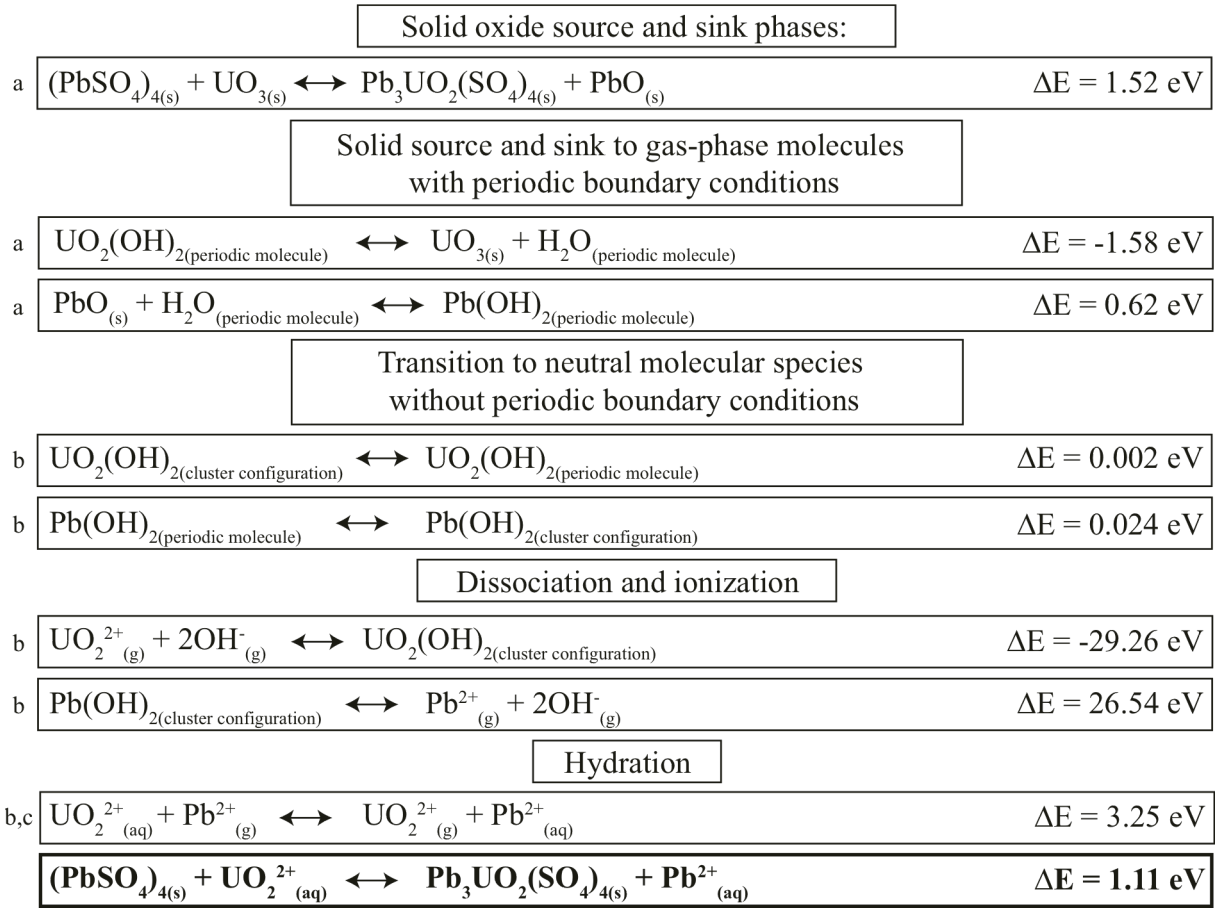

Figure 2. 1. This series of equations demonstrates the transition from solid oxide source and sink phases to charge aqueous complexes for $UO_2^{2+}{}_{(aq)}$ incorporation into anglesite ($PbSO_4$). For each equation, the energy of each term is calculated under identical computational conditions. Adding subsequent equation yields the final incorporation reaction with a reaction energy of 1.11 eV. [a]calculated in CASTEP, [b]calculated in DMol^3, [c]hydration energy for Pb^{2+} from (Marcus, 1994).

Appendix 2.A.

Dissociation and ionization equations are added next to the series as well as expressions for ion hydration energies. Hydration energies for the uranyl and neptunyl ions were calculated by embedding each ion in a dielectric continuum and adding explicit water molecules until the hydration energies converged at −18.02 eV for UO_2^{2+} and −7.50 eV for NpO_2^{+}. These values agree comparatively well with published calculated solvation energies: ΔE_{hyd} for UO_2^{2+} = −17.78 ± 0.2 eV (Gutowski and Dixon, 2006) (with the corresponding experimental value of −18.00 ± 0.65 eV) and ΔE_{hyd} for

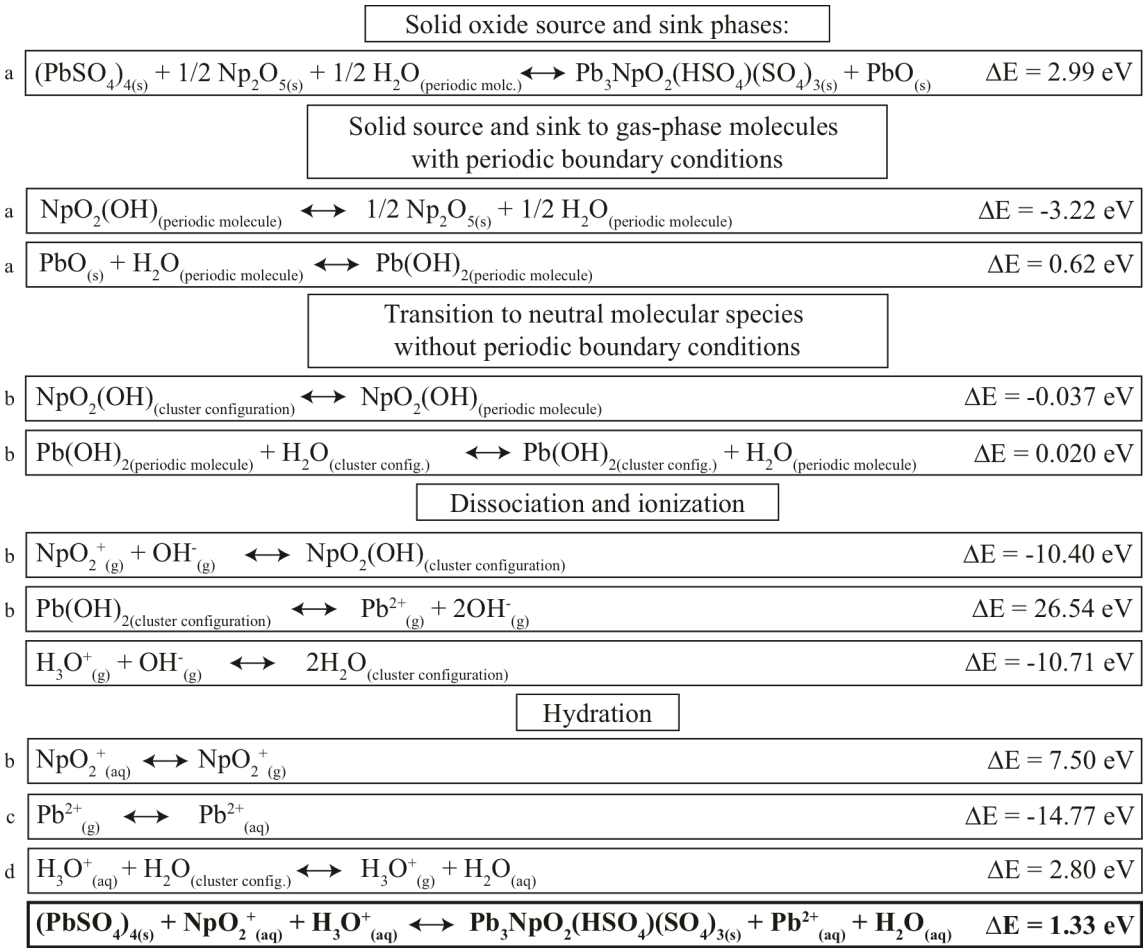

Figure 2. 2. Transition from solid oxide to charged aqueous cluster source and sink phases for $NpO_2^{+}{}_{(aq)}$ incorporation into anglesite. [a]calculated in CASTEP, [b]calculated in DMol[3], [c]from (Marcus, 1994), [d]from (Kiliari et al, 2012) and (Shuller et al. 2013) and enthalpy of the condensation of water.

$NpO_2^+ = -7.83 \pm 2.0$ eV (Tsushima and Suzuki, 2000) (no experimental data are available for neptunyl hydration).

It is important to note that COSMO only evaluates the electrostatic contribution of the free energy of hydration (ΔG_{hyd}). Non-electrostatic contributions to ΔG_{hyd} include the formation of the cavity surrounding the solute molecule as well as dispersion effects. These terms are expressed as a linear function of the surface of the cavity, which are used to "correct" for the missing non-electrostatic energy contribution (Renock et al., 2013). Despite this correction, COSMO consistently underestimates the hydration energy of smaller ionic species. The comparison between calculated hydration energies and published values is shown in Table 2. 2. Due to this discrepancy, hydration energies from Marcus (1994) were used in the conversion from solid to aqueous source and sink phases. Because there is little to no thermodynamic data for actinide hydration, we approximate uranyl and neptunyl hydration energies with a combination of explicit water molecules and COSMO. COSMO evaluates hydration energy in terms of the free energy of salvation; therefore, we use ΔG_{hyd}. COSMO is just one example of a polarized continuum model with which to estimate the hydration energy of an ion. Other approaches, *e.g.*, UA0, UAKS, IEF-PCM, may be used to account for the bulk effects of the solvent (Tomasi et al., 2005).

Table 2. 2. Comparison of hydration energies calculated with explicit water molecules embedded in a dielectric continuum model (COSMO) and published hydration energies. [a](Marcus, 1994).

Species	COSMO/DMol^3 (eV)	ΔG_{hyd} (eV)[a]
Ba^{2+}	-11.73	-13.00
Pb^{2+}	-11.78	-14.77
Sr^{2+}	-12.48	-14.30
Ca^{2+}	-13.74	-15.60
OH^-	-4.19	-4.46

$UO_2^{2+}{}_{(aq)}$ and $NpO_2^{+}{}_{(aq)}$ incorporation energies are listed in Table 2. 3. In each isostructural host mineral, the actinyl ion is positioned in the exact same initial orientation. Results indicate that gypsum is the most favorable sulfate host mineral for both uranyl and neptunyl incorporation (ΔE_{rxn} = 0.19 eV and 0.36, respectively). Among the remaining anhydrous sulfates, celestine and anhydrite are more favorable for UO_2^{2+} incorporation, although both celestine and particularly anhydrite have significantly higher NpO_2^{+} incorporation energies. Barite is the least favorable host for UO_2^{2+} incorporation. Of the four cations, barium has the largest ionic radius (1.60 Å [XII]). One might expect that the cation site in barite would be able to accommodate the uranyl ion with a lesser degree of lattice distortion and thus require less energy for incorporation; however, the barite unit cell experiences a 20.59% change in volume (initial volume: 346.8 Å^3, $\alpha_{initial}$ = $\beta_{initial}$ = $\gamma_{initial}$ = 90°, final volume: 418.2 Å^3, α_{final} = 89.14°, β_{final} = 89.97°, γ_{final} = 75.23°). This change in volume is similar to the volume changes observed with UO_2^{2+} incorporation into the other sulfate minerals (anglesite: 18.81%, celestine: 20.77%, anhydrite: 23.75%). Values of ΔE_{rxn} suggest that the ionic radius of the host cation is not the principal factor in minimizing incorporation energy. A more detailed description of optimized incorporation structures is provided in Section 0.

Table 2. 3. Energies for UO_2^{2+} and NpO_2^{+} incorporation with aqueous source and sink phases.

Host Phase	$UO_2^{2+}{}_{(aq)}$ ΔE_{rxn} (eV)	$NpO_2^{+}{}_{(aq)}$ ΔE_{rxn} (eV)		$UO_2^{2+}{}_{(aq)}$ ΔE_{rxn} (eV)	$NpO_2^{+}{}_{(aq)}$ ΔE_{rxn} (eV)
barite ($BaSO_4$)	2.84	1.79	witherite ($BaCO_3$)	2.16	1.78
anglesite ($PbSO_4$)	1.11	0.58	cerussite ($PbCO_3$)	0.91	0.58
celestine ($SrSO_4$)	0.61	0.74	strontianite ($SrCO_3$)	2.09	2.27
anhydrite ($CaSO_4$)	0.68	1.84	aragonite ($CaCO_3$)	0.27	0.10
gypsum ($CaSO_4$•$2H_2O$)	0.19	0.36	calcite ($CaCO_3$)	3.53	1.62

For the carbonate minerals, aragonite provides the lowest incorporation energies for both aqueous uranyl and neptunyl incorporation. Calcite, on the other hand, yields the highest UO_2^{2+} incorporation energy. This difference in incorporation energy may be attributed to the structural differences between aragonite (Pmcn) and calcite ($R\bar{3}c$). Ca coordination in aragonite (9-fold coordination) is higher than that in calcite (6-fold coordination). That the aragonite structure tends to incorporate large cations is manifested by the fact that carbonates of large divalent cations (ionic radii >1 Å, *e.g.*, Ba, Sr, Pb) tend to crystallize with aragonite structure and carbonates of smaller cations (<1 Å, *e.g.*, Mn, Fe, Mg) with calcite structure, while Ca^{2+}, with a radius of about 1 Å, crystallizes with both structures. The relative reaction energy of UO_2^{2+} incorporation into calcite is greater than that of NpO_2^{+} incorporation into calcite, which suggests that calcite incorporates neptunyl preferentially over uranyl. In order to maintain the host mineral's neutral charge, neptunyl incorporation is coupled with the addition of a hydrogen ion. Geometry optimizations reveal that the hydrogen points towards one of the neptunyl O atoms.

3.1.3. Incorporation and defects

The incorporation energies in Table 2. 3 are the result of the replacement of a host cation with a uranyl or neptunyl + hydrogen ion in the conventional 1 × 1 × 1 unit cell. However, another possible coprecipitation mechanism is the incorporation of the foreign ion into a preexisting defect in the crystal structure. Crystalline solids in thermodynamic equilibrium all contain defects due to local disorder, non-stoichiometry, and the presence of aliovalent impurity ions (Kröger, 1985). One example of such a point defect is a vacancy. To model uranyl incorporation into a vacant lattice site, a vacancy is created by removing a cation and an anion from the unit cell. The uranyl ion can then substitute for a

cation adjacent to the missing cation/anion pair (as per Eq. (2.5a), leaving a cation/anion vacancy in the structure) or the uranyl ion along with either an additional sulfate or carbonate ion can fill the vacancy, which is described by Eq. (2.5b) ($X = Sr^{2+}$, Ba^{2+}, Pb^{2+}, or Ca^{2+}). Incorporation energies for minerals with and without vacancies in the final structure are listed in Table 2. 4.

Table 2. 4. Uranyl incorporation energies for vacancy incorporation.

UO_2^{2+} *with* vacancy in final structure (5a)		$UO_2^{2+} + SO_4^{2-}/CO_3^{2-}$ into vacancy (5b)	
	ΔE_{rxn} (eV)		ΔE_{rxn} (eV)
anglesite ($PbSO_4$)	0.98	anglesite ($PbSO_4$)	-3.31
celestine ($SrSO_4$)	-1.39	celestine ($SrSO_4$)	-3.18
cerussite ($PbCO_3$)	-0.75	cerussite ($PbCO_3$)	-1.72
strontianite ($SrCO_3$)	0.77	strontianite ($SrCO_3$)	-2.83

$$X_{3,cation}(SO_4,CO_3)_{3,anion} + UO_2^{2+}{}_{(aq)} \Leftrightarrow X_2(UO_2)_{cation}(SO_4,CO_3)_{3,anion} + X^{2+}{}_{(aq)} \quad (2.5a)$$

$$X_{3,cation}(SO_4,CO_3)_{3,anion} + UO_2^{2+}{}_{(aq)} + (SO_4^{2-},CO_3^{2-})_{(aq)} \Leftrightarrow X_3(UO_2)(SO_4,CO_3)_4 \quad (2.5b)$$

In order to minimize computational expense, only a few host minerals were chosen to demonstrate the effect of a vacancy on uranyl incorporation. Overall, UO_2^{2+}incorporation into a unit cell with a vacancy is more favorable than incorporation into a regular unit cell. This result is consistent with Skomurski et al. (2000) in that incorporation of radionuclide polyions is more likely to occur at a defect in the lattice. Although vacancies are inherently present in minerals, the local structural relaxation and disruption of periodic bond chains result in a positive vacancy formation enthalpy (*e.g.*, 4.59 eV for vacancy formation in anglesite and 3.16 eV in cerussite). This disruption results in a less energetically favorable initial host mineral configuration (which is then relatively more favorable for uranyl incorporation) and could explain the decrease in incorporation energies as compared with incorporation without vacancies. When both a

UO_2^{2+} and an SO_4^{2+} or CO_3^{2+} ion fill the cation and anion vacancies, the incorporation energy is even more negative than the energy associated with uranyl incorporation into a structure with a vacancy remaining. By plugging up these vacancies, the resulting structure is more stable than that with vacancies.

In addition to a vacancy point defect, substitution of the incorporated ion (in this case neptunyl) with an impurity ion was investigated. To set up this calculation, an anion and a cation in the host mineral were replaced with ammonium chloride (NH_4Cl). Ammonium and chloride are frequently used as counter ions in solution for co-precipitation experiments. In these experiments, an actinide-containing doping solution is introduced to supersaturated solutions of the host mineral cation and anion (*e.g.*, $CaCl_2$ and NH_4HCO_3 solutions for calcite precipitation). Incorporation is measured as a function of time and initial actinide solution concentration. As a result, an ammonium chloride impurity can be incorporated into the host mineral and subsequently substituted with a neptunyl ion, as in Eq. (2.6) ($X = Sr^{2+}$, Ba^{2+}, Pb^{2+}, or Ca^{2+}). Table 2. 5 shows the incorporation energies for neptunyl substitution with an impurity ion.

$$X_3(NH_4Cl)(SO_4,CO_3)_3 + NpO_2^{+}{}_{(aq)} \Leftrightarrow X_3(NpO_2Cl)(SO_4,CO_3)_3 + NH_4^{+}{}_{(aq)} + H_2O_{(l)} \quad (2.6)$$

For the sulfate host minerals, the neptunyl incorporation energy of anglesite with an NH_4Cl impurity increased from 1.33 eV to 3.69 eV. Incorporation into celestine and anhydrite, however, became slightly more favorable.

Table 2. 5. Energies for neptunyl substitution for ammonium in (NH_4Cl) impurity

NpO_2^+ with NH_4Cl impurity			
	ΔE_{rxn} (eV)		ΔE_{rxn} (eV)
anglesite ($PbSO_4$)	3.69		
celestine ($SrSO_4$)	1.61	strontinaite ($SrCO_3$)	2.20
anhydrite ($CaSO_4$)	3.05	aragonite ($CaCO_3$)	1.40

3.2. Optimized incorporation structures

In a quantum–mechanical geometry optimization, each atom is allowed to relax such that the entire structure adopts the lowest energy configuration, as shown for neptunyl-incorporated gypsum in Figure 2. 3A. Even though the GGA-PBE functional has been shown to overestimate lattice parameters (Wu and Cohen, 2006; Demichelis et al., 2010), calculated lattice vectors of pure anhydrite and gypsum (for example) are in relatively good agreement with measured lattice vectors. For anhydrite, percent differences between calculated and measured lattice vectors are 1.5% (a direction), 1.9% (b), and 1.1% (c) (Hawthorne and Ferguson, 1975). For gypsum, these percent differences are 1.6% (a), 2.1% (b), and 1.6% (c). Gypsum has a layered structure with double sheets of sulfate and calcium ions separated by double sheets of asymmetrically arranged water molecules parallel to the (010) face (Pedersen and Semmingsen, 1982). The neptunyl ion is oriented approximately parallel to the (001) face. One of the neptunyl O atoms extends into the water interlayer, while the other neptunyl oxygen forms a hydroxide bond with a distance of 1.01 Å, closer than a typical hydrogen bond. For comparison, the neptunyl O–H bond in the neptunyl-incorporated anhydrite unit cell has a distance of 2.69 Å (Figure 2. 3B). Although both gypsum and anhydrite contain Ca^{2+} and SO_4^{2+} ions, the water interlayer of gypsum better accommodates uranyl and neptunyl incorporation as demonstrated by the lower incorporation energy.

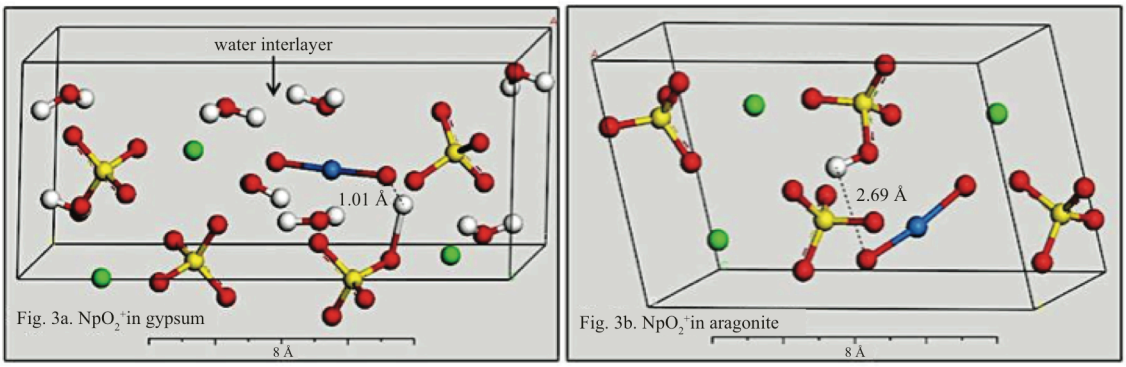

Figure 2. 3. Neptunyl incorporated into gypsum ($CaSO_4 \cdot 2H_2O$) (a) and anhydrite ($CaSO_4$) (b). In each unit cell, one Ca^{2+} cation is replaced by an NpO_2^+ and an H^+ for charge compensation. The reaction energy for neptunyl incorporation into gypsum is lower than that into anhydrite. In the case of incorporation into gypsum (3a), the neptunyl ion extends into the water interlayer. H: white, O: red, S: yellow, Ca: green, Np: blue.

Figure 2. 4A-C show the cation coordination environment for anglesite, uranyl-incorporated anglesite, and neptunyl-incorporated anglesite. For both types of incorporation, the sulfate groups rotate approximately 45° such that the O atoms in the sulfate group point away from the O atoms of the actinyl ions. Both U and Np are equatorially coordinated by four O atoms from four monodentate sulfate groups (U–O distances: 2.32, 2.41, 2.44, 2.49 Å; Np-O distances: 2.39, 2.43, 2.57, 2.70 Å). On average, these bond distances are shorter than the Pb–O bonds in anglesite (2.63, 2.67, 2.79, 3.06, 3.08, 3.34 Å). U incorporated into anhydrite is equatorially coordinated by four O atoms. U incorporated into celestine and barite, however, is coordinated by five O atoms from three unique sulfate groups (Figure 2. 5). In NpO_2^+-incorporated barite, the unit cell becomes more elongated and tilted with the incorporation of neptunyl ($\alpha = 89.96°$, $\beta = 93.98°$, $\gamma = 76.78°$) compared with that of anglesite ($\alpha = 78.52°$, $\beta = 93.49°$, $\gamma = 100.2°$). The NpO_2^+ maintains a more linear orientation (O–Np–O = 176.35°) in barite compared with neptunyl in anglesite (O–Np–O = 168.26°), yet rotates so that the neptunyl ion is at a diagonal from the long *a* axis.

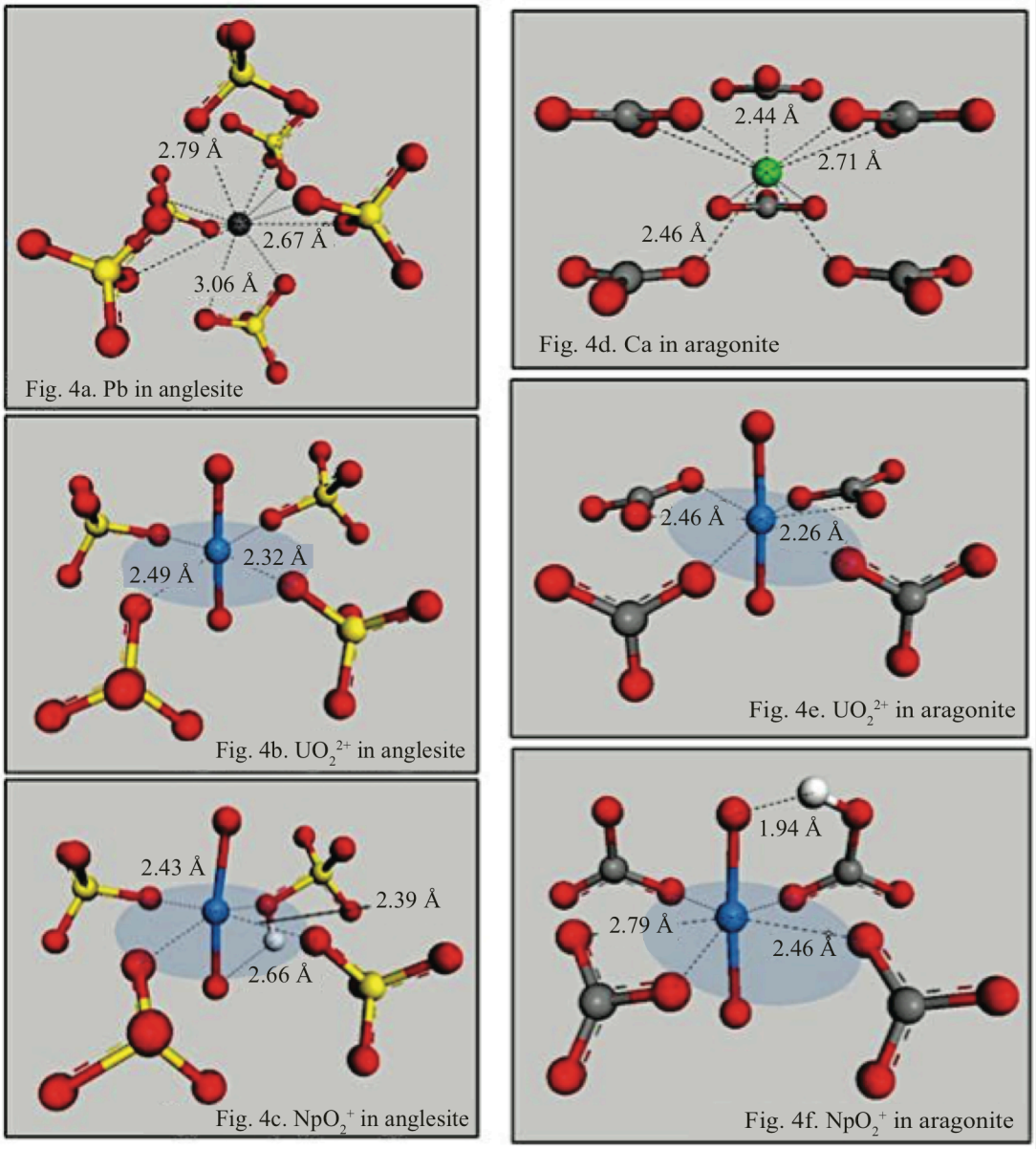

Figure 2. 4. Coordination environments in anglesite (a) Pb, (b) UO_2^{2+} incorporation, and (c) NpO_2^{+} incorporation. and for aragonite (d) Ca, (e) UO_2^{2+} incorporation, and (f) NpO_2^{+} incorporation.

As with the sulfates, the distortion of the host mineral anion can be observed in incorporation into carbonates with the aragonite-structure (Figure 2. 4D-F). Of particular note is the uranyl incorporation into aragonite. The carbonate groups adjacent to the uranyl ion rotate so that six carbonate O atoms form the equatorial coordination environment of uranium with nearest-neighbor distances of 2.26, 2.43, 2.47, 2.52, 2.63,

and 2.65 Å. Instead of a triscarbonato complex, U is in bidentate coordination with two carbonate groups and in monodentate coordination with two more carbonates. Witherite, strontianite, and cerussite also exhibit this tetracarbonate coordination. In calcite, however, the carbonate groups remain roughly parallel and do not reorient with respect to the uranyl ion (Figure 2. 5B). The coordination number of uranium incorporated into calcite is six (U–O distances: 2.39, 2.44, 2.49, 2.58, 2.68, 2.73 Å), and the equatorial O atoms coordinate the uranium in a highly puckered plane. This relative rigidity of the calcite structure may explain the less favorable incorporation energy. A lesser degree of rotation is observed in the neptunyl-incorporated aragonite. The NpO_2^+ ion distorts from a linear configuration (O–Np–O angle ≅ 180°) to a bent structure (O–Np–O = 171°), and the distance between the charge-balancing H^+ and the adjacent neptunyl oxygen is 1.66 Å.

For each uranyl-incorporated structure, the uranyl ions incorporated into each mineral relax to an average length of 1.787 Å and an average O–U–O angle of 177.63°. These results are in good agreement with experimental data, which suggests distinctively short U—O bond lengths (ca. 1.78 Å) (Görller-Walrand and Colen, 1982; Thompson et al., 1997; Kubicki et al., 2009; Fortier and Hayton, 2010).

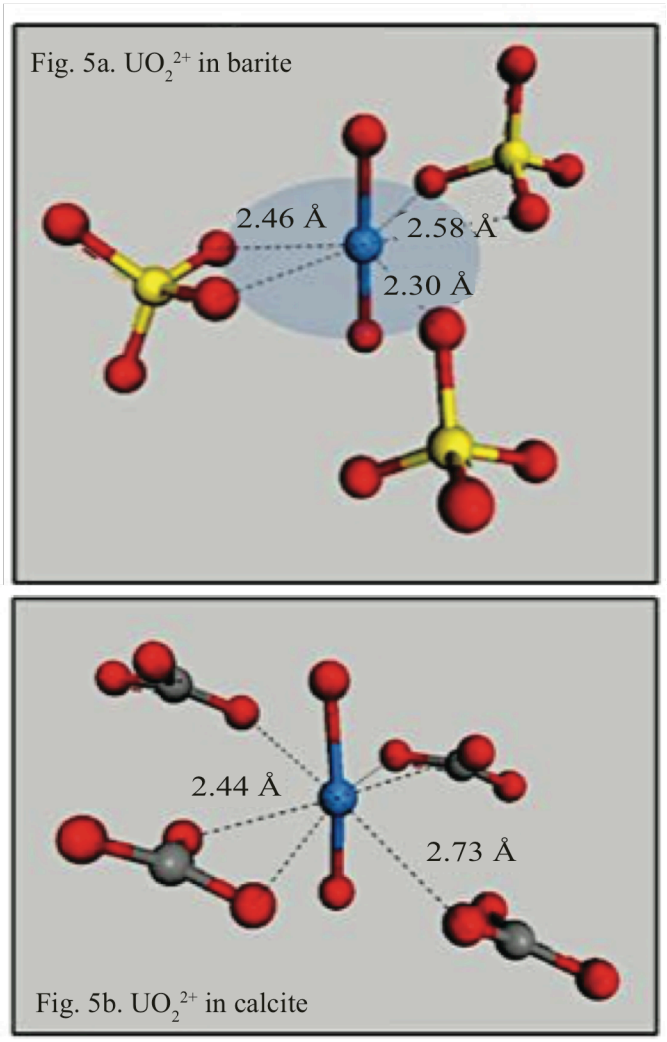

Figure 2. 5. UO_2^{2+} incorporated into barite (a) and calcite (b).

3.3. Thermodynamics of uranyl incorporation into carbonates in a solid solution framework

Another way to look at the relative stability of uranyl incorporation into aragonite is to compare the excess energies of uranyl-incorporated $CaCO_3$ in the aragonite and rutherfordine (UO_2CO_3) structural frameworks. The excess energies in this context provide a way to evaluate incorporation in terms of which structural arrangement is more likely to occur at certain UO_2^{2+} concentrations, or, in other words, at what uranyl concentration would one would expect a structural phase change. Rutherfordine (space group Imm2) is a pure uranyl carbonate and a secondary alteration product of uraninite

(UO_2) (Finch et al., 1999). Figure 2. 6 shows on the left the excess energy of rutherfordine with all the uranyl groups replaced by Ca^{2+} (labeled A) and is defined as zero. Pure rutherfordine (B) on the right hand side is also defined as zero. Without uranyl, aragonite is about 1.3 eV per cation more energetically favorable than rutherfordine with all uranyl replaced by Ca^{2+}. However, at a uranyl mole fraction of about 0.37, the two lines cross and at higher mole fractions, the rutherfordine framework is more energetically favorable than the aragonite framework.

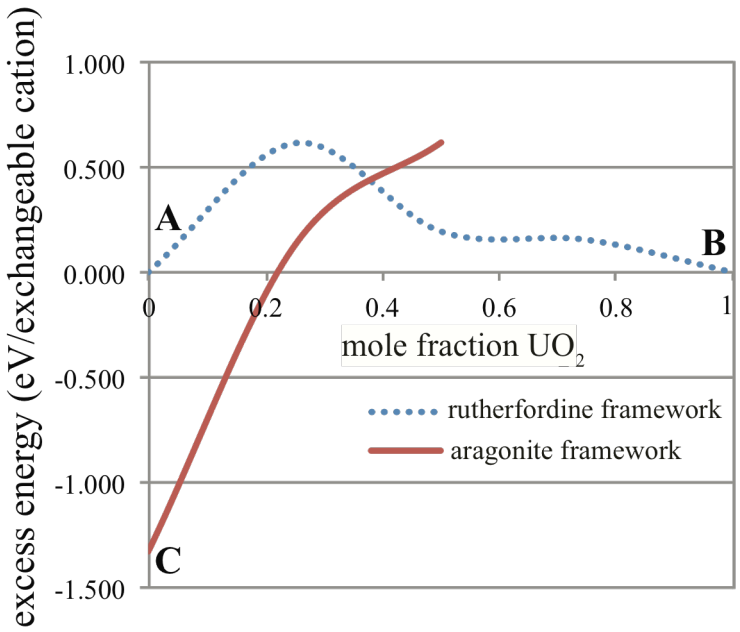

Figure 2. 6. Excess energy showing the relative stability of uranyl incorporation into aragonite (solid line) vs. Ca^{2+}incorporation into rutherfordine (dotted line). The reference energy (i.e., zero excess energy) is the line connecting the energy of rutherfordine with all uranyl replaced by Ca (A) and the energy of rutherfordine UO_2CO_3 (B). Due to the difference in excess energies, pure $CaCO_3$ is more stable in the aragonite structure framework (C) as compared with the rutherfordine framework (A). At a uranyl mole fraction of 1 (B), rutherfordine (UO_2CO_3) is the more stable phase. The transition between the aragonite and the rutherfordine structure occurs at ca. 0.37 mol fraction of UO_2^{2+}.

3.4. Electronic configuration of UO_2^{2+}- and NpO_2^{+}- incorporated phases

Partial density of states (PDOS) spectra and orbital projections are used as one way to analyze the electronic structures of uranyl and neptunyl-incorporated minerals. The partial (or often called the projected) density of describes which atoms and orbitals provide electronic states over a given range of the energy spectrum of a system. Here, individual contributions to the total density of states are resolved according to the angular momentum, which allows for the assignment of s, p, d, or f character of the orbital. The PDOS spectrum for the mineral anhydrite before uranyl/neptunyl incorporation is shown in Figure 2. 7. Orbital contributions for each peak are labeled, including the contributions from the O 2 s and S 3 s bonding and antibonding orbitals. Upon incorporation, the peak associated with the energy contribution from the Ca s orbital (ca. −37 eV for pure anhydrite) splits and shifts to the left, particularly for NpO_2^{+} incorporation (Figure 2. 8). The band gap decreases from 6.39 eV to 2.24 eV (uranyl-incorporated anhydrite) and 1.04 eV (neptunyl-incorporated) due to the infilling of U and Np 5f orbital contributions. Electron energy contributions in the inner valence band (between ca. −25 and −15 eV) display the most significant variation between uranyl and neptunyl incorporation. Anhydrite incorporates uranyl into the structure more favorably (ΔE_{rxn} = 0.68 eV) than it does neptunyl (ΔE_{rxn} = 1.84 eV). Both PDOS spectra indicate correlation between the sulfate O 2p orbital contribution and the U/Np 6d and 5f orbital contributions just below the Fermi level (E_{Fermi} = 0 eV).

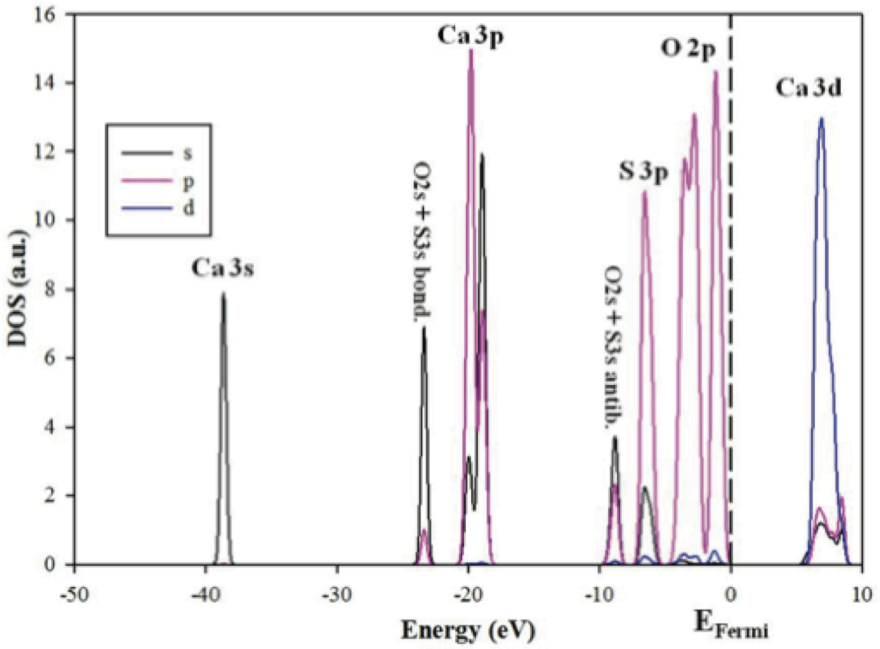

Figure 2. 7. PDOS spectra for anhydrite without actinyl incorporation.

Aragonite has a more favorable neptunyl incorporation energy (ΔE_{rxn} = 0.10 eV) compared to the uranyl incorporation energy (ΔE_{rxn} = 0.27 eV). Figure 2. 9 illustrates the electronic interaction between Np and carbonate O atoms in neptunyl-incorporated aragonite. The orbital shown in Figure 2. 9B is a π-bonding orbital and demonstrates the partial covalency of the bond between Np 5f orbitals and carbonate O 2p orbitals. This orbital is approximately 1.3 eV below the Fermi level (E_{Fermi} = 0 eV). Bonding orbitals between the other coordinating O atoms and the actinides have similar binding energies (energy eigenvalues). Figure 2. 9C depicts the highest occupied molecular orbital (HOMO) (ca. −0.8 eV), which is a non-bonding orbital as shown by the lack of overlap between the eight-lobed Np 5f orbital and the O 2p orbitals. The PDOS projection (Figure 2. 9A) shows that the contribution from Np 5f orbitals fills in the top portion of the valence band, just below the Fermi level, and reduces the band gap from approximately 4 eV to 1.5 eV.

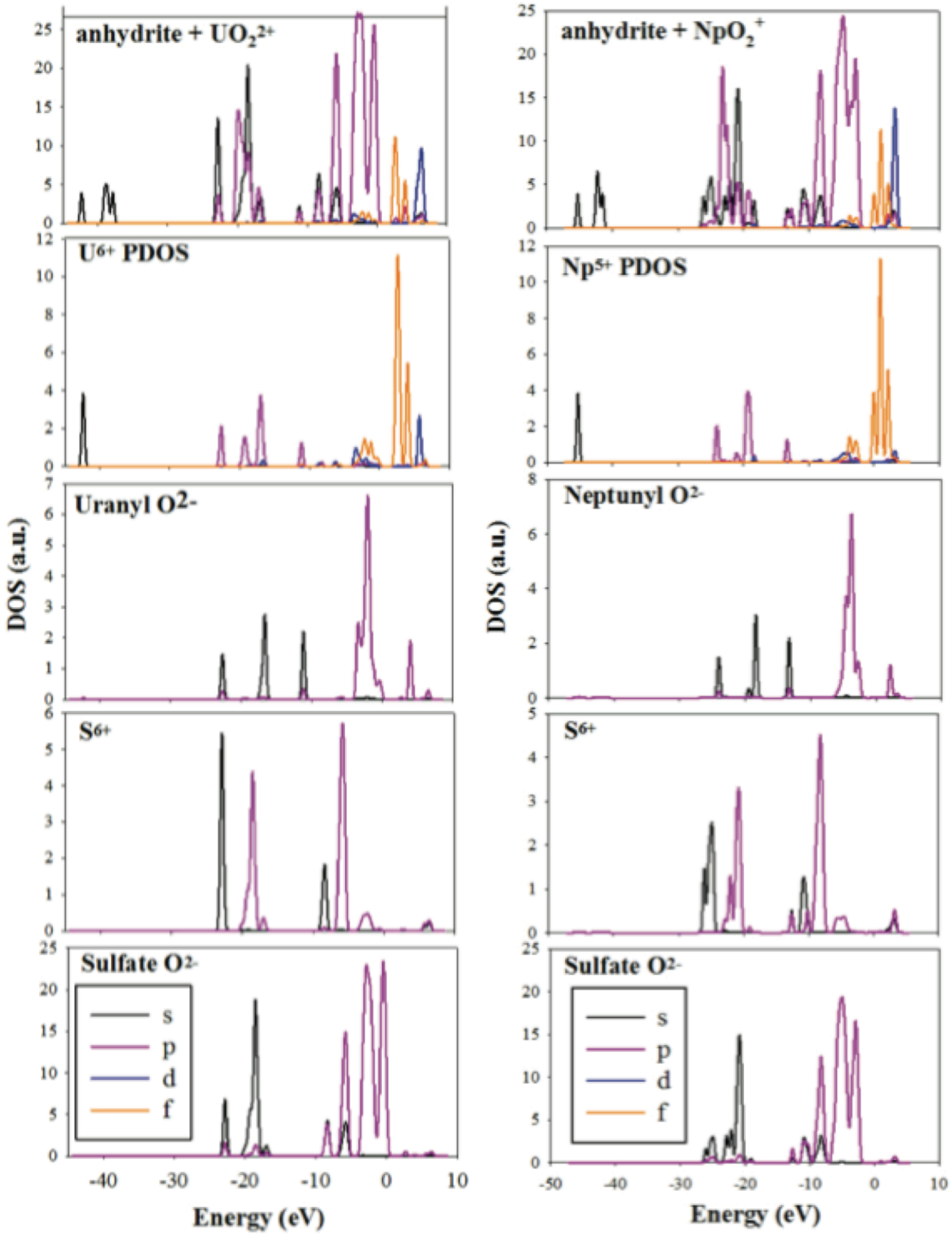

Figure 2. 8. Partial density of states (PDOS) spectra of uranyl and neptunyl-incorporated anhydrite. Of note is the correlation between actinide f orbital and sulfate oxygen 3p orbital contributions as well as different electron density contributions in the inner valence band (−25 to −15 eV).

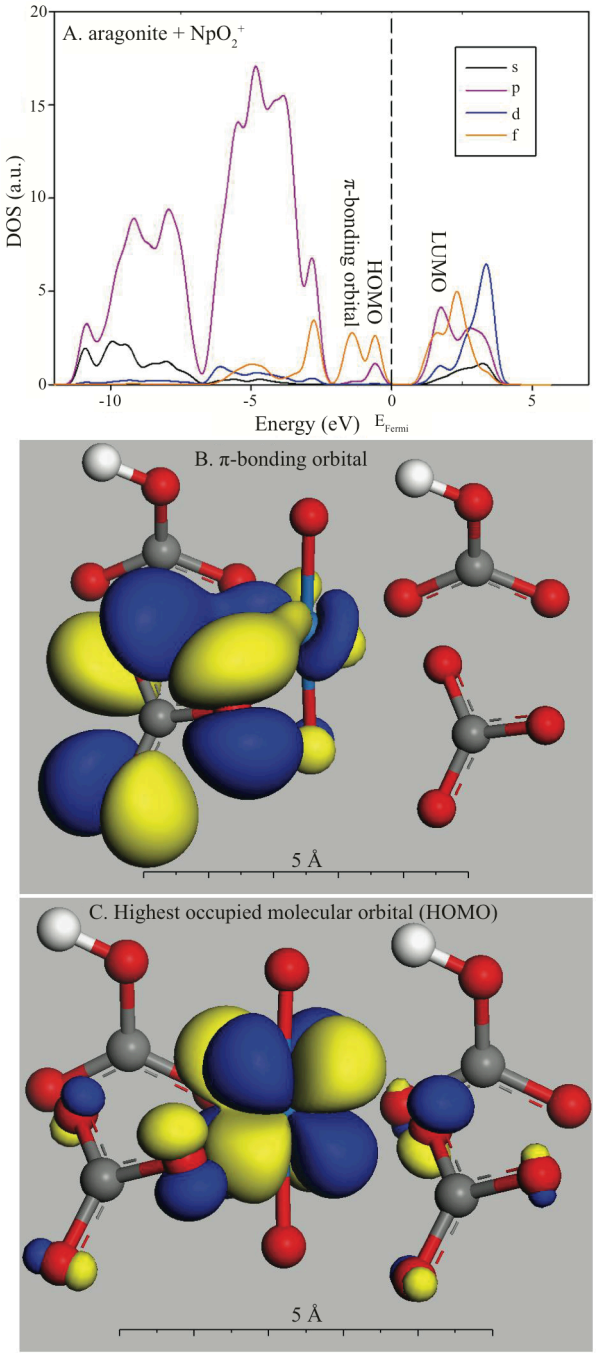

Figure 2. 9. The electronic structure of NpO_2^+ in aragonite. (a) Partial density of states (PDOS) spectra for the energy range −10 eV to 10 eV. (b) Wavefunction ($E = -1.3$ eV) with π-bonding between carbonate O 2p and Np 5f orbitals (other 3 π-bonding orbitals with comparable energies are not shown). (c) Highest occupied molecular orbital projection. No overlap between the carbonate O 2p orbitals and the eight-lobed Np 5f orbital indicates that this is a non-bonding orbital.

3.5. Vibrational entropy of solids and other sources of entropy

The vibrational entropies of solids were computed using the phonon module of the quantum mechanical code, DMol[3], using Eq. (2.4). Due to high computational expense, the vibrational entropy was only calculated for a subset of minerals, anglesite (5.93×10^{-3} eV K^{-1}), barite (4.76×10^{-3} eV K^{-1}), and calcite (5.22×10^{-3} eV K^{-1}), and the vibrational entropy reduces the Gibbs free energy of incorporation from its respective enthalpy at 300 K by 0.04 eV, 0.02 eV, and 0.01 eV, respectively. One would expect the entropy of the host mineral to increase upon incorporation, as the "perfect" crystal structure is disrupted by the incorporation of a relatively large uranyl or neptunyl (plus hydrogen) ion. More vibrational modes are available in the incorporated phase. While the magnitude of this value may be small, this entropic contribution to the Gibb's free energy may cause a significant change in the reaction's thermodynamic favorability, especially if equilibrium constants are calculated.

Considering the relative importance of the vibrational entropy of solid phases, it is prudent to consider other sources of ΔS in the incorporation process. One notable source is the change in entropy associated with hydration. When an ion becomes hydrated, the water molecules in the first few hydration spheres surrounding the ion of interest orient themselves with respect to the charge of the ion and their polarity. This local ordering can considerably lower the entropy of the solvent and decrease the overall favorability of the incorporation of aqueous species. There are some treatments of hydration energy, both computational and experimental, that take this ordering into account. Depending on the computational (or even experimental) methods used, hydration energies may be listed as ΔG, ΔH, or even some other thermodynamic quantity representing hydration. Careful attention is advised when extracting these values from the literature, as the treatment of

hydration energy is a relatively large source of error in the computation of the overall incorporation energy. For instance, computational hydration energy methods that are based on a combination of one explicit hydration shell using water molecules (with mainly contributions to ΔH) and a surrounding dielectric continuum (that has been calibrated for ΔG) may produce a hybrid of both thermodynamic parameters with entropy contributions that are difficult to deconvolute. Another separate source of entropy is any imbalance between the number of reactants and the number of products. For example, Eq. (2.2), which describes the neptunyl incorporation with solid sources and sinks, has three reactants and only two product species. In this case, one would expect the entropy to decrease. If the opposite takes place (i.e., the number of products is greater than the number of reactants), entropy would increase upon incorporation.

4. Challenges and potential sources of error

With this approach, interactions between dissolved species in solution and solid materials can be described with quantum mechanics; however, it is important to recognize potential sources of error. As with any quantum–mechanical method, the choice of high quality basis sets (or high energy cutoffs for planewave calculations), appropriate density functional, *k*-point density for periodic calculations, and the application of other corrections, such as relativistic effects, appropriate treatment of strongly correlated systems, and, if required, spin–orbit coupling, helps to ensure the highest degree of accuracy, particularly for the calculations of the host mineral, the incorporated mineral phase as well as the solid oxide sources and sinks. For the aqueous species, the treatment of hydration energy amounts to the greatest potential source of error. One particular issue is that hydration energy can be calculated with several approaches, *e.g.*, static quantum–mechanical or classical empirical force-field methods or

molecular dynamics based on either quantum–mechanical or classical principles. In addition, the hydrated molecule or ion can be embedded in a dielectric fluid (using PCM, C-PCM, IEF-PCM methods, to name a few) to account for the long-range electronic effects of the solvent (Tomasi et al., 2005). Ideally, these calculations are benchmarked with experimental data; however, hydration thermodynamics for the actinides are notably lacking in the literature. This variability in the type of hydration energy and their complexes at different oxidation states can lead to a significant accumulation of error in the overall incorporation energy.

Future improvement of the accuracy of incorporation calculations can also involve the careful, but computationally expensive, evaluation of incorporation energies as a function of unit cell size, and therefore, as a function of concentration. The relatively small unit cell sizes used in this study (with one in four cations replaced by an actinyl cation) allow for significant relaxation of the cell. Larger unit cells allow for more relaxation *within* the unit cell, and the high number of unperturbed atoms around the incorporation site keeps the overall size and shape (*i.e.*, angles) more constant, reflecting the constraints of the surrounding bulk. However, it is expected that an increase of the unit cell size has to be significant in order to allow for the relaxation around the perturbation, specifically the incorporation site, to dissipate completely within the supercell. If we assume that the supercell size would have to be at least $4 \times 4 \times 4$ in order to host the entire relaxation cascade, that would increase the unit cell size by a factor of 64 and the computational cost by a factor of about 250,000 which is prohibitive. In contrast, calculations using smaller unit cells allow for more relaxation *of* the unit cell. There is a trade-off in either of the two approaches, and careful evaluation of this may be

able to give some insight into the dependence of the thermodynamics as a function of unit cell size and concentration.

An additional challenge is the validation of this method against experimental data, namely what types of results from computational models and calculations can be compared with experiments. Possible points of comparison include the structure and lattice distortion of the incorporated phase, the bonding environment of the incorporated actinide, potential changes in the electronic configuration of the host mineral (otherwise known as "doping"), and the thermodynamics of incorporation expressed as the thermodynamic limit of incorporation, or the maximum extent of incorporation at equilibrium conditions. While co-precipitation experiments and subsequent analyses offer ways to probe these results (*e.g.*, XANES and EXAFS can identify specific coordination environments and nearest neighbor distances, conductivity experiments and ultraviolet photoelectron spectroscopy can verify changes in electronic structure of the incorporated host, and mass spectrometry can measure concentrations of the incorporated ion), it is difficult to verify if experiments have achieved equilibrium conditions. Ideal experimental analogues are those that allow for large amounts of incorporation (*i.e.*, up to several percent), reach equilibrium within a reasonable amount of time, and can be structurally and electronically analyzed.

5. Conclusions

By combining different types of quantum–mechanical calculations under uniform computational theory, the incorporation of radionuclide contaminants into minerals can be modeled as the interaction between ionic species in solution and periodic solids. Transitioning from solid to aqueous source and sink phases generally lowers the

incorporation energy by about 1.5 eV, because more energy is gained with the hydration of an alkaline earth element than with the dehydration of an actinyl ion. All incorporation reactions considered in this work are endothermic, although less so than one might expect from considering that a fairly large linear uranyl molecule replaces a smaller spherical cation, especially when coupled substitution of $NpO_2^+ + H^+$ replaces a divalent cation. Uranyl incorporation energies range from 0.19 eV (gypsum) to 2.84 eV (barite), while energies for neptunyl incorporation range from 0.10 eV (aragonite) to 2.27 eV (strontianite). Geometry optimizations present possible coordination environments and show how host anions reorient to accommodate the distortion of the unit cell. Our investigation of uranyl and neptunyl incorporation into pre-existing defects in the mineral structure reveals that incorporation occurs preferentially at these high-energy sites, and reaction energies even become exothermic in some cases. With regard to electronic structure, the incorporation of UO_2^{2+} and NpO_2^+ results in a decrease in the band cap (between 3 and 5 eV), and bonding occurs primarily between the actinide 5f and host-mineral anion O 2p orbitals. The contribution of the vibrational entropy to the overall reaction energy is relatively small in comparison with other potential sources of error, in particular the calculation or experimental determination of hydration energy and the choice of computational parameters.

Despite different sources of error, this approach to modeling incorporation reactions facilitates the evaluation of chemical properties in a way that is independent and complimentary to experimental studies. In addition, this method provides determination of equilibrium conditions while incorporation experiments, such as co-precipitation studies, typically suffer from a lack of time to reach such conditions. Understanding the

thermodynamic end point of a reaction is valuable given that federal mandates require the prediction of repository conditions at million-year time scales. However, in order to reach this goal from a computational point of view, the community may have to work on improving certain aspects such as hydration energy, changes in entropy, and optimized computational parameters for such calculations. This approach can then become a key tool to not only help interpret co-precipitation experiments, but also other geologic processes involving minerals and hydrated ions in solution, including precipitation, dissolution, and aqueous solution–solid solution formation.

Appendix 2.A

Table 2.A. 1. Uranyl (UO_2^{2+}) incorporation into anglesite

Solid oxide source and sink phases

$(PbSO_4)_{4(s)} + UO_{3(s)} \rightarrow Pb_3UO_2(SO_4)_{4(s)} + PbO_{(s)}$ $\Delta E = 1.52$ eV

Solid source and sink to gas-phase molecules with periodic boundary conditions

$UO_2(OH)_{2(pbc\ m)} \rightarrow UO_{3(s)} + H_2O_{(pbc\ m)}$ $\Delta E = -1.58$ eV

$PbO_{(s)} + H_2O_{(pbc\ m)} \rightarrow Pb(OH)_{2(pbc\ m)}$ $\Delta E = 0.62$ eV

Transition to neutral molecular species without periodic boundary conditions

$UO_2(OH)_{2(clus)} \rightarrow UO_2(OH)_{2(pbc\ m)}$ $\Delta E = 0.002$ eV

$Pb(OH)_{2(pbc\ m)} + H_2O_{(clus)} \rightarrow Pb(OH)_{2(clus.)} + H_2O_{(pbc\ m)}$ $\Delta E = 0.020$ eV

Dissociation and ionization

$UO_2^{2+}{}_{(clus)} + 2\ OH^-_{(clus)} \rightarrow UO_2(OH)_{2(clus)}$ $\Delta E = -29.26$ eV

$Pb(OH)_{2(clus)} \rightarrow Pb^{2+}{}_{(clus)} + 2OH^-_{(clus)}$ $\Delta E = 26.54$ eV

Hydration

$UO_2^{2+}{}_{(aq)} \rightarrow UO_2^{2+}{}_{(clus)}$ $\Delta E = 18.02$ eV

$Pb^{2+}{}_{(clus)} \rightarrow Pb^{2+}{}_{(aq)}$ (calc.) $\Delta E = -11.78$ eV

$Pb^{2+}{}_{(clus)} \rightarrow Pb^{2+}{}_{(aq)}$ (exp.[a]) $\Delta E = -14.77$ eV

Overall reaction

$(PbSO_4)_{4(s)} + UO_2^{2+}{}_{(aq)} \rightarrow Pb_3UO_2(SO_4)_{4(s)} + Pb^{2+}{}_{(aq)}$ $\Delta E = 1.11$ eV

pbc m = molecule/cluster with periodic boundary conditions, "molecule in a box"

clus = cluster/molecule in vacuum (gas phase)

aq = hydrated (non-periodic) cluster, aqueous ion

[a] experimental value from MARCUS which has been used for the sum in the overall equation rather than the calculated value above

References

Allen P. G., Bucher J. J., Clark D. L., Edelstein N. M., Ekberg S. A., Gohdes J. W., Hudson E. A., Kaltsoyannis N. and Lukens W. W. (1995) Multinuclear NMR, Raman, EXAFS, and X-ray diffraction studies of uranyl carbonate complexes in near-neutral aqueous solution. X-ray structure of $[C(NH_2)_2]_6[(UO_2)_3(CO_3)_6]\bullet 6.5H_2O$. *Inorg. Chem.* **34**, 4797–4807.

Andzelm J., Kölmel C. and Klamt A. (1995) Incorporation of solvent effects into density functional calculations of molecular energies and geometries. *J. Chem. Phys.* **103**, 9312–9320.

Antonio M. R., Soderholm L., Williams C. W., Blaudeau J. P. and Bursten B. E. (2001) Neptunium redox speciation. *Radiochim. acta* **89**, 17–25.

Atkinson A. (1985) The time dependence of pH within a repository for radioactive waste disposal. *United Kingdom At. Energy Res. Establ. Rep. AERE-R117777*.

Balboni E., Morrison J. M., Wang Z., Engelhard M. H. and Burns P. C. (2015) Incorporation of Np(V) and U(VI) in carbonate and sulfate minerals crystallized from aqueous solution. *Geochim. Cosmochim. Acta* **151**, 133–149.

Bruno J., Bosbach D., Kulik D. and Navrotsky A. (2007) Chemical thermodynamics of solid solutions of interest in radioactive waste management. *OECD Nucl. Energy Agency Rep.*

Burns P. C., Ewing R. C. and Miller M. L. (1997) Incorporation mechanisms of actinide elements into the structures of U^{6+} phases formed during the oxidation of spent nuclear fuel. *J. Nucl. Mater.* **245**, 1–9.

Delley B. (1990) An all-electron numerical method for solving the local density functional for polyatomic molecules. *J. Chem. Phys.* **92**, 508–517.

Demichelis R., Civalleri B., D'Arco P. and Dovesi R. (2010) Performance of 12 DFT functionals in the study of crystal systems: Al_2SiO_5 orthosilicates and Al hydroxides as a case study. *Int. J. Quantum Chem.* **110**, 2260–2273.

Dolg M., Wedig U., Stoll H. and Preuss H. (1987) Energy-adjusted ab initio pseudopotentials for the first row transition elements. *J. Chem. Phys.* **86**, 866–872.

Finch R. J., Cooper M. A., Hawthorne F. C. and Ewing R. C. (1999) Refinement of the crystal structure of rutherfordine. *Can. Mineral.* **37**, 929–938.

Fortier S. and Hayton T. W. (2010) Oxo ligand functionalization in the uranyl ion (UO_2^{2+}). *Coord. Chem. Rev.* **254**, 197–214.

Görller-Walrand C. and Colen W. (1982) On the coordination symmetry of the hydrated uranyl ion. *Chem. Phys. Lett.* **93**, 82–85.

Gutowski K. E. and Dixon D. D. (2006) Predicting the energy of the water exchange reaction and free energy of solvation for the uranyl ion in aqueous solution. *J. Phys. Chem. A* **110**, 8840–8856.

Hawthorne F. C. and Ferguson R. B. (1975) Anhydrous sulphates, I: Refinement of the crystal structure of celestite with an appendix on the structure of thenardite. *Can. Mineral.* **13**, 181–187.

Heberling F., Denecke M. A. and Bosback D. (2008) Neptunium(V) coprecipitation with calcite. *Environ. Sci. Technol.* **42**, 471–476.

Hirano T. (1993) MOPAC Manual (Seventh Edition) ed. J. J. P. Stewart.

Kerisit S., Felmy A. R. and Ilton E. S. (2011) Atomistic simulations of uranium incorporation into iron (hydr)oxides. *Environ. Sci. Technol.* **45**, 2770–2776.

Klamt A. and Schuurmann G. (1993) COSMO: a new approach to dielectric screening in solvents with explicit expressions for the screening energy and its gradient. *J. Chem. Soc. Perkin Trans. 2* **0**, 799–805.

Kröger F. A. (1985) Point Defects in Solids: Physics, Chemistry, and Thermodynamics. In *Point Defects in Minerals* American Geophysical Union. pp. 1–17.

Kubicki J., Halada G., Jha P. and Phillips B. (2009) Quantum mechanical calculation of aqueuous uranium complexes: carbonate, phosphate, organic and biomolecular species. *Chem. Cent. J.* **3**, 1–29.

Marcus Y. (1994) A simple empirical model describing the thermodynamics of hydration of ions of widely varying charges, sizes, and shapes. *Biophys. Chem.* **51**, 111–127.

Nico P. S., Stewart B. D. and Fendorf S. (2009) Incorporation of oxidized uranium into Fe (hydr)oxides during Fe(II) catalyzed remineralization. *Environ. Sci. Technol.* **43**, 7391–7396.

Pedersen B. F. and Semmingsen D. (1982) Neutron diffraction refinement of the structure of gypsum, $CaSO_4 \cdot 2H_2O$. *Acta Crystallogr. Sect. B* **38**, 1074–1077.

Perdew J. P., Burke K. and Ernzerhof M. (1996) Generalized gradient approximation made simple. *Phys. Rev. Lett.* **77**, 3865–3868.

Pfrommer B. G., Côté M., Louie S. G. and Cohen M. L. (1997) Relaxation of crystals with the quasi-newton method. *J. Comput. Phys.* **131**, 233–240.

Rák Z., Ewing R. C. and Becker U. (2013) Electronic structure and thermodynamic stability of uranium-doped yttrium iron garnet. *J. Phys. Condens. Matter* **25**, 495502.

Rák Z., Ewing R. C. and Becker U. (2013) Ferric garnet matrices for immobilization of actinides. *J. Nucl. Mater.* **436**, 1–7.

Rák Z., Ewing R. C. and Becker U. (2011) Role of iron in the incorporation of uranium in ferric garnet matrices. *Phys. Rev. B* **84**, 155128.

Reeder R. J., Elzinga E. J., Tait C. D., Rector K. D., Donohoe R. J. and Morris D. E. (2004) Site-specific incorporation of uranyl carbonate species at the calcite surface. *Geochim. Cosmochim. Acta* **68**, 4799–4808.

Reeder R. J., Nugent M., Lamble G. M., Tait C. D. and Morris D. E. (2000) Uranyl incorporation into calcite and aragonite:, XAFS and luminescence studies. *Environ. Sci. Technol.* **34**, 638–644.

Reeder R. J., Nugent M., Tait C. D., Morris D. E., Heald S. M., Beck K. M., Hess W. P. and Lanzirotti A. (2001) Coprecipitation of uranium(VI) with calcite: XAFS, micro-XAS, and luminescence characterization. *Geochim. Cosmochim. Acta* **65**, 3491–3503.

Renock D., Mueller M., Yuan K., Ewing R. C. and Becker U. (2013) The energetics and kinetics of uranyl reduction on pyrite, hematite, and magnetite surfaces: A powder microelectrode study. *Geochim. Cosmochim. Acta* **118**, 56–71.

Segall M. D., Lindan P. J. D., Probert M. J., Pickard C. J., Hasnip P. J., Clark S. J. and Payne M. C. (2002) First-principles simulation: ideas, illustrations and the CASTEP code. *J. Phys. Condens. Matter* **14**, 2717–2744.

Shuller L. C., Ewing R. C. and Becker U. (2013) Np-incorporation into uranyl phases: A quantum-mechanical evaluation. *J. Nucl. Mater.* **434**, 440–450.

Silva R. J. and Nitsche H. (1995) Actinide environmental chemistry. *Radiochim. acta* **70/71**, 377–396.

Skomurski F. N., Rosso K. M., Krupka K. M. and McGrail B. P. (2010) Technetium incorporation into hematite (α-Fe_2O_3). *Environ. Sci. Technol.* **44**, 5855–5861.

Thompson H. A., Brown Jr G. E. and Parks G. A. (1997) XAFS spectroscopic study of uranyl coordination in solids and aqueous solution. *Am. Mineral.* **82**, 483–496.

Tomasi J., Mennucci B. and Cammi R. (2005) Quantum Mechanical Continuum Solvation Models. *Chem. Rev.* **105**, 2999–3094.

Tsushima S. and Suzuki A. (2000) Hydration numbers of pentavalent and hexavalent uranyl, neptunyl, and plutonyl. *J. Mol. Struct. THEOCHEM* **529**, 21–25.

Vanderbilt D. (1990) Soft self-consistent pseudopotentials in a generalized eigenvalue formalism. *Phys. Rev. B* **41**, 7892–7895.

Wilson E. B., Decuis J. C. and Cross P. C. (1980) *Molecular Vibrations: the Theory of Infrared and Raman Vibrational Spectra*., Dover, New York.

Wu Z. and Cohen R. E. (2006) More accurate generalized gradient approximation for solids. *Phys. Rev. B* **73**, 235116.

CHAPTER 3
Imaging the reduction of chromium (VI) on magnetite surfaces using *in situ* electrochemical AFM

Abstract

Hexavalent chromium is a highly toxic and readily mobile metal contaminant introduced to the environment through a variety of industrial operations. In the presence of reductants, such as Fe(II), and catalytic mineral surfaces, such as iron oxides surfaces, Cr(VI) may be reduced to a less toxic and relatively insoluble form Cr(III). In this study, we investigate the interaction between Cr(VI) and the surface of the Fe(II)-bearing mineral magnetite, $Fe(II)Fe(III)_2O_4$, as an example catalyst, using electrochemical atomic force microscopy (EC-AFM). With this method, the redox potential is controlled by an electrode, and Cr deposition on the magnetite surface is imaged over time as a function of redox potential and pH of the solution. Quantitative analyses of volumetric growth and surface coverage reveal that more precipitation occurs over time at very negative (− 500 mV at pH 3, − 750 mV at pH 7, and − 1000 mV at pH 11) and very positive (+ 1000 mV at pH 3 and + 500 mV at pH 11) electrochemical potentials. Up to 70% of the surface is covered with precipitates at pH 7, while less coverage is observed at pH 11 (< 8%) and pH 3 (< 2%). Particle growth at pH 3 is predominantly lateral in nature with a tendency to form a higher number of smaller adsorbate particles. At pH 11, growth is primarily vertical (perpendicular to the surface), and smaller particles tend to aggregate into larger clusters on the surface with increasingly negative redox polarization. These larger clusters (most likely subcrystalline Cr-(oxy)hydroxides) co-exist with rhombic,

crystalline particles that likely have preferred crystallographic growth relationships with the magnetite substrate; the composition of this latter type of particle is most likely chromite, $FeCr_2O_4$, based on the matching crystallography and stability under the Eh/pH conditions of this experiment.

Results from growth analyses were confirmed by batch experiments performed on the same samples used in the AFM, where changes in the Cr concentration in solution were monitored using inductively coupled plasma mass spectrometry (ICP-MS). Virtually all of the Cr was removed after 30 min at pH 7 (starting at 2 μM Cr(VI)) at all potentials, ~ 60% at pH 3, and very little removal at pH 11. X-ray photoelectron spectroscopy (XPS) analyses of the magnetite surface at pH 3 suggest that only Cr(III) phases are present and that Cr and/or Fe–Cr oxide phases are more stable at very reducing conditions (− 750 mV), while Cr and/or Fe–Cr (oxy)hydroxide phases are present under more moderately-reducing conditions (− 250 mV). At pH 11, any Cr deposited is below the detection limit for XPS analysis (< 1% surface coverage); however, Fe(II)/Fe(III) ratios (~ 0.3) are lower than the expected ratio of magnetite, which indicates that some oxidation of the surface has occurred. This oxidized layer, possibly maghemite (γ-Fe_2O_3), hematite (α-Fe_2O_3), or FeOOH, may inhibit the reduction of Cr(VI) on the surface.

1. Introduction

Chromium, like most transition metals, is redox-active and shows variable geochemical behavior with changes in oxidation state (typically III or VI). Under reducing conditions, Cr is present as Cr(III) and occurs naturally as the mineral ore chromite ($FeCr_2O_4$). Cr(III) may also precipitate as Cr_2O_3 (eskolaite) or as Cr(III)-

hydroxides in aqueous environments at pH > 3. The oxidized form of chromium, Cr(VI), however, is highly carcinogenic and exists primarily as dissolved chromate ($CrO_4^{2-}{}_{(aq)}$), dichromate ($Cr_2O_7^{2-}{}_{(aq)}$), or as rare chromate solids (e.g., crocoite, $PbCrO_4$). Cr(VI) persists in soils and natural waters indefinitely unless removed through leaching, uptake into the cells of plants and microorganisms, adsorption, or reduction and subsequent precipitation of Cr(III) phases (Bartlett, 1991). The World Health Organization proposes a maximum allowable limit of 50 $\mu g\ L^{-1}$ (about 1 μM) total chromium in drinking water (WHO, 2011).

In the context of environmental contamination, Cr(VI) poses a significant hazard, while Cr(III) is relatively benign at low concentrations. Therefore, a detailed understanding of the redox transformations between Cr(VI) and Cr(III) has important implications for the chemical sequestration and remediation of chromium. Electron donors available to promote Cr reduction, e.g., dissolved organic matter or $Fe(II)_{(aq)}$, are relatively common; however, mineral surfaces are often needed to promote these redox reactions. Atoms at the surfaces of minerals may accept or donate electrons as active participants in the redox reactions, or the mineral surface may serve as a catalyst for the reaction by facilitating electron transfer via an electron shuttle through the surface. Furthermore, mineral surfaces may help lower the activation energy of the overall reaction by providing nucleation or adsorption sites for species in solution (Tessis et al., 1999; Becker et al., 2001; Vorlicek and Helz, 2002; Rosso and Becker, 2003). Minerals that are ubiquitous in aqueous environments, including sulfide minerals and Fe or Mn oxides/(oxy)hydroxides, play a critical role in surface-mediated reduction (Hyland and Bancroft, 1990; Elsner et al., 2004; Taylor et al., 2015). Macroscale kinetic experiments

have demonstrated that these redox reactions are often catalyzed by the surfaces of sulfide and oxide minerals, yet the actual nanoscale reaction mechanisms are not understood (Gheju, 2011). Kinetic bottlenecks may include diffusion of chromate towards the mineral surface, dehydration of the chromate and reductant, outer- to inner-sphere surface complex transitions, and associated angular momentum changes due to electron-spin transfer (Renock and Becker, 2010). In order to clarify these atomic-scale processes, high-resolution microscopy and surface-sensitive analytical techniques are needed.

One way to observe the progress of a reduction/precipitation reaction is to study the formation of the reduction product as a function of solution chemistry and redox potential. In this study, atomic force microscopy (AFM) in combination with electrochemical methods (EC-AFM) has been developed and applied to image the reductive precipitation of Cr on a mineral surface. In our approach, the solution chemistry (i.e., pH, Cr concentration, type and concentration of background electrolyte) is constrained within an experimental cell (although slight modulations in the pH are inherent to the nature of redox reactions), and the redox potential is controlled by setting the voltage of a potentiostat for a given amount of time. This type of redox-dependent scanning probe microscopy, or electrochemical-SPM (EC-SPM) allows for in situ observations of reactions along a given Eh/pH path. Although homogenous reduction of Cr(VI) by Fe(II) in solution has been observed (Buerge and Hug, 1997; Flury et al., 2009), we focus on surface-mediated, heterogeneous reduction, because the experimental conditions can be controlled, and the reaction products can be studied with EC-AFM. EC-SPM has been used relatively rarely for geochemical applications, but this combined

method has been a powerful tool in studying processes such as epitaxial mineral growth (Stack, Erni, et al., 2004), mineral dissolution morphology and kinetics (Higgins and Hamers, 1995; Higgins et al., 1996; Higgins and Hamers, 1996; Etienne et al., 2004), precipitation (Yuan et al., 2015), adsorption and thin film formation (Stack, Eggleston, et al., 2004; Stack, 2008), and electron transfer (Wigginton et al., 2009).

Here, EC-AFM is used to visualize the in situ adsorption/precipitation/reduction of Cr(VI) onto a magnetite (Fe_3O_4) surface. Magnetite is a mixed valence iron oxide mineral and is a major constituent of many different types of soil environments (Cornell and Schwertmann, 2006). Additionally, magnetite has been shown to facilitate the heterogeneous reduction of Cr(VI) to Cr(III) (White and Peterson, 1996; Peterson et al., 1997; Kendelewicz et al., 1999; Fendorf et al., 2000; Kendelewicz et al., 2000; Jung et al., 2007; Gheju, 2011; Baig et al., 2014). When Cr(VI) in solution is reduced to Cr(III), there is an associated change in angular momentum when its unpaired spins change from 0 to 3. Magnetite, which has both ferric (five unpaired spins) and ferrous (four unpaired spins) iron, can compensate for this change in angular momentum. In order to precisely control the redox potential of the electrochemical cell, the electrode material/substrate of interest has to be adequately conductive to allow for the transfer of electrons from a voltage source to solution (or vice versa). Magnetite is a semiconducting mineral (with a band gap of 0.1 eV) and, therefore, well suited as a substrate to study surface-mediated redox reactions. In these experiments, a magnetite sample is loaded into an EC-AFM cell and polarized at discrete redox potentials in the presence of a Cr(VI)-containing solution. Morphological changes in the magnetite surface and kinetic information are measured in

terms of changes in the volume growth of Cr adsorbates/precipitates, the number of adsorbates/precipitates per unit area, or a combination thereof.

The goal is to observe, understand, and quantify Cr(VI) reduction and adsorption/precipitation onto magnetite at specific Eh and pH conditions. The Eh and pH are set by the applied electrochemical potential and the initial acid/base content in solution, respectively, and the progress of the reaction is monitored by imaging the magnetite surface over time. Redox equilibrium diagrams are useful for evaluating which species is predominant over a range of pH and Eh conditions and what process is being observed (Figure 3. 1); however, many redox reactions are very slow, and disequilibrium may occur when multiple redox couples are present. As a result of this, a reduction (or

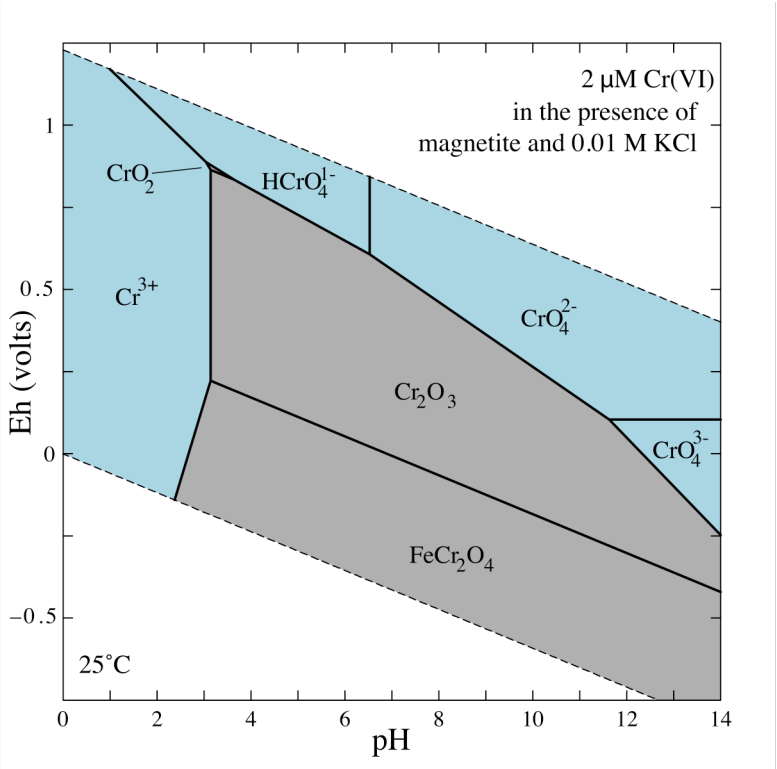

Figure 3. 1. Eh–pH diagram of chromium at the experimental conditions (2 µM chromate solution). Modeled with Geochemists' Workbench LLNL thermodynamic database.

oxidation) process may be observed at a redox potential that is actually lower (or higher) than expected from equilibrium conditions. In addition, it is possible that the dominant species predicted by the Nernst equation is less redox-active than other species or even redox-inactive. By measuring precipitation over time, we can compare the growth features that appear at the time scale of these experiments (i.e., minutes to hours) with the species predicted at thermodynamic equilibrium. We can also observe the morphology of adsorbates or precipitates on the surface and see how it changes over time.

As a second, more methodological goal, the suitability of EC-AFM is evaluated to capture the kinetics of precipitation as a function of Eh/pH. This relatively new and underutilized approach is a way to specifically control Eh and pH and simultaneously look at growth and morphology changes in situ and in almost real time (depending on the time needed to acquire an image). This is a potentially powerful tool to study geochemically relevant redox processes. Morphologic information is complemented with surface-sensitive spectroscopy (XPS and AES) in order to determine the composition of Cr precipitates and analysis of the solution to measure the amount of Cr removed. This knowledge will help develop a mechanistic model for surface-mediated reductive precipitation of Cr.

2. Methods

2.1. Electrochemical AFM experiments

The magnetite samples used in this study are octahedral–dodecahedral crystals collected from Mineville, New York and the Itabira District, Minas Gerais, Brazil (Ward's Science, USA). Minor amounts of titanium and aluminum were measured with energy-dispersive x-ray spectroscopy (EDS). The crystals were cut using a water-saw parallel to triangular (111) growth faces. The chosen faces were largely free of

inclusions. The large octahedral magnetite crystals from the Itabira District are associated with minor occurrences of high-grade hematite bodies, and impurities are generally minor. The samples were polished with silicon carbide paper (grit sizes 180, 400, 600, 800, 2400, and 4000) and 0.3 μm and 0.05 μm alumina powders in sequence. Samples were then sonicated for 10 min and rinsed with ethanol and acetone in order to remove any contaminants introduced through polishing. Samples were polished and rinsed immediately prior to EC-AFM experiments in order to expose a "fresh" surface and minimize oxidation of Fe(II) to Fe(III) on the surface. The exposed areas of the final samples were approximately 15 mm^2 to 18 mm^2.

Our experimental setup consists of a three-electrode configuration in which magnetite serves as the working electrode, a platinum wire is the counter electrode, and a silver wire is the quasi-reference electrode (+ 250 mV vs. the standard hydrogen electrode, SHE). In this electrochemical cell (Appendix 3.A, Figure 3.A 1). Bruker Corporation, Santa Barbara, California), the magnetite samples were affixed flat on an etched Teflon® disk using Torr Seal® low vapor pressure epoxy. The Teflon disk was then mounted to the base of the AFM fluid cell, and electrical contact was established with a spring through a small opening in the disk. The redox potential was controlled using a CHI 760D potentiostat, and EC-AFM experiments were performed using an in-house Dimension Icon atomic force microscope (Bruker). Electrolyte solutions were prepared using ultra-pure water (i.e., Milli-Q® water, typically 18.2 MΩ cm at 25 °C) and reagent-grade $Na_2Cr_2O_7 \cdot 2H_2O$ and KCl. The pH was adjusted using 0.01 M HCl and 0.1 M NaOH. For all experiments, the initial pH of the electrolyte solutions was approximately 3, 7, or 11; these values were chosen in order to capture a broad range of

possible pH conditions. Previous studies have shown that magnetite can reduce Cr(VI) in solution at neutral pH, although less evidence exists at more extreme pH values (Peterson et al., 1996; Peterson et al., 1997). Due to the relatively small volume of the experimental cell (2 mL), the decision was made not to use a buffering agent in order to avoid possible complexation of Cr by the buffering agent in solution or competition for surface sites on the magnetite (Sibanda and Young, 1986; Welch et al., 2002; Sokołowska and Bal, 2005). Still, in order to consider the potential pH change, we estimate the upper limit of pH change as a function of hydronium consumption described in Eqs. (3.1a) and (3.1b).

$$2CrO_4^{2-}{}_{(aq)} + 6e^- + 10H^+ \Rightarrow Cr_2O_{3(s)} + 5H_2O \quad (3.1a)$$

$$2CrO_4^{2-}{}_{(aq)} + 6e^- + 10H_2O \Rightarrow Cr_2O_{3(s)} + 5H_2O + 10OH^-_{(aq)} \quad (3.1b)$$

In the extreme case in which all the Cr in solution is reduced and none of the pH change is buffered by either the mineral surface or solution constituents, and by applying this estimate to the least pH buffered solution of pH 7, 10^{-5} M hydroxide ions would be produced (or an equal amount of hydronium consumed) in a 2 μM chromate solution. This would result in a maximum pH change of + 2 units from pH 7 to 9. This effect would be negligible at pH 3 (3 to 3.004) or pH 11 (11 to 11.004). Geochemical modeling reveals that the phases expected to dominate at pH 7 are present over several pH units in either direction, and a change in pH from 7 to 9 would not greatly affect Cr speciation in this case, but would somewhat shift the equilibrium away from Cr_2O_3 towards dissolved chromate for oxidizing conditions (Figure 3. 1). Solutions were kept in opaque bottles and refrigerated at 4 °C to minimize the possibility of photochemical redox reactions (Kleber and Helz, 1992).

Contact mode and Peak Force Tapping (PFT) mode experiments were performed in fluid (1 μM $Na_2Cr_2O_7 \cdot 2H_2O$ and 0.01 M KCl solution) using silicon nitride (DNP, nom. freq. 23 kHz, nom. spring constant 0.12 N/m) and silicon tips (ScanAsyst-Fluid +, nom. freq. 150 kHz, nom. spring constant 0.7 N/m). In PFT, developed by Bruker, the tip makes intermittent contact with the sample surface, but unlike regular tapping mode, the oscillation of the cantilever is kept at frequencies well below its resonance. This removes artifacts attributed to the dynamics of a resonating system. A linear scan rate of about 1.2 Hz was used with a resolution of 320 samples per line. For each experiment, the open circuit potential, usually between 0 and − 100 mV, was measured and allowed to stabilize for 400 s before beginning polarization of the magnetite electrode. Images were later cleaned and flattened using the NanoScope Analysis® software version 1.4 (Bruker Corp). After polarization, the experiment was stopped, and the Cr-electrolyte was removed from the cell and stored for subsequent ICP-MS analysis. The magnetite electrodes were then gently dried with compressed air, and immediately transferred into a controlled atmosphere Coy® vinyl glove box, where they continued to dry for at least 24 h before XPS and AES analysis. The gas in the box was primarily N_2 (with 5% H), and O_2 levels are < 1 ppm (controlled using a desiccant with a palladium catalyst and an O_2trap; see Taylor et al. (2015) for further details). All experiments were carried out at a temperature of 22 ± 2 °C. Both types of spectroscopic analyses were performed at the Electron Microbeam Analysis Laboratory at the University of Michigan.

A MATLAB script (release 2015a, the MathWorks, Inc., Natwick, Massachusetts, USA) was developed to quantify the precipitates observed on the AFM images. The script first estimates a background for each original grayscale image using a user-defined

structural element. This structural element is chosen to distinguish and separate features in the image. The background is then subtracted from the original grayscale image. The intensity values of the corrected grayscale image are mapped to new values, such that 1% of these data are saturated at low and high intensities creating an increased contrast output image. The high-contrast image is then converted to a black and white image based on a threshold value specified by the user. This approach was preferred over standard threshold-finding strategies (e.g., Otsu's method) because choosing a threshold allowed the visual selection of the closest-to-original result (Otsu, 1979). Objects can then be defined, measured, and counted from the binary or black and white representation of the original image. The binary image is a logical array with ones (1) where precipitates exist in the original image and zeros (0) where they do not. To obtain the precipitate heights only, this logical array is multiplied by the image height data exported from the AFM acquisition software. All heights not associated with precipitates are thus discarded. The sum of the heights that correspond to precipitates is finally multiplied by the appropriate area differential to estimate the volume of the precipitates. Importantly, defects on the magnetite surface or interference during the original image acquisition influence the numbers obtained by this method, which should be taken as estimates instead of precise values. Overall trends and differences are likely to be more relevant in this model than absolute numbers.

2.2. X-ray photoelectron spectroscopy (XPS)

Characterization of the chemical oxidation states of Cr species on the magnetite surface was performed by measuring the peak chemical shifts of the electron binding energies (BE) using a Kratos Axis Ultra XPS with an Al Kα x-ray radiation source (1486.6 eV). Before analyses, the samples were degassed overnight in a sample-transfer

chamber under a vacuum pressure of $< 10^{-5}$ Torr. Analyses were then carried out at a pressure of $< 10^{-8}$ Torr. The x-ray emission current and anode voltage used during spectra acquisition were 8 mA and 14 keV, respectively. A charge neutralizer was used during spectra acquisition. Spectra were acquired using a hybrid lens and slot aperture (700 × 300 μm). The analysis area was approximately 2 mm × 1 mm. For survey scans, a pass energy of 160 eV was used with a dwell time of 100 ms per 1 eV step (10 sweeps). Core scans were performed for the Cr 2p, Fe 2p, O 1 s, and C 1 s regions using a 20 eV pass energy and a dwell time of 400 ms per 0.1 eV step (20–50 sweeps). Spectra were analyzed using the Casa XPS software (version 2.3.16), and binding energies were calibrated to C 1s at 284.8 eV. The signal-to-noise ratio was increased by convolution using a 5-point quadratic polynomial.

2.3. Auger electron spectroscopy (AES)

Chemical analyses of the magnetite surfaces were also performed with AES. Measurements were taken using the Physical Electronics Auger Nanoprobe 680. The electron gun with a Schottky thermal field emitter was operated at a beam voltage of 10 keV and current of 10 nA. The electron energy analyzer is a full cylindrical mirror analyzer with a capture angle of 42 ± 6° for 360° around the analyzer axis. Samples were held under ultra-high vacuum (ca. 2.0×10^{-9} Torr) for the duration of analysis. Although magnetite is a semiconducting mineral, some charge from the incident electron beam may accumulate on the surface and cause shifts in electron kinetic energy; therefore, all samples were fixed onto a tilted sample mount (30°) during analysis. Tilting the sample serves to scatter electrons from the incident beam away from the surface so that only a relatively small number of electrons initiate the Auger process. Spectra were smoothed

and differentiated using the MultiPak software package, version 9.6.0 (ULVAC-PHI 2014).

2.4. Inductively-coupled plasma mass spectroscopy (ICP-MS)

Aqueous Cr(VI) concentrations were measured from the diluted, acidified aliquots of electrolyte using an Agilent 7900 ICP-MS. The quantitative analysis method uses 100 sweeps per reading and the average of three to five replicates per measurement. Interferences were minimized by using a high He flow method in the collision-reaction chamber of the instrument. The analysis was controlled using a simple linear standard calibration curve with 6 points and Ga as internal standard. Internal standard variation was never above 15%. Analytical precision was better than 7% RSD based on check standards, laboratory reference material, and sample replicates.

3. Results and Discussion

3.1. Electrochemical AFM

3.1.1. Redox processes at pH 11

The magnetite surface was first imaged in the absence of an applied potential in order to survey the substrate before any induced sorption took place and to test if sorption occurred at the open circuit potential (OCP). With this step, a "background" image is obtained with which to compare growth features that appear on the surface as a function of time and potential (Figure 3. 2A). Scratches and grooves produced when polishing the magnetite surface serve as reference points during the experiment. The magnetite electrode was then polarized at specific electrochemical potentials (− 250 mV, − 750 mV, and + 1000 mV), and the surface was imaged over a period of 20 to 35 min at each potential. In all experiments, unless otherwise stated, scanning was briefly paused between images in order to reset the potentiostat and resumed once the redox potential

was set to ensure a stable potential during image acquisition. Images were then quantified and analyzed for changes in the number and size of adsorbates and/or precipitates (hereafter collectively referred to as sorbates). While these values provide a quantitative measure of sorption over time, the level of uncertainty of the image analysis dictates that the overall trends and relative differences between potentials (rather than the absolute values) be emphasized.

At − 250 mV (vs. SHE), sorbates appear on the surface within the first 10 min of polarization. In general, these particles have a diamond-like or rhombic shape with dimensions of approximately 100 nm × 100 nm and a range in height from 3 to 17 nm (average height 6.8 nm, Figure 3. 2B). The angle between the long axes of these rhombic adsorbates is slightly less than 90° (78°–86°). In a replicate experiment (not shown), the scan angle was rotated by 45° in order to verify the rhombic particle shape was not an artifact of the AFM tip. Upon changing the scan angle, the pseudo-rhombohedra maintained their original orientation (with respect to stable surface features), which indicates that the observed shape reflects the morphology of the adsorbed particles. Some particles overlap with one another, which may indicate some epitaxial relationship between precipitates. No detectable particle growth was observed during the 35 min of polarization. There is also no apparent trend in particle distribution; the particles are distributed evenly on relatively flat regions of the magnetite surface.

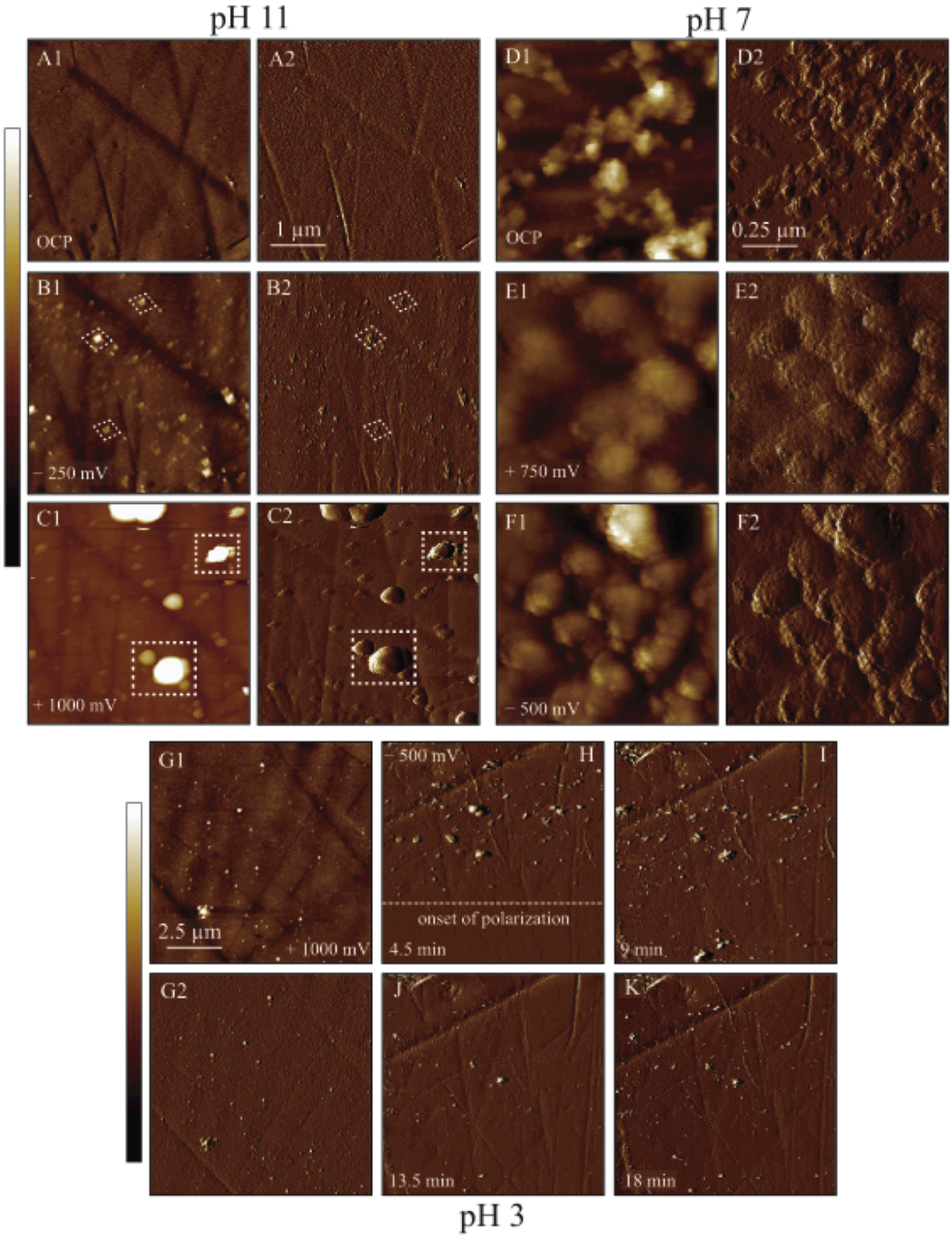

Figure 3. 2. EC-AFM height and Peak Force Error (PFE) images. A–C: pH 11, D–F: pH 7, G–K: pH 3. A. Color bar: ± 18 nm. Open circuit potential (OCP): height (A1), PFE (A2). B. Color bar: ± 18 nm. Polarization − 250 mV, 20 min: height (B1), PFE (B2). White outlines highlight rhombic growth features. C. Color bar: ± 50 nm. Polarization + 1000 mV, 13 min: height (C1), PFE (C2). White squares indicate new growth at this potential. D. Color bar: ± 50 nm. OCP: height (D1), PFE (D2). E. Color bar: ± 50 nm. Polarization + 750 mV, 21 min: height (E1), PFE (E2). F. Color bar: ± 50 nm. Polarization − 500 mV, 28 min: height (F1), PFE (F2). G. Color bar: ± 40 nm. Polarization + 1000 mV, 13.5 min: height (G1), PFE (G2). (H–K) Color bar: ± 40 nm. Polarization − 500 mV, PFE, 4.5 min (H), 9 min (I), 13.5 min (J), 18 min (K). White dashed line in (H) shows where polarization began.

After approximately 35 min of polarization at − 250 mV, where only rhombic sorbates were observed, the Eh was set to − 750 mV. At this potential, more rhombic features appear on the surface as well as a second class of larger, semi-spheroidal particles. These images are shown and described in further detail in Appendix 3.C, Figure 3.C 1. At this potential, the volume remains relatively constant around 6×10^7 nm^3.

In order to oxidize the sorbates deposited on the magnetite under reducing conditions, the magnetite was polarized at + 1000 mV for 30 min. Equilibrium thermodynamics does not predict a persistent solid phase over such a wide range of Eh conditions. Therefore, the dissolution/desorption of both the larger semi-spheroidal features and the pseudo-rhombohedra was expected. Both types of particles, however, largely remain on the surface. Furthermore, growth of additional spheres was observed (Figure 3.C 1). The total sorbate volume is the greatest at the more positive potentials (+ 250 mV and + 500 mV, Figure 3. 3). The number of particles counted on the surface decreases at + 250 mV, which indicates that there are fewer, larger particles on the surface, although the percentage of surface coverage remains largely the same after 45 min of polarization (between 1 and 7%). It is possible that both the pseudo-rhombohedra and the (oblate) spheroids are stable, or at least metastable on the timescale of the experiments, over a range of Eh values, and/or the dissolution kinetics is too slow to observe over the time of the experiment.

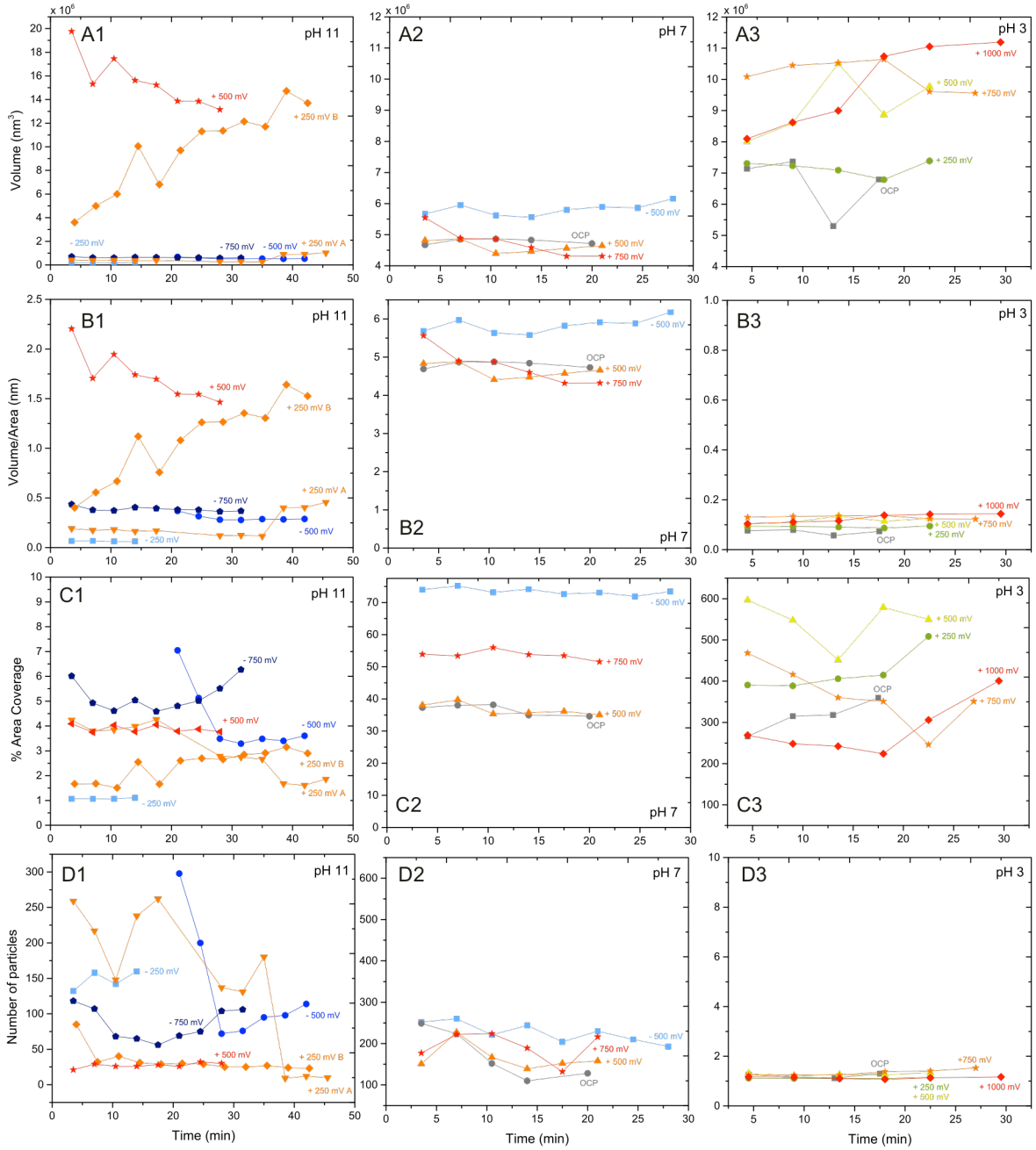

Figure 3. 3. Sorbate quantification from EC-AFM images at pH 3, 7, and 11. (A) Total sorbate volume. –250 mV A and − 250 mV B represent two different series of AFM images scanned over different areas of the surface. (B) Volume/sorbate area. (C) Percentage of surface coverage. (D) Number of sorbates plotted over time.

To determine if growth is primarily due to an increase in sorbate height or due to lateral growth, sorbate volume and surface area are compared for the images acquired at − 750 mV and + 500 mV (Figure 3. 4). The volume increases at a higher rate than the rate of growth for the surface area (scaled for clarity), which indicates that growth is mainly vertical in nature. At − 750 mV, the surface coverage remains constant over the duration of the experiment, so the entire volumetric increase may be attributed to vertical growth. The fact that it is more advantageous to grow on top of an existing sorbate indicates an increasing epitaxial mismatch for lateral growth; in other words, it is more energetically favorable to grow new layers on top, rather than making use of the additional bonding partners at a lateral step or kink site (Taylor et al., 2016). At + 500 mV, both the sorbate volume and area increase, which implies that the particles grow in the vertical and in the x- and y-directions (about 8% and 21% each, respectively). The square root of the surface area is also shown in order to compare equal dimensions; this length dimension remains unchanged at − 750 mV, yet it increases at a gentle slope at + 500 mV (21% increase). To summarize, growth at pH 11 at highly reducing conditions is primarily vertical, while highly oxidizing conditions result in both vertical and lateral sorbate growth. Sorbates that grow under oxidizing conditions are relatively large (~ 0.5–1 μm in diameter) and semi-spheroids compared with the rhombi that grow under more mildly reducing conditions. Under reducing conditions, the overall number of islands decreases slightly over time, which may be explained by diffusion and subsequent aggregation of particles on the surface complemented by fast vertical growth.

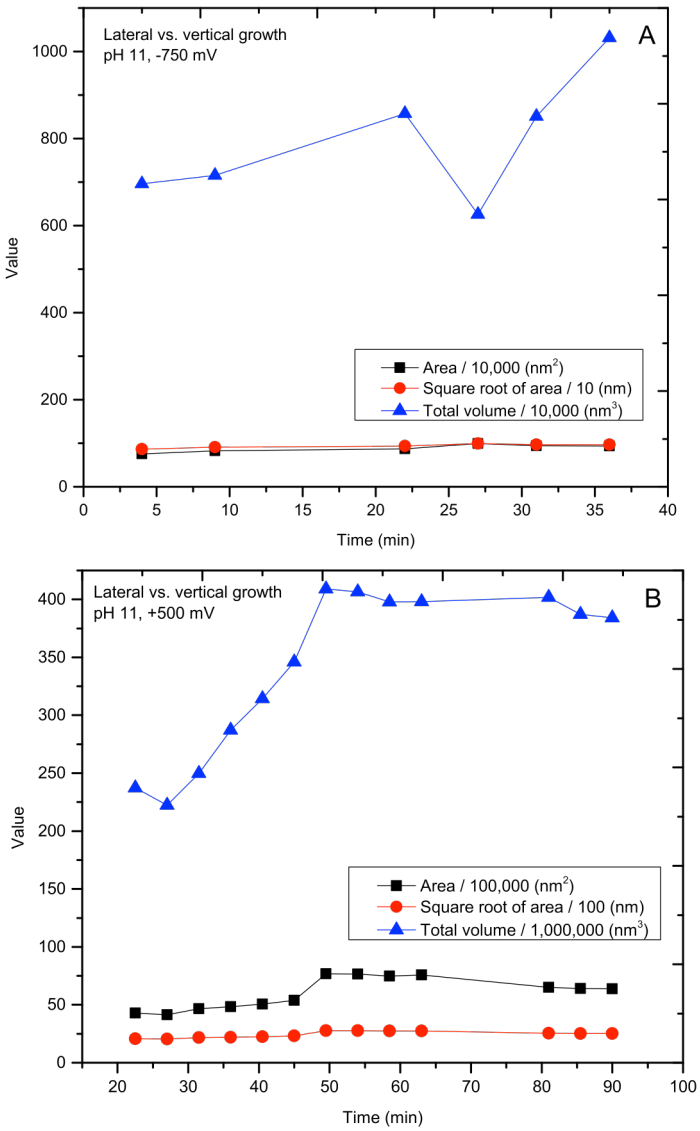

Figure 3. 4. A comparison of volumetric growth dimensions at pH 11, − 750 (A) and + 500 mV (B). The total volume and the total area covered by adsorbates (scaled for clarity) are plotted in dark blue and black, respectively. A more rapid increase in total volume versus area implies that growth on the surface is predominantly vertical at − 750 mV. Growth at + 500 mV is both lateral and vertical at approximately equal rates, given the 60% increase in total volume and 48% increase in area.

3.1.2. Redox processes at pH 7

As with pH 11, a series of AFM images was acquired as a function of time at the redox potentials 0 mV (open circuit potential), + 500 mV, + 750 mV, and − 500 mV in a solution at a pH of 7. At the beginning of the experiment, deposition is observed on the

magnetite surface (Figure 3. 2D). These conditions (redox- and pH-neutral) correspond to the Eh–pH region where chromite is the dominant Cr phase; aqueous Cr(VI) undergoes reductive precipitation in the presence of the magnetite surface and accumulates on the surface as chromite. The texture of the growth features may be described as subhedral; well-defined edges develop on many of the particles and define a roughly rhombic shape. In some cases, two sides form a fan-shaped feature rather than a four-sided rhombohedron. Individual particles, or growth islands, are approximately 75–100 nm in length, yet these features tend to form larger aggregates. After increasing the potential to + 500 mV, the general appearance of the surface remains largely unchanged, although results from image analyses indicate that there is a 9% drop in total particle volume in the first 10.5 min of polarization followed by a gradual increase from 4.4×10^6 to 4.6×10^6 nm^3 over the next 10 min (Figure 3. 3).

At + 750 mV, AFM images show significant rounding of the particles on the surface (Figure 3. 2E). The original rhombic shape of the precipitates is no longer observed, and the aggregates present at the open circuit potential have decomposed into broader and more gently sloping mounds on the surface. The percentage of the surface covered by growth features increases from approximately 37% at + 500 mV to 55% at + 750 mV; the volume, however, decreases by 23% after about 20 min of polarization. This trend may be explained by the dissolution of the particles on the surface. The cause of this "rounding" of particles is actually the creation of jagged edges through an increase in the number of kink sites. Kink sites are positions on the surface of a solid that have relatively few bonding partners and are consequently higher in energy. This higher energy state may exist during this experiment due to disequilibrium conditions caused by

the rapid changing of the redox potential; however, from an equilibrium energetics point of view, the creation of more energetic kink sites must be compensated by a gain in energy. One possible candidate for this energy gain may be the oxidation and solvation of Cr: $Cr(III) \Rightarrow Cr(VI)O_4^{2-}{}_{(aq)}$. For example, Cr(III) sorbed onto the surface is oxidized, and the energy gained through the hydration of Cr(VI) balances out the energy deficit caused by the creation of more kink sites.

The final potential in this series of experiments was − 500 mV. Polarization during 21 min at this potential resulted in an overall adsorbate volume increase of 9.4%. Most of this growth was observed on one side of the mound features produced at + 750 mV (Fig. 2F). These new growth features are primarily semi-spheroids approximately 30–50 nm in diameter. The percentage of surface coverage (~ 75%) is higher than that at the more positive potentials, yet does not increase over the duration of the experiment. These conditions plot within the Eh–pH region where $FeCr_2O_4$ is dominant (Fig. 1). These particles are smaller than those that first appear at the OCP. At − 500 mV, more Cr(III), as well as Fe(II), is available to form solid compounds.

3.1.3. Redox processes at pH 3

Volume growth observed during the OCP and at + 250 mV (up to 30 min) was minor in comparison to the growth seen at − 500 mV and at + 1000 mV (Figure 3. 3; Appendix 3.C, Figure 3.C 2). In this set of experiments, the potentiostat was set at − 500 mV during the acquisition of an image (rather than between images), and the results show that deposition occurred almost immediately upon polarization (indicated by the white dashed line in Figure 3. 2H). In this case, image acquisition is initiated at the OCP, and the polarization is applied part way through the acquisition of the image. This

change was made in order to capture growth at time steps shorter than the ~ 4.5 min per image. After this initial burst of growth, however, the total particle volume decreases before leveling out after 18 min. Larger, non-uniform semi-spheroidal particles are first observed on the surface, yet these larger features disappear after 13.5 min. Growth is relatively homogeneous over the entire scan area. Lateral vs. vertical growth analysis for images acquired at − 500 mV shows a decrease in the average length and average height in relatively equal proportions (Appendix 3.C Figure 3.C 2).

The positive potentials were also systematically explored at pH 3. The largest amount of volumetric increase occurs at + 1000 mV. A representative EC-AFM image is shown in Figure 3. 2G. The adsorbates appearing for all positive potentials are all semi-spheroidal and relatively small (50–100 nm in diameter, ~ 25 nm in height). A lateral vs. vertical growth analysis reveals that highly oxidizing conditions (+ 1000 mV) and low pH values produce fast lateral growth with a significant increase in growth islands (Appendix 3.C, Figure 3.C 3).

Under reducing conditions (i.e., more negative polarization potentials), $Cr(VI)_{aq}$ is heterogeneously reduced to the Cr(III) solids Cr_2O_3 or chromite, $FeCr_2O_4$. These phases are stable at pH values greater than 3.5. Indeed, sorption is observed at very reducing conditions for all three pH values (3, 7, and 11). In this case (i.e., at pH 3), the initial disequilibrium caused by changing the electrochemical potential may allow for the precipitation of Cr–Fe oxides at pH conditions that are considered to be unstable for these phases. It is also possible that the pH increased slightly during the reduction reaction to allow for oxide precipitation (Eq. 3.1a)

At both pH 3 and pH 11, adsorption/precipitation was the highest at very low and very high potentials. At pH 7, maximum growth occurs at − 500 mV, and dissolution is observed at + 750 mV. While we can rationalize the presence of solid Cr(III) phases as either Cr(− Fe) oxides or Cr(− Fe) (oxy)hydroxides under reducing conditions, the precipitation at very positive potentials for pH 3 and 11 is counterintuitive. The Eh–pH model would predict aqueous $HCrO_4^-{}_{(aq)}$ or CrO_4^{2-} as the dominant Cr phases, yet results from batch chemistry experiments (to be discussed in Section 3.2) show a significant decrease in dissolved Cr at pH 3 (and not at pH 11). We cannot rule out the possibility of $Cr(IV)O_2$, and another explanation is the precipitation of a ferric iron chromate, $Fe(III)_3(CrO_4)_2$. No solubility information was found for this compound; however, Ag_2CrO_4 and $PbCrO_4$ have very low solubilities ($K_{sp} \approx 10^{-12}$ and 10^{-13}, respectively). It is likely, therefore, that $Fe_3(CrO_4)_2$ is also highly insoluble. Although little thermodynamic/solubility information is available for $Fe_3(CrO_4)_2$, its low solubility may allow for precipitation with small amounts of Cr and Fe(III) in the system.

3.2. Batch chemistry analysis

Since the small area analyzed using EC-AFM may not be representative of Cr sorption over the entire working electrode surface, these observations were complemented by batch experiments. Changes in the concentration of Cr in solution were measured at 10-min intervals over the course of several EC-AFM experiments. At each time interval, the experiment was stopped, and the entire volume of solution was removed and analyzed using ICP-MS. The magnetite electrode was then re-polished before the next experiment. Given the solubility behavior of Cr (i.e., Cr(VI) compounds are often several orders of magnitude more soluble than Cr(III) compounds), we assume that any Cr removed from solution is Cr(III) that has precipitated or Cr(VI) that has

adsorbed onto the magnetite surface; the remaining Cr is present as an aqueous Cr(VI) oxyanion, such as $CrO_4^{2-}{}_{(aq)}$.

Results from pH 11 experiments indicate that very little Cr is removed from solution (Figure 3. 5). We would expect to see some Cr removal as either Cr_2O_3 or $FeCr_2O_4$ at the more negative potentials. As will be discussed in the next section, oxidation and subsequent passivation of the magnetite surface at pH 11 may explain the lack of Cr deposition. One point of concern for the analysis is the excursion above the initial Cr concentration of 2 μM at − 1000 mV and − 500 mV. The high error registered for these points likely arises from complications associated with the matrix pH adjustments required for measuring, which have an initial pH of 11. The small sample size of the EC cell prevented pH monitoring during and after the experiment. However, this variance does not invalidate the overall trend that relatively little Cr is removed from solution at pH 11.

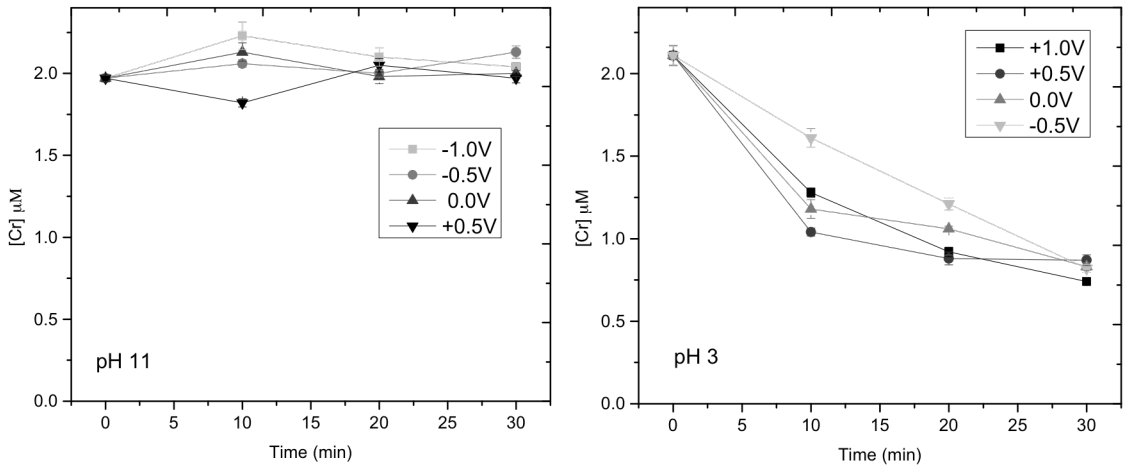

Figure 3. 5. Changes in total dissolved Cr concentration as a function of time and Eh at pH 3 and 11. Most of the Cr stays in solution at pH 11. However, at pH 3, Cr concentration decreases more at very high and very low potentials.

At pH 7, nearly all of the Cr was removed from solution across all potentials (results not shown). This is consistent with the relatively high percentage of surface coverage measured from the AFM images. Although the total sorbate volume calculated at pH 7 is not as high as the volume calculated at pH 3, more of the surface is covered with sorbates. Extrapolating this observation over the entire electrode surface (~ 15 mm^2 vs. 1 μm^2 for AFM images), it is feasible that all of the initial Cr(VI) in solution is reduced and precipitates as Cr(III) on the magnetite.

At pH 3, similar amounts of Cr removal from solution are observed at all potentials tested (~ 60% after 30 min). Maximum removal occurred at + 1000 mV, the most oxidizing potential (~ 65%), while the least Cr was removed at + 500 mV (~ 59%). At + 500 mV, approximately 50% of the Cr is removed, yet this rate of removal rapidly decreases and eventually levels out after 30 min of reaction. Cr removal at − 500 mV, however, is nearly linear over the entire 30-min period. EC-AFM experiments at this potential result in a rapid increase in initial growth followed by a decrease in the total particle volume before the volume levels out after ~ 15–18 min of scanning. This surge in growth occurred on a time scale shorter than the 10-min interval used for the batch chemistry experiments, and therefore would not be captured by the ICP-MS data. Image analyses are still consistent with a linear decrease in the concentration of Cr in solution over time.

An attempt was made to measure the possible release of Fe into solution (as an indication of magnetite dissolution), but any Fe in solution was below the detection limit of the spectrometer, which is on the order of 1 ppb (10^{-9} M). White and Peterson (1996) report magnetite dissolution rates ranging from 0.3 to 13 × 10^{-14} $mol \cdot cm^{-2} \cdot s^{-1}$ in

pH 1–7 anoxic solutions, and these rates decrease with increasing pH. Using these rates to estimate the amount of Fe(II) released into solution over 30 min of polarization, Fe concentrations should be high enough to be detected by instrument (i.e., 10^{-7} or 10^{-8} M). Dissolved O_2 present in the experimental solution may re-oxidize some of the Fe(II), so these estimates may be slightly high; however, the absence of measureable Fe in solution suggests that the sorbates present on the magnetite have a mixed Fe–Cr composition.

3.3. Spectroscopic analysis of the magnetite surface

3.3.1. X-ray photoelectron spectroscopy

XPS spectra were acquired in order to confirm Cr deposition through spatially-averaged spectroscopic evidence of Cr and to measure its oxidation state. This was done for a subset of the same magnetite samples that were previously used for EC-AFM experiments, polarized at − 750 mV, − 250 mV (pH 3 and pH 11), and + 1250 mV (pH 11 only). For the samples prepared at pH 3, binding energies (BE) for Cr $2p_{3/2}$ peaks (calibrated to C 1s at 284.8 eV) are consistent with Cr(III) (main peak components range from 575.4 to 577.4 eV) (Jung et al., 2007). The chemical shift between Cr(III) and Cr(VI) is relatively large, approximately 2.5 eV for single peak-fitted spectra (Suzuki et al., 1997; Kendelewicz et al., 1999; Kendelewicz et al., 2000), no peaks were observed at this higher binding energy, typically around 579 eV. This indicates that Cr(VI) reduction on the magnetite surface is complete.

Multiplet splitting, not to be confused with spin-orbit splitting, can also occur when an atom has unpaired valence electrons, such as Cr(III) (with the electronic configuration: [Ar] $3p^6$ $3d^3$, i.e., with three unpaired d electrons). Upon emission of a core-level electron, these unpaired valence electrons may couple with unpaired core electrons to create a number of final energy states. This results in a multi-peak envelope

rather than a sharp elemental line. In our initial fitting, we assume a single broad component to get a first approximation of the Cr 2p and O 1s peak positions (Figure 3. 6). In a more detailed fitting with at least two multiplet components for each peak, the Cr 2p binding energies for the magnetite polarized at the more reducing potential (− 750 mV, pH 3) are slightly lower than those of the magnetite polarized at − 250 mV. For clarity, the samples prepared at − 750 mV and − 250 mV will be referred to as sample A and sample B, respectively. For sample A (more reduced), positions of the main peak components are 575.4 and 576.8 eV, compared with 576.1 and 577.3 eV for sample B (less reduced). Additionally, the separation between $2p_{3/2}$ and $2p_{1/2}$ for sample A is more consistent with the peak separation reported for Cr_2O_3 and $FeCr_2O_4$ (9.45 eV reported by Ünveren et al. (2004) compared with 9.2 eV measured in this study). As predicted by geochemical modeling, we observe the formation of Cr and/or Fe–Cr oxide phases on the magnetite surface under very reducing conditions (− 750 mV). The Cr 2p spectra for Cr_2O_3 and $FeCr_2O_4$; however, are nearly identical (Biesinger et al., 2004; Beisinger et al., 2001; Jung et al., 2007), and due to the Fe 2p signal from the magnetite substrate, we were unable to distinguish between these two phases.

In comparison, the higher binding energies for chromium phases deposited on sample B (− 250 mV) may be indicative of chromium (oxy)hydroxides $Cr(OH)_3$, CrOOH, or perhaps an Fe–Cr solid solution, $(Fe,Cr)(OH)_3$. The binding energies for Cr(III) in $Cr(OH)_3$ are typically 0.5–0.6 eV higher than those for chromium oxides, and this shift increases with increasing number of OH groups (Harvey and Linton, 1981; McCafferty et al., 1988; Kendelewicz et al., 2000). While this higher binding energy is still contained within the Cr $2p_{3/2}$ envelope for sample B, increased Cr–OH content may

explain this shift towards the higher binding energy. Another way to evaluate the amount of hydroxylation is to compare O 1s peaks of experimental vs. unreacted magnetite (Figure 3. 7). The unreacted magnetite surface features an asymmetric O 1s peak with three main components. The largest component is attributed to lattice O atoms in the magnetite structure, while the other two components at higher binding energies are likely final state shake-ups (commonly observed in magnetite XPS spectra) and possible surface contamination (e.g., carbonation, non-stoichiometric O atoms or even some partial hydroxylation), respectively (Wandelt, 1982; Kendelewicz et al., 2000; Yamashita and Hayes, 2008). Two of the O 1s peak components for Cr_2O_3 and the polarized sample are very similar; however, there is an additional feature present in the reacted magnetite. This third component provides evidence of hydroxylation of the sample surface and the formation of Cr (and/or Cr–Fe) (oxy)hydroxide phases. At pH 6 and 8, Kendelewicz et al. (2000) report that this hydroxide layer contains little to no Fe. With the reduction of Cr(VI) to Cr(III), one would expect to see a corresponding increase in Fe(III) on the magnetite surface; however, both pH 3 spectra do not show a clear shift in Fe peaks or Fe(II)/Fe(III) ratios. This would imply that after 20 min of polarization, the surface is not yet saturated with reduced Cr precipitates, and some Fe(II) is still available to promote reduction.

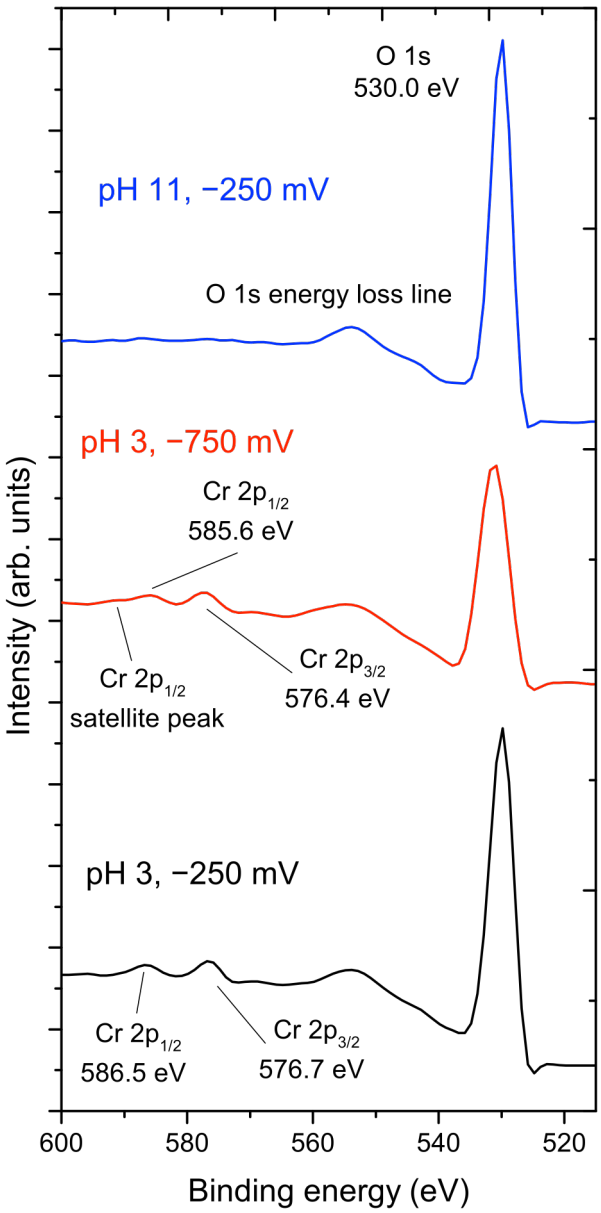

Figure 3. 6. XPS Cr 2p and O 1s spectra. Peak positions shown are the result of single peak fitting. The Cr 2p3/2 and 2p1/2 peaks are clearly visible in the spectra for samples prepared at pH 3; however, Cr 2p peaks do not appear in the pH 11 spectra. This implies that any Cr on the surface is below the detection limit of the instrument.

XPS spectra from samples prepared at pH 11 show no peaks for Cr in the narrow scan, which indicates that any Cr deposited on the surface is below the detection limit of the instrument (~ 1% or greater, Figure 3. 6). It is interesting to note that the Fe(II)/Fe(III) ratio of the pH 11 samples is generally lower than the expected ratio in magnetite (avg. ratio = 0.33, rather than the stoichiometrically expected value of 0.50). Spectra from the + 1250 and − 250 mV samples also show Fe 2p satellite peaks that are not present in magnetite, but are attributed to ferric Fe present in minerals such as hematite or maghemite. According to Peterson et al. (1997), this oxidized overlayer may be the formation of maghemite, which passivates the magnetite surface from further Cr reduction. In that particular study, passivation was observed at more neutral pH values, but may explain why Cr is not seen on the surface of the pH 11 samples in our experiments.

In summary, Cr deposited on the magnetite surface at pH 3 is entirely reduced Cr(III). Under very reducing conditions (− 750 mV), the Cr 2p peak positions and peak separation suggest that Cr oxides and/or Fe–Cr oxides (such as Cr_2O_3 or $FeCr_2O_4$) are present, while a shift towards a slightly higher binding energies and evidence of hydroxylation may denote Cr (oxy)hydroxide phases are more stable and deposited on the surface under less reducing conditions (− 250 mV). At pH 11, no Cr is observed due to partial oxidation and possible passivation of the surface by, e.g., maghemite, which would inhibit reduction or dramatically impede the kinetics of the reaction.

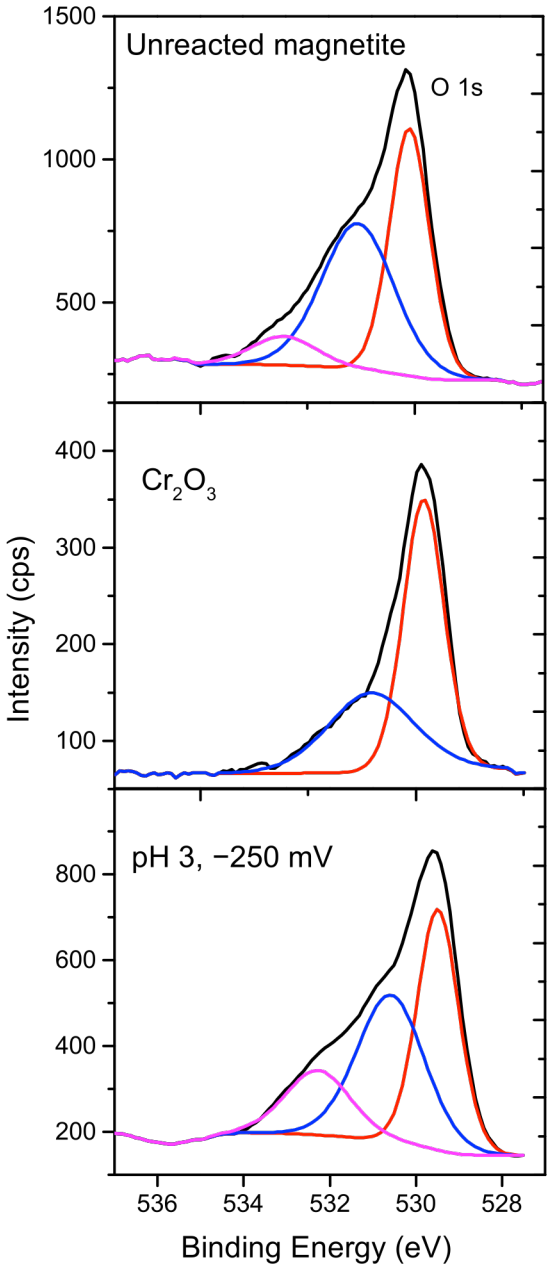

Figure 3. 7. Comparison of O 1s core spectra for unreacted magnetite, Cr2O3, and the magnetite sample polarized for 20 min at − 250 mV, pH 3.

3.3.2. Auger electron spectroscopy

In an effort to identify the phases observed to grow under oxidizing and reducing conditions, AES spectra were collected from samples at pH 3 (+ 1000 mV), pH 7 (− 500 mV), and pH 11 (+ 500 mV). While there is some indication that Cr_2O_3 is present at pH 3, + 1000 mV, this evidence is not conclusive. See Appendix 3.D for further detail.

4. Conclusions

In this study, electrochemical and atomic force microscopy methods are combined in order to image the deposition of Cr on the surface of magnetite at variable Eh and pH conditions. With this method, reactions that occur over the entire Eh–pH range can be observed in situ and complemented with further analysis of the surface and the solution. In this system, quantitative analysis of the AFM images reveals that more Cr precipitation occurs at very positive and very negative redox potentials at pH 3 and 11. At pH 7, maximum growth occurs at − 500 mV, while the total sorbate volume decreases over time at + 750 mV. At pH 3, the growth observed under oxidizing conditions is dominated by rapid lateral growth and the nucleation of new 2D growth islands, while growth at more reducing potentials (− 500 mV) occurs as a rapid initial deposition of larger particles that decreased in both height and diameter over the 30 min of polarization. At pH 11, vertical growth was the primary growth mechanism at both reducing and oxidizing conditions.

Concurrent batch chemistry experiments (and subsequent ICP-MS analysis) show total Cr removal from solution at all potentials at pH 7, about 60% removal of Cr from solution at all potentials at pH 3, and little Cr removal at pH 11. These observations are supported by results from XPS analyses of the magnetite surface. At pH 3, Cr(III) and/or Cr(III)–Fe(III) oxide phases are present at the surface for samples prepared under highly

reducing conditions (− 750 mV). At more moderately reducing potentials (e.g., – 250 mV), XPS analysis suggests the presence of Cr(III)–O–OH phases deposited on the surface. All Cr present on the magnetite appears to have reduced from Cr(VI) to Cr(III), although more definitive phase identification may require x-ray techniques with a higher degree of spatial resolution, such as synchrotron-based x-ray absorption spectroscopy (XAS). No Cr was detected on the surface at pH 11, although elevated Fe(II)/Fe(III) and Fe(III) satellite structures indicate that the magnetite surface at pH 11 is slightly oxidized, and this oxidized overlayer may inhibit Cr(VI) reduction. AES analysis, which is slightly more surface sensitive than XPS, supports the presence of some Cr on the surface at pH 11; however, interpretations drawn from these spectroscopic analyses suffered due to overlap between the O KLL peaks from the substrate and Cr LMM peaks. The deposition observed at positive potentials may be $Fe_3(CrO_4)_2$, yet more work is needed for confirmation. Angle-dependent XPS or high resolution XAS are possible techniques that would help determine Fe/Cr ratios as a function of depth.

Through the direct control of the oxidizing and reducing conditions as well as pH, EC-AFM in concert with chemical analysis of the solid and liquid, this method presents a new way to study the effects of Eh and pH on the reductive precipitation of Cr(VI). While Eh–pH diagrams may be a first indication of which phases dominate at certain conditions, we see significant sorption where the stability diagram does not predict a solid phase. For this system, the extension of thermodynamic databases to include less crystalline Cr hydroxide phases would provide a better description of sorption processes at a wide range of Eh conditions. With further improvements, this relatively underutilized

method may be a helpful tool to study the deposition and dissolution of redox-active metals on semi-conducting mineral surfaces in a broader geochemical context.

Appendix 3.A

3.A.1. Schematic of electrochemical AFM cell

Figure 3.A 1 presents a diagram of the electrochemical AFM cell used in these experiments.

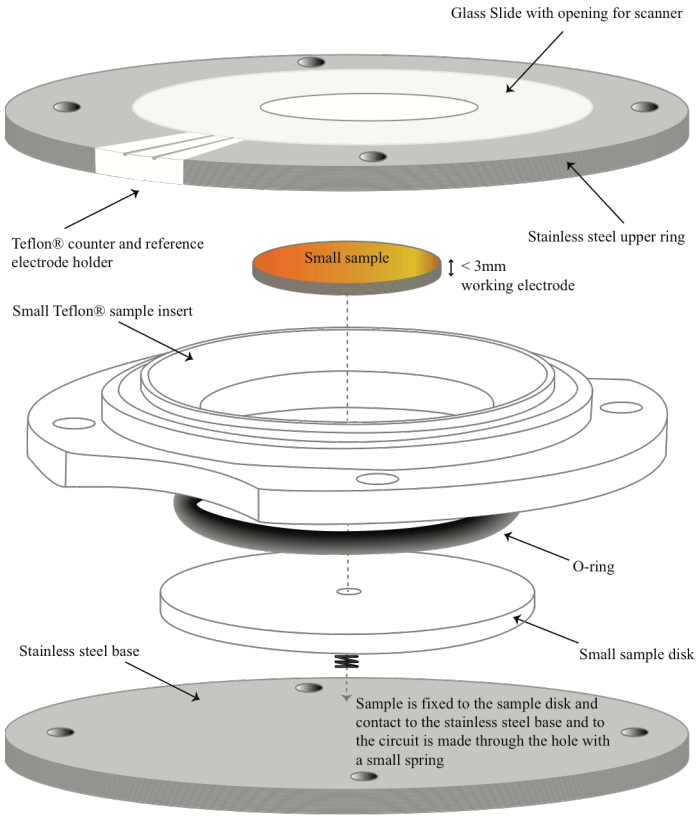

Figure 3.A 1. Schematic of electrochemical AFM cell.

Appendix 3.B

3.B.1. Detailed description of image analysis procedure

The raw data from each AFM image is exported as a 3-dimensional height matrix that preserves the topography of the surface as a function of the x and y location of the scanned area. Using the MATLAB script described in Section 0, a user-defined structural

element is chosen in order to identify features of interest on the surface and estimate the background, or the part of the image considered to be the magnetite substrate. This structural element is typically a circular disk that distinguishes surface elements; increasing the size of this disk allows for larger elements on the surface to be selected (and vice versa for a smaller disk), and the remainder is characterized as the background. These features are confirmed through visual selection, and the background is subtracted from the original grayscale image. With the background-subtracted image, the contrast is increased so that the selected features on the surface are easier to identify. Figure 3.B 1 presents each of these steps in detail, beginning with the original grayscale image (A), the original image minus the background (B), and the enhanced contrast image (with background subtracted) (C). At this step, the enhanced contrast images are converted to a black and white image by another user-defined threshold (D). Based on this black and white image, a binary array is created that indicates where sorbates are present (white) and where they are not (black). The number and size (volume and area) of the sorbates are calculated by combining this binary array with the image height information from the raw AFM data. Each image, normalized by the number of samples per line, represents one data point for each of the volume, area, size, and number of sorbate plots (Figure 3. 3). Figure 3.B 1 also shows a 3D model of the derived background (E), which highlights some of the surface defects and polishing grooves, which may influence the absolute values for the sorbate size and shape calculated with this method. For this reason, it is recommended that overall trends be emphasized more than absolute numbers.

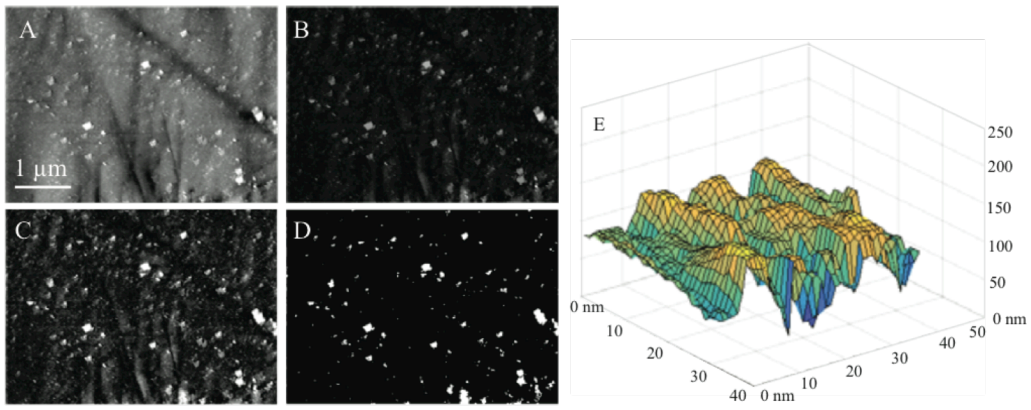

Figure 3.B 1. Detail of image analysis procedure for sorbate quantification. (A) Original grayscale image. (B) Original image minus script-generated background. (C) Enhanced contrast image. (D) Black and white binary image. (E) 3D background model.

Appendix 3.C

3.C.1. Extended description of redox processes at pH 11

In this section, further description, explanation, and interpretation of EC-AFM images at pH 11 and pH 3 are provided. During negative polarization at pH 11, two types of growth features appear on the magnetite surface: pseudo-rhombohedra and larger, spheroidal particles. Some of the rhombic particles appear to grow on top of and slightly adjacent to one another, such as those outlined in the panels labeled 9 and 22 min in Figure 3.C 1. This type of crystallographically directed growth may indicate epitaxial or parallel growth on the surface. Crystal intergrowths are about equal in size, and their offset is approximately one-half of the length of each feature (50–60 nm). Epitaxial relationships may limit the size of each rhombic sorbate, which would explain the occurrence of more sorbates at more negative potentials instead of continued growth of individual particles. The semi-spheroidal particles are significantly larger than the rhombic; their diameters range from 200 to 600 nm with a height on the order of 20 nm.

Over time (and particularly after 30 min), these semi-spheroidal particles diffuse towards each other to form a central particle with smaller pseudo-spheres on the periphery.

The semi-spheroidal particles are significantly larger than the rhombic; their diameters range from 200 to 600 nm with a height on the order of 20 nm. Over time (and particularly after 30 min), these semi-spheroidal particles diffuse towards each other to form a central particle with smaller pseudo-spheres on the periphery. This growth is shown in the lower panels of Figure 3.C 1. The pseudo-spherical sorbates appear to lack a crystallographic or structural relationship to the magnetite substrate, which suggests that they are mostly amorphous unlike the pseudo-rhombohedra. Since there is less of an epitaxial relationship between the semi-spheroidal particles and the magnetite surface, which would result in a crystallographic mismatch at a given size, growth of the semi-spheroidal sorbates is uninhibited. In addition, the fact that the semi-spheroidal features are more prone to surface diffusion indicates that they have a smaller (i.e., less negative) interface energy between the sphere–magnetite interface compared to the rhombohedron–magnetite interface. One candidate for such a phase is poorly crystalline chromium hydroxide (Rai et al., 1987; Rai et al., 1989).

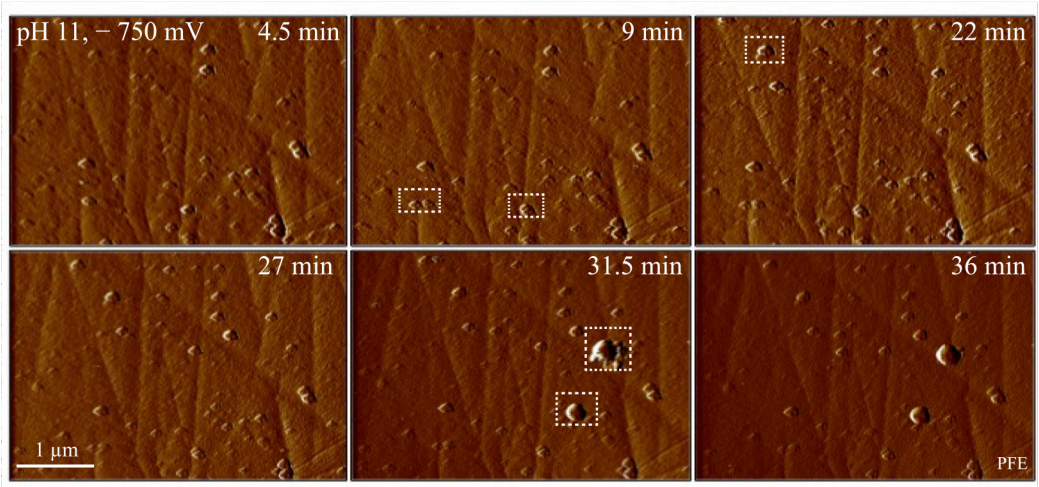

Figure 3.C 1. Particle growth during polarization of the magnetite electrode at − 750 mV as a function of time. Each image (which is peak force error data) was scanned in sequence. New growth features are marked by the white rectangles.

3.C.2. Extended description of redox processes at pH 3

Figures 3.C 2 and 3.C 3 provide lateral vs. vertical growth analyses for polarization at − 500 mV and + 1000 mV. After an initial burst of growth at − 500 mV, the total volume decreases, although the number of particles increases from ~ 70 to 180 (Figure 3.C 2). The average particle length and average height decrease at approximately the same rate. Such a rapid precipitation event may be due to the disequilibrium cause by the initial polarization at very reducing conditions followed by a slow return to a quasi-steady state. At + 1000 mV, there is an increase in volume of total adsorbate of ~ 30% within 30 minutes. This increase in volume is solely due to an increase in surface coverage, i.e. lateral growth, as shown by the overlap of the scaled volume and scaled area in Figure 3.C 3. Scaling the square root of the surface area shows that this length dimension slightly increases during the ~ 30 min of polarization and that the entire volume also increases for the experimental settings used. Such an increase in newly-formed adsorbates would normally be expected in a highly-supersaturated state that is,

according to classical crystal growth theory, dominated by two-dimensional nucleation (De Yoreo and Vekilov, 2003).

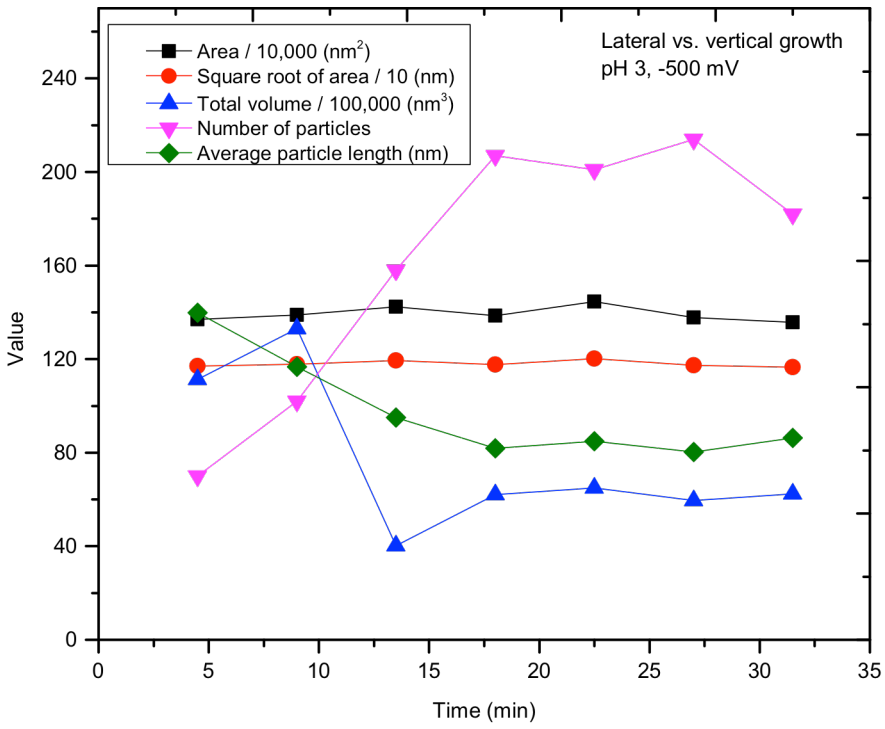

Figure 3.C 2. Lateral vs. vertical growth at pH 3, − 500 mV. The total volume decrease after ca. 35 min of reaction likely due to rapid initial precipitation followed by the dissolution of larger particles, shown here by decreasing average particle length (green line).

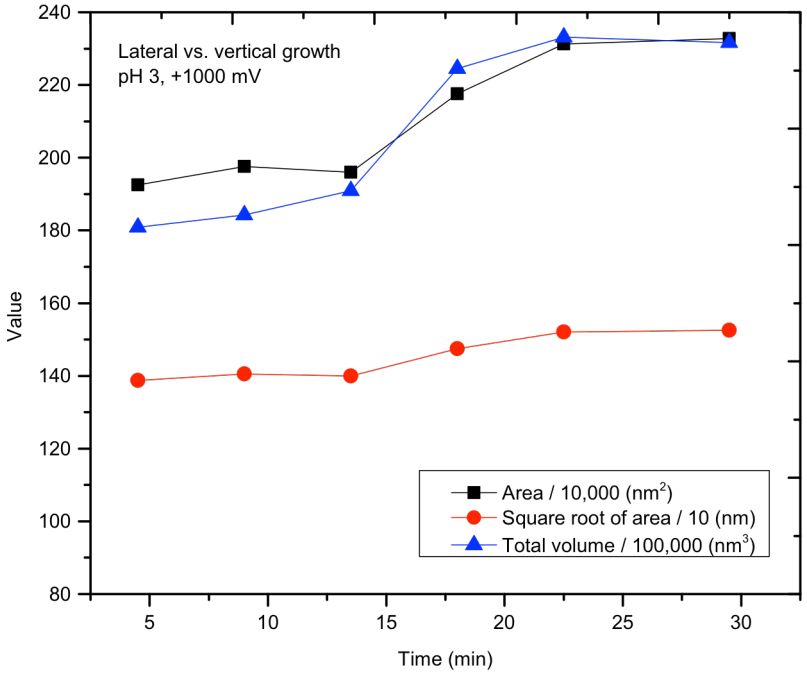

Figure 3.C 3. Lateral vs. vertical growth at pH 3, + 1000 mV. Growth at pH 3, + 1000 mV is primarily lateral, illustrated by the overlapping of the total volume and total area curves.

Appendix 3.D

3.D.1. Auger electron spectroscopy

At pH 3, Cr Auger peaks were observed for features resembling the particles imaged in the AFM (Figure 3.D 1). Cr has five Auger lines, although two of these have very low kinetic energies and are difficult to distinguish above the background. The most significant peaks occur at ~ 490, 530, and 560 eV, all of which are LMM transitions, yet we will focus on the 490 eV peak; the 530 eV line is almost entirely overwhelmed by the strong O KLL line, and the 560 eV peak is relatively weak in comparison. While it is common practice to differentiate AES spectra due to the broad shape of many Auger lines, here, we show the undifferentiated spectra in order to emphasize the contrast in shape for this set of peaks. The shapes of Auger peaks are potentially very sensitive to changes in chemistry and atomic arrangement of a given compound, especially if the Auger transition involves valence electrons. This particular energy range includes the Cr

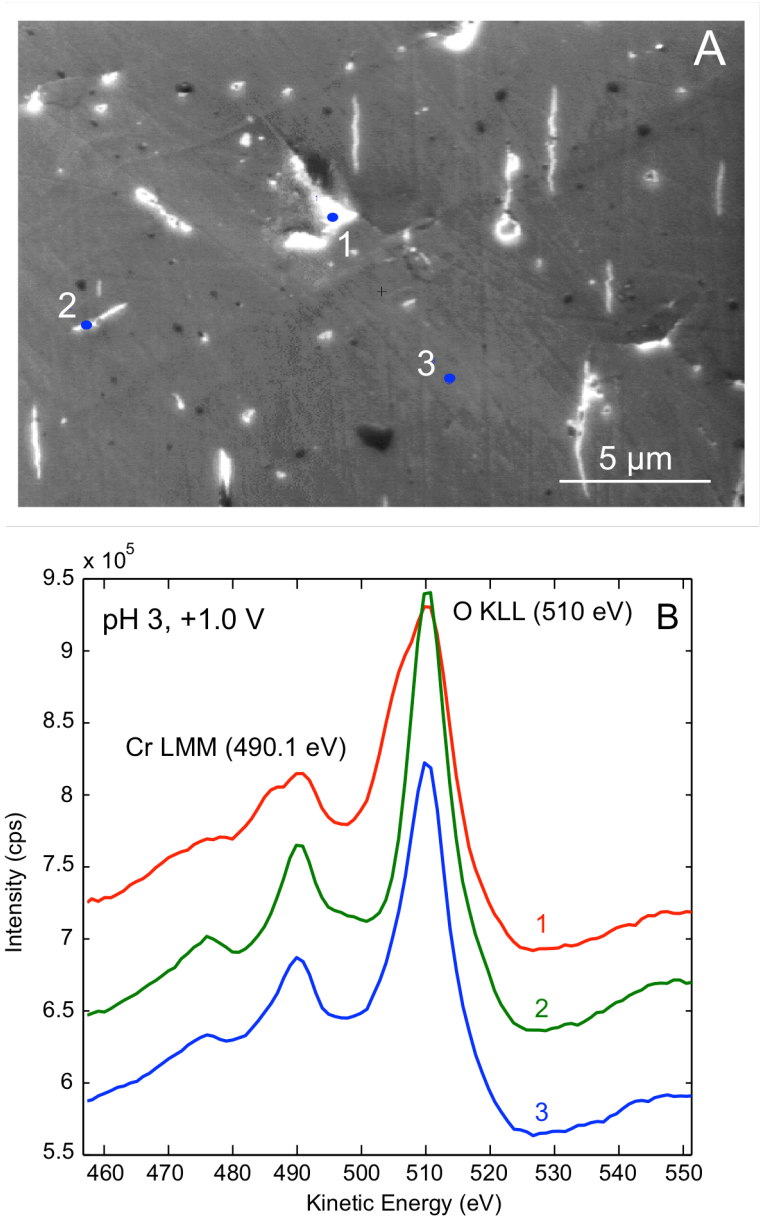

Figure 3.D 1. SEM image (A) and undifferentiated Auger spectra (B) collected from pH 3, + 1000 mV magnetite surface. Three analysis spots are labeled in the SEM image, and their corresponding spectra are shown from 450 to 550 eV. The first spot measured was focused on a particle ~ 1 µm in diameter, the second spot on a flat, white feature, and the third spot on the "background" magnetite. The spectrum for point 1 has asymmetric Cr LMM and O KLL lines, which could indicate that multiple Cr phases are present, including Cr_2O_3.

LMM peak at ~ 490 eV and the O KLL peak at ~ 510 eV, both of which involve two valence electrons for each transition. All three spectra closely resemble the spectrum for magnetite, including two relatively strong energy loss lines on the lower kinetic energy side of the O KLL peak at 510 eV. The overlap of the O KLL peak with the Cr LMM peak at 490 mV complicates the identification and interpretation of Cr peaks; however, the Cr LMM peak from the first analysis spot is asymmetric and has a distinct shoulder on the lower kinetic energy side of the peak. The O KLL peak for spot 1 is also asymmetric with a similar shoulder feature. The O KLL peaks were manually aligned at 510 eV in order to emphasize peak shape and to correct for surface charging; this shift was less than 1.7 eV. The presence of these shoulders can either indicate the presence of multiple bond types (e.g., the main O peak could be attributed to oxygen bonded to Fe or Cr, and the shoulder with a lower kinetic energy could be due to O bonded to H) or a different structural environment for that particular element. In an attempt to identify the chemical and oxidation state of Cr from the spectra collected from the magnetite surfaces, AES spectra were collected from three Cr reference compounds with Cr in three different oxidation states: Cr^0 (Cr metal), Cr^{3+} (eskolaite, Cr_2O_3), and Cr^{6+} (crocoite, $PbCrO_4$, Figure 3.D 2). Because Cr_2O_3 and $PbCrO_4$ are insulating minerals, the beam energy used to collect these spectra was 3 keV in order to reduce the amount of peak shift due to charging, which explains why the O KLL line is closer to 515 eV. Beam energy does not affect peak morphology. Assigning oxidation states with AES can be quite challenging due to a high background signature, the broad nature of Auger peaks, and the high potential for peak overlap from Auger transitions involving shallow atomic levels; however, we can say with some certainty that Cr^0 is not likely present on this magnetite

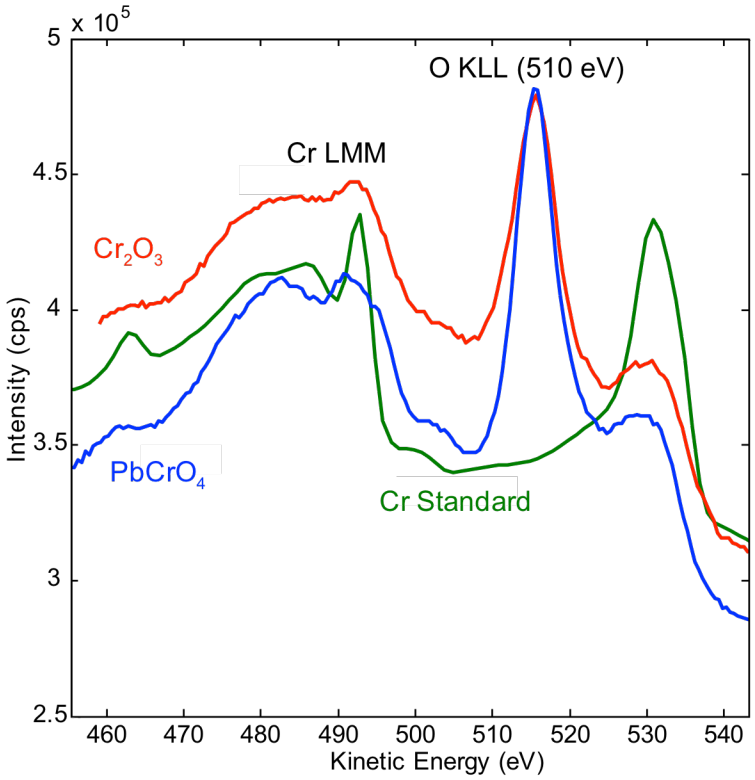

Figure 3.D 2. Overlay of Auger spectra between 450 and 550 eV for Cr in three oxidation states: Cr0 (Cr standard), Cr^{3+}(Cr_2O_3), and Cr^{6+} ($PbCrO_4$).

surface (pH 3, + 1000 mV). The shape of the Cr LMM 490 eV peak for Cr^0 is sharp and slightly shifted towards higher kinetic energies, which is not consistent with the Cr measured in the pH 3, + 1000 mV sample. On the other hand, Cr_2O_3 provides an Auger line that is most similar to the Cr LMM peak for the first spot analysis: a strong peak close to 490 eV and a shoulder on the lower kinetic energy side. This comparison provides some evidence that the particle analyzed contains Cr(III) as in Cr_2O_3 or $FeCr_2O_4$. Spots 2 and 3 are identical to the magnetite reference spectrum.

At pH 7, AES spectra of the magnetite surface were taken after 30 min of polarization at − 500 mV (SEM image of scan area and undifferentiated spectra shown in Figure 3.D 3). In the SEM image, a precipitate is shown in white (labeled ‘sorbate’) on top of the darker magnetite substrate. The sorbate material contains some amount of Ti

(that was dissolved, as an impurity, out of the magnetite substrate), evident by the Ti LMM transition labeled in the AES spectrum. At 498 eV, the energy loss feature produced from the O KLL transition in the magnetite has a distinct shoulder on the higher

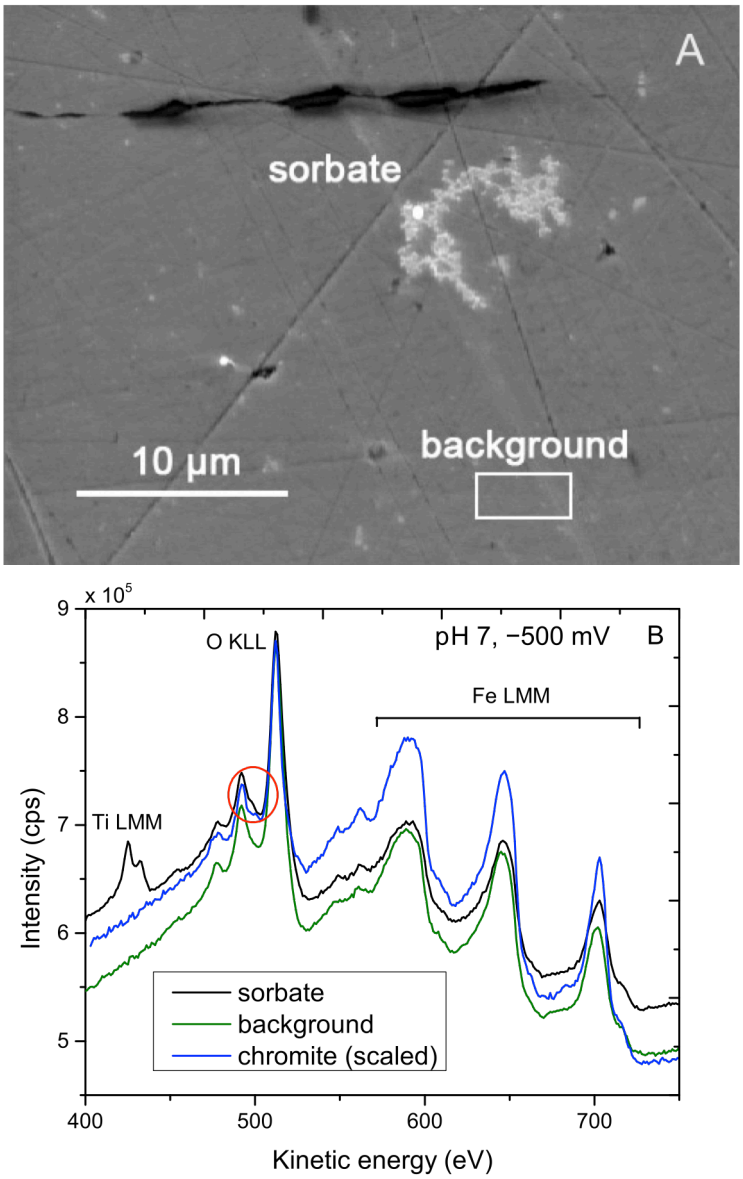

Figure 3.D 3. SEM image (A) and AES spectra (B) of pH 7 surface. The white sorbate material labeled in the SEM image contains Ti as well as Cr. The Cr LMM peak at ~ 490 eV creates a shoulder on the higher kinetic energy side of the O KLL energy loss feature from the magnetite substrate (highlighted in the red circle). A chromite AES spectrum (scaled for clarity) is also shown. Spectra are shifted to the background O KLL peak to account for peak shifts due to charging.

kinetic energy side of the peak. This shoulder is possibly produced by the overlap with the Cr LMM peak at ~ 490 eV. The AES reference spectrum for chromite is also presented in Figure 3.D 1; however, there is no clear indication that chromite contributes to the Cr shoulder feature.

AES spectra were also collected from the Cr-sorbed magnetite surface prepared at pH 11, + 500 mV. The presence of semi-spheroidal particles deposited homogeneously on the surface distinguishes this sample from the pH 3 and pH 7 samples (Figure 3.D 4). These particles are also present in AFM images acquired under similar oxidizing conditions. The AES spectrum for these particles does contain Cr LMM peaks around 490 eV (as a shoulder) and 530 eV (labeled with arrows in Figure 3.D 5). Unfortunately, these peak positions as well as their morphology are similar to the peaks in both Cr_2O_3 and $PbCrO_4$ reference spectra, and the Cr oxidation state cannot be confidently identified. At pH 11, the magnetite surface is positively charged, and less adsorption of CrO_4^{2-} would occur. If all the Cr in solution is present as Cr(VI), it is conceivable that these particles are an Fe(III) chromate phase, e.g., $Fe_2(CrO_4)_3 \cdot 3\ H_2O$ (Riou et al., 1978).

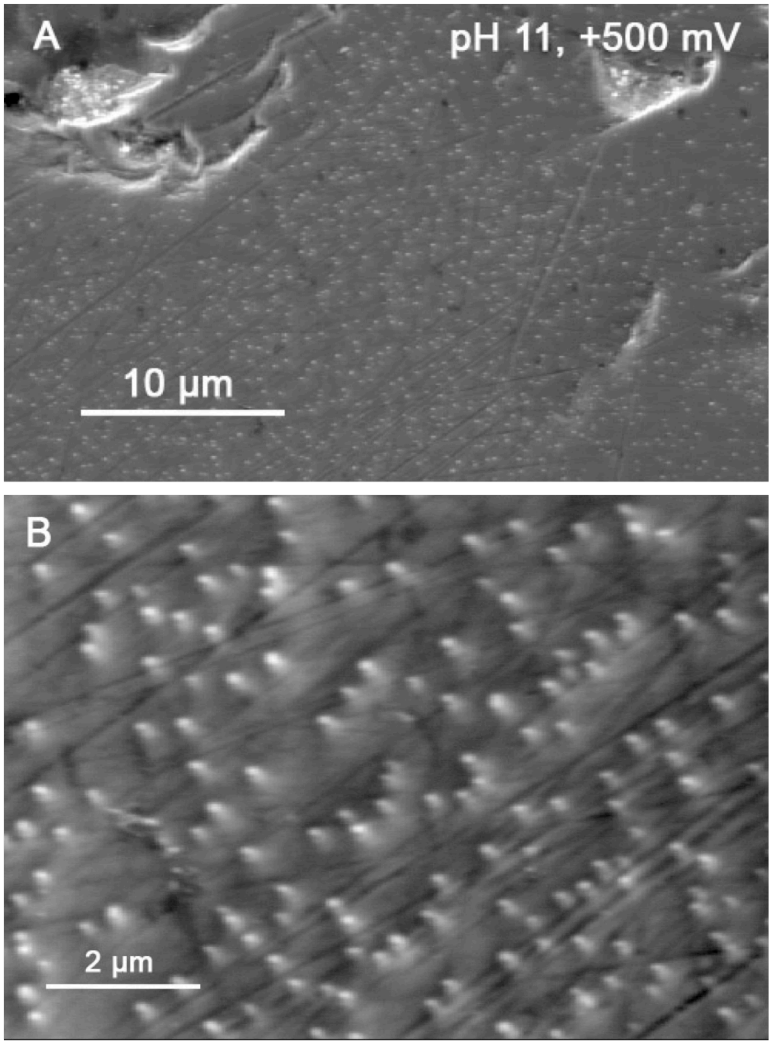

Figure 3.D 4. Secondary electron images of particles on the surface of magnetite deposited at pH 11, + 500 mV, taken using the Auger Nanoprobe. (A) Low resolution. (B) High resolution.

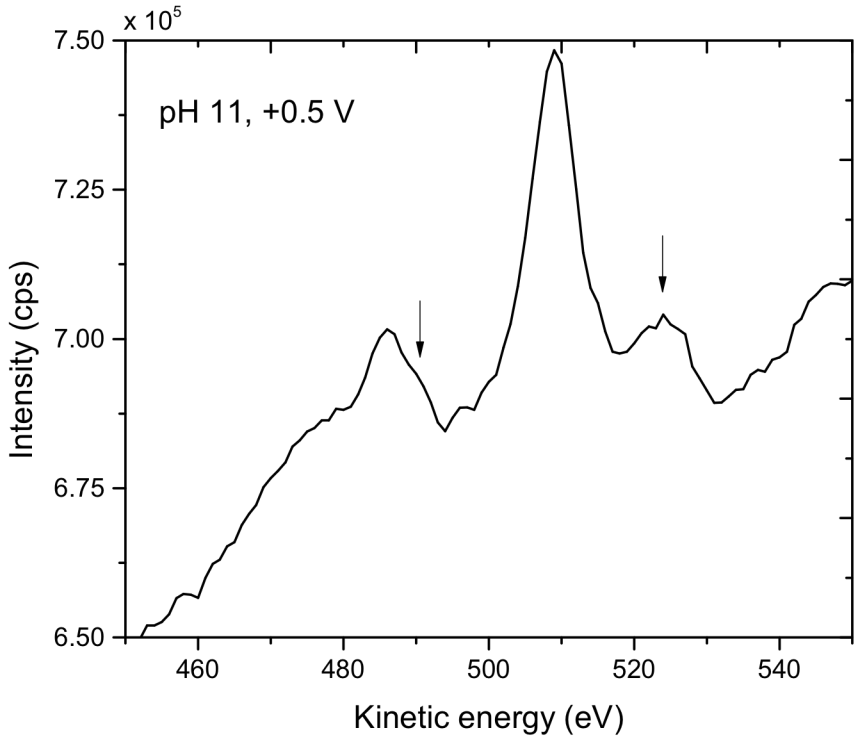

Figure 3.D 5. AES spectrum for pH 11, + 500 mV. Arrows indicate the presence of Cr peaks at ca. 490 and 530 eV, although the Cr oxidation state cannot be identified from this spectrum. It is possible that under oxidizing conditions, $Fe_2(CrO_4)_3$ $3(H_2O)$ can precipitate on the surface.

References

Baig S. A., Wang Q., Wang Z., Zhu J., Lou Z., Sheng T. and Xu X. (2014) Hexavalent chromium removal from solutions: surface efficacy and characterizations of three iron containing minerals. *CLEAN - Soil, Air, Water* **42**, 1409–1414.

Bartlett R. J. (1991) Chromium cycling in soils and water: links, gaps, and methods. *Environ. Health Perspect.* **92**, 17–24.

Becker U., Rosso K. M. and Hochella Jr M. F. (2001) The proximity effect on semiconducting mineral surfaces: a new aspect of mineral surface reactivity and surface complexation theory? *Geochim. Cosmochim. Acta* **65**, 2641–2649.

Biesinger M. C., Brown C., Mycroft J. R., Davidson R. D. and McIntyre N. S. (2004) X-ray photoelectron spectroscopy studies of chromium compounds. *Surf. Interface Anal.* **36**, 1550–1563.

Beisinger M. C., Payne B. P., Grosvenor A. P., Lau L. W., Gerson A. R., Smart R. S. C. (2001) Resolving surface chemical states in XPS analysis of first row transition metsl, oxides and hydroxides: Cr, Mn, Fe, Co and Ni. *Appl. Surf. Sci.* **257**, 2717-2730.

Buerge I. J. and Hug S. J. (1997) Kinetics and pH dependence of chromium(VI) reduction by iron(II). *Environ. Sci. Technol.* **31**, 1426–1432.

Cornell R. M. and Schwertmann U. (2006) *The iron oxides: structure, properties, reactions, occurrences and uses*., John Wiley & Sons.

Elsner M., Haderlein S. B., Kellerhals T., Luzi S., Zwank L., Angst W. and Schwarzenbach R. P. (2004) Mechanisms and products of surface-mediated reductive dehalogenation of carbon tetrachloride by Fe(II) on goethite. *Environ. Sci. Technol.* **38**, 2058–2066.

Etienne M., Schulte A., Mann S., Jordan G., Dietzel I. D. and Schuhmann W. (2004) Constant-distance mode scanning potentiometry. 1. Visualization of calcium carbonate dissolution in aqueous solution. *Anal. Chem.* **76**, 3682–3688.

Fendorf S., Wielinga B. W. and Hansel C. M. (2000) Chromium transformations in natural environments: the role of biological and abiological processes in chromium(VI) reduction. *Int. Geol. Rev.* **42**, 691–701.

Flury B., Frommer J., Eggenberger U., Mäder U., Nachtegaal M. and Kretzschmar R. (2009) Assessment of long-term performance and chromate reduction mechanisms in a field scale permeable reactive barrier. *Environ. Sci. Technol.* **43**, 6786–6792.

Gheju M. (2011) Hexavalent chromium reduction with zero-valent iron (ZVI) in aquatic systems. *Water, Air, Soil Pollut.* **222**, 103–148.

Harvey D. T. and Linton R. W. (1981) Chemical characterization of hydrous ferric oxides by X-ray photoelectron spectroscopy. *Anal. Chem.* **53**, 1684–1688.

Higgins S. R. and Hamers R. J. (1996) Chemical dissolution of the galena (001) surface observed using electrochemical scanning tunneling microscopy. *Geochim. Cosmochim. Acta* **60**, 3067–3073.

Higgins S. R. and Hamers R. J. (1995) Spatially-resolved electrochemistry of the lead sulfide (galena) (001) surface by electrochemical scanning-tunneling microscopy. *Surf. Sci.* **324**, 263–281.

Higgins S. R., Hamers R. J. and Banfield J. F. (1996) In-situ real-time imaging of the surface reactions of metal sulfide minerals with electrochemical STM. *Abstr. Pap. Am. Chem. Soc.* **211**, 70–COLL.

Hyland M. . and Bancroft G. . (1990) Palladium sorption and reduction on sulphide mineral surfaces: an XPS and AES study. *Geochim. Cosmochim. Acta* **54**, 117–130.

Jung Y., Choi J. and Lee W. (2007) Spectroscopic investigation of magnetite surface for the reduction of hexavalent chromium. *Chemosphere* **68**, 1968–1975.

Kendelewicz T., Liu P., Doyle C. S., Brown G. E., Nelson E. J. and Chambers S. A. (1999) X-ray absorption and photoemission study of the adsorption of aqueous Cr (VI) on single crystal hematite and magnetite surfaces. *Surf. Sci.* **424**, 219–231.

Kendelewicz T., Liu P., Doyle C. S. and Brown Jr G. E. (2000) Spectroscopic study of the reaction of aqueous Cr(VI) with Fe_3O_4 (111) surfaces. *Surf. Sci.* **469**, 144–163.

Kleber R. J. and Helz G. R. (1992) Indirect photoreduction of aqueous chromium (□). *Env. Sci Technol* **28**, 307–312.

McCafferty E., Bernett M. K. and Murday J. S. (1988) An XPS study of passive film formation on iron in chromate solutions. *Corros. Sci.* **28**, 559–576.

Otsu N. (1979) Threshold selection method from gray-level histograms. *Ieee Trans. Syst. Man Cybern.* **9**, 62–66.

Peterson M. L., Brown Jr G. E. and Parks G. A. (1996) Direct XAFS evidence for heterogeneous redox reaction at the aqueous chromium/magnetite interface. *Colloids Surfaces A Physicochem. Eng. Asp.* **107**, 77–88.

Peterson M. L., Brown Jr G. E., Parks G. A. and Stein C. L. (1997) Differential redox and sorption of Cr (III/VI) on natural silicate and oxide minerals: EXAFS and XANES results. *Geochim. Cosmochim. Acta* **61**, 3399–3412.

Rai D., Eary L. E. and Zachara J. M. (1989) Environmental chemistry of chromium. *Sci. Total Environ.* **86**, 15–23.

Rai D., Sass B. M. and Moore D. A. (1987) Chromium (III) hydrolysis constants and solubility of chromium (III) hydroxide. *Inorg. Chem.* **26**, 345–349.

Renock D. and Becker U. (2010) A first principles study of the oxidation energetics and kinetics of realgar. *Geochim. Cosmochim. Acta* **74**, 4266-4284.

Riou A., Bonnin E. and IUCr (1978) Structure cristalline de $Fe_2(CrO_4)_3(H_2O)_3$ alpha. *Acta Crystallogr. Sect. B Struct. Crystallogr. Cryst. Chem.* **34**, 706–709.

Rosso K. M. and Becker U. (2003) Proximity effects on semiconducting mineral surfaces II: Distance dependence of indirect interactions. *Geochim. Cosmochim. Acta* **67**, 941–953.

Sibanda H. M. and Young S. D. (1986) Competitive adsorption of humus acids and phosphate on goethite, gibbsite and two tropical soils. *J. Soil Sci.* **37**, 197–204.

Sokołowska M. and Bal W. (2005) Cu(II) complexation by “non-coordinating” N-2-hydroxyethylpiperazine-N′-2-ethanesulfonic acid (HEPES buffer). *J. Inorg. Biochem.* **99**, 1653–1660.

Stack A. G. (2008) GEOC 79-Applications of electrochemical scanning tunneling microscopy to adsorption and thin films in geochemical systems. *Abstr. Pap. Am. Chem. Soc.* **235**.

Stack A. G., Eggleston C. M. and Engelhard M. H. (2004) Reaction of hydroquinone with hematite I. Study of adsorption by electrochemical-scanning tunneling microscopy and X-ray photoelectron spectroscopy. *J. Colloid Interface Sci.* **274**, 433–441.

Stack A. G., Erni R., Browning N. D. and Casey W. H. (2004) Pyromorphite growth on lead-sulfide surfaces. *Environ. Sci. Technol.* **38**, 5529–5534.

Suzuki S., Oku M. and Waseda Y. (1997) Changes in the chemical state and composition of the clean surface of K_2CrO_4 and $K_2Cr_2O_7$ due to air exposure and argon ion bombardment. *Surf. Interface Anal.* **25**, 161–166.

Taylor S. D., Marcano M. C., Rosso K. M. and Becker U. (2015) An experimental and ab initio study on the abiotic reduction of uranyl by ferrous iron. *Geochim. Cosmochim. Acta* **156**, 154–172.

Taylor S. D., Powell B. A. and Becker U. (2016) Influence of the goethite (α-FeOOH) surface on the stability of distorted PuO2 and PuO2–x phases. *Radiochim. Acta* **104**, 821–841.

Tessis A. C., Penteado-Fava A., Pontes-Buarque M., De Amorim H. S., Bonapace J. A. P., de Souza-Barros F. and Vieyra A. (1999) Pyrite suspended in artificial sea water catalyzes hydrolysis of adsorbed ATP: enhancing effect of acetate. *Orig. Life Evol. Biosph.* **29**, 361–374.

Ünveren E., Kemnitz E., Hutton S., Lippitz A. and Unger W. E. S. (2004) Analysis of highly resolved x-ray photoelectron Cr 2p spectra obtained with a Cr_2O_3 powder sample prepared with adhesive tape. *Surf. Interface Anal.* **36**, 92–95.

Vorlicek T. P. and Helz G. R. (2002) Catalysis by mineral surfaces: implications for Mo geochemistry in anoxic environments. *Geochim. Cosmochim. Acta* **66**, 3679–3692.

Wandelt K. (1982) Photoemission studies of adsorbed oxygen and oxide layers. *Surf. Sci. Rep.* **2**, 1–121.

Welch K. D., Davis T. Z. and Aust S. D. (2002) Iron autoxidation and free radical generation: effects of buffers, ligands, and chelators. *Arch. Biochem. Biophys.* **397**, 360–369.

White A. F. and Peterson M. L. (1996) Reduction of aqueous transition metal species on the surfaces of Fe (II)-containing oxides. *Geochim. Cosmochim. Acta* **60**, 3799–3814.

WHO (2011) Guidelines for drinking water quality, 4th ed. *Geneva World Heath Organ.*

Wigginton N. S., Rosso K. M., Stack A. G. and Hochella M. F. (2009) Long-range electron transfer across cytochrome-hematite (alpha-Fe_2O_3) interfaces. *J. Phys. Chem. C* **113**, 2096–2103.

Yamashita T. and Hayes P. (2008) Analysis of XPS spectra of Fe^{2+} and Fe^{3+} ions in oxide materials. *Appl. Surf. Sci.* **254**, 2441–2449.

De Yoreo J. J. and Vekilov P. G. (2003) Principles of crystal nucleation and growth. *Rev. Mineral. geochemistry* **54**, 57–93.

Yuan K., Ilton E. S., Antonio M. R., Li Z. R., Cook P. J. and Becker U. (2015) Electrochemical and spectroscopic evidence on the one-electron reduction of U(VI) to U(V) on magnetite. *Environ. Sci. Technol.* **49**, 6206–6213.

CHAPTER 4
Understanding calcite wettability alteration through surface potential measurements and molecular simulations

Abstract

Mineral wettability and wettability alteration are important factors that determine the distribution and mobility of oil during the recovery process. Because wettability is dependent on many factors (*e.g.*, hydrocarbon composition, mineralogy, and pH), predicting mineral wettability is often difficult. Our goal is to look at changes that occur on the mineral itself, specifically changes in the surface structure and surface potential, in order to better understand the molecular-level processes involved in wettability alteration Nanoscale surface imaging is combined with Kelvin probe force microscopy (KPFM) to characterize changes in topography and surface potential for water-wet (hydrophilic) and oil-wet (hydrophobic) calcite surfaces, using the surfactant hexamethyldisilazane ($NHSi_2(CH_3)_6$, HMDS) to render the calcite surface oil-wet. KPFM measurements show that HMDS adsorbs preferentially on step edges of the calcite surface and is coupled by an increase in surface potential, which suggests a decrease in electron density in the valence band wherever HMDS is adsorbed. Surface-sensitive spectroscopic measurements (XPS) reveal that HMDS molecules on oil-wet calcite displace O atoms from H_2O molecules adsorbed to hydrated, water-wet calcite surfaces. Quantum-mechanical calculations of HMDS adsorption confirm an increase in the surface potential of oil-wet calcite and show that Ca corner sites are associated with the most favorable HMDS adsorption energies. Coadsorption of H^+ and OH^- with HMDS is more likely to

occur at edges and Ca kink sites and indicates that this surfactant may be an effective wettability modifier at a range of pH conditions. At these locations, the central amine (NH) group forms covalent π bonds with Ca atoms on the surface; additionally, one of the two HMDS methyl groups interacts with the surface while the other moves away towards the bulk solution to serve as an anchor point for other hydrophobic molecules and for the formation of oil microdroplets on the surface. This study is the first application of KPFM to mineral wettability, and with further development, KPFM can be a powerful tool to study interactions between specific functional groups and surface sites modifies the electronic structure of the mineral surface and produce changes in wettability.

1. Introduction

The physical and chemical properties of mineral surfaces play a significant role in the distribution and mobility of fluids in many different environments. In particular, in oil reservoirs, a rock's affinity to either water or oil, a characteristic referred to as wettability, is an important factor in oil production and enhanced oil recovery (Morrow, 1990). For example, wettability affects relative permeability, electrical properties probed in log measurements, and saturation profiles within the reservoir, which are parameters critical to reservoir characterization (Abdallah et al., 2007). Wettability is not always binary but rather a continuum between water-wet and oil-wet states, and this variation along with the possibility of several coexisting wettability types in a single reservoir can greatly complicate oil production and recovery scenarios. Yet, the ability to correctly identify wetting preference is relevant to optimal oil production and accurate reserves estimates.

Changes between water-wet and oil-wet states, which are brought about by hydrocarbon migration or by the use of synthetic surface-active compounds (surfactants), are not always predictable. Many factors are relevant to wettability preferences, including reservoir mineralogy, hydrocarbon composition, connate fluids or other formation fluids, temperature, and pressure. Wettability modifiers in the oil itself are often the polar components of resins and asphaltenes. Connate and production fluid chemistry, such as Ca^{2+}, Mg^{2+} and SO_4^{2-} concentrations and pH, have also been shown to influence wettability (Anderson, 1986a; Zhang et al., 2007). However, due to the molecular complexity of oil, it is unclear what specific chemical structures or functional groups are directly responsible for wettability changes in the rock or what steps are necessary to affect this change during original migration (oil displacing water) or during production (water displacing oil).

Traditionally, wettability experiments are based on empirical observations at the macroscopic scale. While these approaches have greatly increased the knowledge of fluid-surface interactions (Anderson, 1986a; Anderson, 1986b), an understanding that allows for prediction and the ability to precisely control reservoir wettability is still lacking. Because the mineral surfaces play a fundamental role in wettability alteration, in this study, we aim to assess and interpret changes at the molecular level on the mineral surface that result from changes in wettability. By simplifying a complex system through the use of a limited number of parameters, focusing on the initial water-wet and final oil-wet states only, and modeling the potential molecular interactions, we seek to develop a more fundamental understanding of wettability.

The goal of this study is to explore the effect of an induced change in wettability on specific physicochemical properties of the surface under the simplest conditions. In the reservoir environment, the reactive sites on the charged solid surface initially determine whether the fluid film that covers the surface becomes unstable, which allows wettability to vary (Abdallah et al., 2007). Consequently, we start by investigating changes in mineral surface potential as a major response to wettability alteration. We focus on the pure mineral calcite, which has a positive surface charge at neutral pH (the point of zero charge for calcite is pH 9.5, depending on dissolved Ca^{2+} and CO_3^{2-} species) (Stipp, 1999). Kelvin probe force microscopy (KPFM) and computational modeling are used to examine changes in the structure and the electronic state of the mineral surface as the result of wettability alteration. KPFM measures surface potential by applying a voltage that minimizes the electrostatic force between the tip and the sample. Through observation and modeling of the surface potential of a pure mineral before and after adsorption of a well-characterized surfactant, we seek to clarify what happens to the surface during wettability alteration and what organic functional groups are more likely to initiate changes in wettability during oil migration. This is important because, with this information, the compositional classification of hydrocarbons can potentially suffice to accurately estimate the original wettability state of a well-characterized rock reservoir.

Natural mineral surfaces commonly found in hydrocarbon reservoirs are water-wet before oil migration. Likewise, clean minerals in air are considered to be water-wet due to the adsorption of a thin film of water on the surface (Anderson, 1986b; Bohr et al., 2010). For this study, we chose to experiment with calcite, a common constituent of many oil reservoirs. Calcite also has a relatively simple and well-defined structure, which

is an advantage for constructing computational models and for interpreting any possible changes in the surface structure and charge redistribution with a change in the wetting preference of the surface. We reacted the water-wet surfaces with hexamethyldisilazane (HMDS), a common organosilazane compound in order to induce a change from a water-wet to an oil-wet state following the procedure described in Al-Anssari et al. (Al-Anssari et al., 2016). HMDS and several other silanes compounds have multiple applications in water repellency and have been used for many years in adhesion promotion (Plueddemann, 1982). Organosilazanes contain methyl or phenyl groups and at least one Si-N bond, which reacts with protons and/or hydroxyl groups on the mineral surface. As the compound reacts with the mineral surface, the methyl/phenol groups are exposed to the bulk fluid away from the surface, interact with non-polar oil constituents, and reduce the water-wetness of the surface (Osthoff and Kantor, 1957). HMDS is a well-known compound of definite chemical composition that is much simpler than an actual surfactant from oil or a commercial substance. Both experimental and computational applications are greatly simplified by these choices, while maintaining the relevance to more complex systems.

In the experimental part of this study, we use Kelvin probe force microscopy to measure the topography and to map the surface potential of water-wet and oil-wet calcite. This technique is a type of scanning-probe microscopy and has been used widely in the materials sciences to investigate surface potential distribution in metals, semiconductors, insulators, and biological and organic materials (Valdre, 2007; Mélin et al., 2010; Melitz et al., 2011). KPFM is based on electrical forces that are generated between the sample and the tip as the tip scans across the sample surface; these forces are modulated by an

applied AC+DC voltage, which causes the tip to oscillate at a certain frequency. During the scan, a feedback loop within the system adjusts the voltage applied to the tip in order to nullify these oscillations and reduce the electrical force between the sample and tip to zero (see Melin et al., 2010 for further detail). Under this condition, the bias voltage applied to the tip is equal to the local surface potential of the sample, which allows for high-resolution surface potential mapping. Although KPFM is a potentially powerful method to analyze the laterally-resolved electronic structure of surfaces, this technique is rarely used to analyze insulating mineral surfaces (Na et al., 2007; Liu et al., 2015; Moro et al., 2016); to our knowledge, this study is the first application of surface potential mapping to understand mechanism of wettability.

The surface potential of a mineral is the electrostatic potential energy of the surface relative to that of the bulk interior. The termination of a crystal results in a net charge at the surface due in part to surface atoms that are undercoordinated relative to their bulk counterparts, which results in dangling bonds. This net charge produces a surface potential that strongly influences the behavior of dissolved species in the surrounding fluid and the fluid itself. In the context of wettability, molecules that adsorb onto the sample and alter its wettability may substantially alter the surface potential. Depending on the amount of charge transfer that occurs between the surface and adsorbate (in this case, the surfactant), the surface potential may increase or decrease. Surface potential maps, such as those generated by KPFM, help visualize the charge distribution on the surface. For example, areas with a more positive surface potential have either a more positive charge contribution from cations and/or less electron density from anions. In general, electropositive adsorbates, which donate electron density to the

surface, cause a decrease in surface potential; electronegative adsorbates pull electrons away from the surface and cause an increase in surface potential. By measuring changes in the surface potential of oil-wet and water-wet states, we can learn about charge redistribution, the degree of charge transfer, and the relative stability of the parts of the fluid bonded with the surface. The distribution of charges at the mineral surface and the electronic interactions between surface atoms and adsorbates are key factors that determine which fluid is more likely to bond with the surface.

KPFM experiments allow us to measure the spatially resolved surface potential and infer changes in the surface charge distribution of the water-wet and oil-wet calcite surfaces at the nanometer scale; however, it requires a computational approach to develop an atomistic understanding of the nature of the bonds between the surface and the adsorbate (*i.e.*, determine if bonding is ionic or covalent with some partial transfer of electron density) and how well the HMDS molecule (and potentially other surfactants) sterically match with local charge groups on the surface. In order to achieve this level of understanding, we employ computational modeling to describe the molecular-scale processes involved in wettability alteration. Computational modeling results in much higher resolution of atomic arrangements and the thermodynamics of single molecules than is possible with experimental approaches. It is also the tool of choice to precisely describe the adsorption mechanism that occurs when a surface changes from water-wet to oil-wet. Specifically, both periodic and cluster models of calcite surfaces are used to identify surface sites that are more favorable to HMDS adsorption and to predict the likely adsorbate structure. Quantum-mechanical calculations are used to assess the degree of electron transfer and orbital overlap between the surface and adsorbate and to calculate

the work function before and after HMDS adsorption. The resulting changes in the surface dipole moments are also calculated.

2. Methods

2.1. Surface potential measurements

Several samples from a rhombohedral specimen of Iceland spar (transparent $CaCO_3$) were obtained by cleaving along the crystal's $\{10\bar{1}4\}$ face. The calcite sample from Brazil was kindly provided by the A.E. Seam Mineral Museum at Michigan Technological University. All samples had a 2 mm maximum thickness; areas vary from about 0.5 to about 1 cm^2. The organosilazane compound hexamethyldisilazane ($NHSi_2(CH_3)_6$, HMDS) was used to induce a change from a water-wet to an oil-wet state following the procedure described in Al-Anssari et al. (Al-Anssari et al., 2016). In their study, Al-Anssari et al. (Al-Anssari et al., 2016) compared the contact angles on calcite after treatment with HMDS to two more silanes. HMDS produced high contact angles on advancing and receding water droplets on the calcite surface submerged in an oil proxy (i.e., n-decane) and also in air, demonstrating its efficiency in turning the calcite surface oil-wet. Samples were rinsed with DI water and toluene immediately after cleaving and cleaned in air plasma for at least 1 hour. Half of the samples were fixed to a steel plug using silver paste and dried in nitrogen. The other half were submerged in HMDS and kept at 90 ºC for 24 hours in a tightly closed Teflon or glass beaker. Finally, the treated samples were washed with n-hexane and methanol in order to remove excess silazane and abundantly flushed with DI water before drying in N and mounting as described. Elevated temperatures were used for these experiments in order to accelerate the rate of chemical reaction and to assure a more complete oil-wet transformation.

Both clean and reacted samples were then analyzed in a Bruker Dimension Icon atomic force microscope (AFM) by amplitude modulated Kelvin probe force microscopy (AM-KPFM) using a new SCM-PIT tip (Bruker platinum-iridium coated silicon tip; nominal resonance frequency 75 kHz; spring constant 2.8 N/m) previously calibrated against highly-ordered pyrolytic graphite (HOPG). KPFM is an application of atomic force microscopy, in which the sample surface is probed with an atomically sharp tip using a piezoelectric scanner. The tip is mounted on a flexible, reflective cantilever, whose location is monitored through a laser aimed towards the back of the cantilever and reflected over a photodetector. As the scanner moves back and forth and across the sample, interactions between the tip and the sample surface cause the cantilever to bend. This displacement corresponds to a deflection of the laser beam on the photodetector and is interpreted as a change in the appropriate property, for example, topography, which is then represented as a color map image. The resolution of each image is either 256 or 512 samples per line, and the scan rate was between 0.5 and 1.0 Hz. NanoScope Analysis® software version 1.4 (Bruker Corporation) was used for image post-processing, including plane-fitting and flattening.

While there are numerous AFM studies on mineral surfaces, there are to date very few applications of KPFM to natural materials; therefore, a brief description of KPFM is provided here. In amplitude-modulated KPFM, the tip-sample configuration behaves like a small parallel plate capacitor such that the electrostatic force (F) between the tip and the sample as a function of the vertical distance (z) is

$$F(z) = -\frac{1}{2}\frac{\partial C}{\partial z}\left(V_{Applied} - V_S - V_Q\right)^2 \quad (4.1)$$

where C is the capacitance, $V_{Applied}$ is the potential applied to the KPFM tip, V_S is the surface potential, and V_Q is the effective surface potential when a charge Q is introduced into the tip-sample capacitor (Mélin et al., 2010). The term V_S is dependent both on surface states and on the tip-sample work function difference, which is known as the contact potential difference (V_{CPD}), $V_S \sim V_{CPD} = (\Phi_{tip} - \Phi_{sample}) / -e$. Together, the terms $V_S + V_Q$ comprise the local surface potential of the sample.

In an initial scan, the tip measures the topography of the surface (Figure 4. 1, step 1). The tip is then raised a few nanometers (Figure 4. 1, step 2), and the topographic profile is retraced (Figure 4. 1, step 3). This second, so-called interleave scan is to ensure that the tip-sample separation and, therefore, the capacitance remains constant. In order to modulate the electrostatic force between the tip and sample during the interleave scan, a potential is applied to the tip, which consists of both AC and DC voltage when the tip is oscillating at an angular frequency ω (when $\omega \sim 2\pi \times$ resonance frequency, f_o):

$$V_{Applied}(t) = V_{DC} + V_{AC}\sin(\omega t) \tag{4.2}$$

where V_{DC} is the DC component of the applied voltage, V_{AC} is the AC component of the applied voltage, and ω is the angular frequency of the oscillating tip. The V_{AC} contribution causes the electrostatic force to oscillate with the cantilever motion, and the V_{DC} contribution is then employed by the AFM's feedback mechanism to nullify (or reduce to zero) the electrostatic force. To clarify, by combining equations 1 and 2, the electrostatic force between the tip and sample at distance z is

$$F(z,t) = -\frac{1}{2}\frac{\partial C(z)}{\partial z}\left(V_{DC} + V_{AC}\sin(\omega t) - V_S - V_Q\right)^2 \tag{4.3}$$

Depending of the oscillation of the tip, this force may then be divided into three components, F_{DC} (which is static), $F_{1\omega}$, and $F_{2\omega}$ (both dynamic):

$$F_{DC}(z) = \frac{1}{2}\frac{\partial C}{\partial z}\left(V_{DC}^2 - \frac{V_{DC}^2}{2}\right) \tag{4.4a}$$

$$F_{1\omega}(z) = \frac{\partial C}{\partial z}(V_{DC} - V_S) \cdot V_{AC}\cos(\omega t) - \frac{\partial C}{\partial z}V_Q \cdot V_{AC}\cos(\omega t) \tag{4.4b}$$

$$F_{2\omega}(z) = \frac{1}{4}\frac{\partial C}{\partial z}(V_{AC}^2 \cdot \cos(2\omega t)) \tag{4.4c}$$

Briefly, Equation (4.4a) describes the force that causes static deflection of the cantilever, Eqn. (4.4b) is the force used to determine V_{DC}, and Eqn. (4.4c) is the force used to measure capacitive effects in other KPFM applications (Mélin et al., 2010). Because the tip is oscillating at an angular frequency $\omega \sim 2\pi f_o$ (where f_o is the resonance frequency of the tip), only the $F_{1\omega}$ force component results in the amplification of the tip oscillation, while the F_{DC} and $F_{2\omega}$ force components are no longer in resonance and are therefore reduced. The feedback loop then applies V_{DC} so that $F_{1\omega}$ goes to zero and $V_{DC} = V_S + V_Q$. Under this condition, KPFM nullifies the electrostatic force between the tip and the sample and results in the spatially resolved local surface potential of the sample.

The lateral spatial resolution of AM-KPFM is typically 25 nm, although sub-nanometer resolution is possible depending on the sample (Melitz et al., 2011). It is possible to improve the spatial resolution by monitoring the electric force gradient instead of the force itself in the feedback loop, and this is the mechanism used in frequency modulated KPFM (FM-KPFM). On the other hand, AM-KPFM has a higher energy resolution (5 meV) when compared with FM-KPFM (10-20 meV).

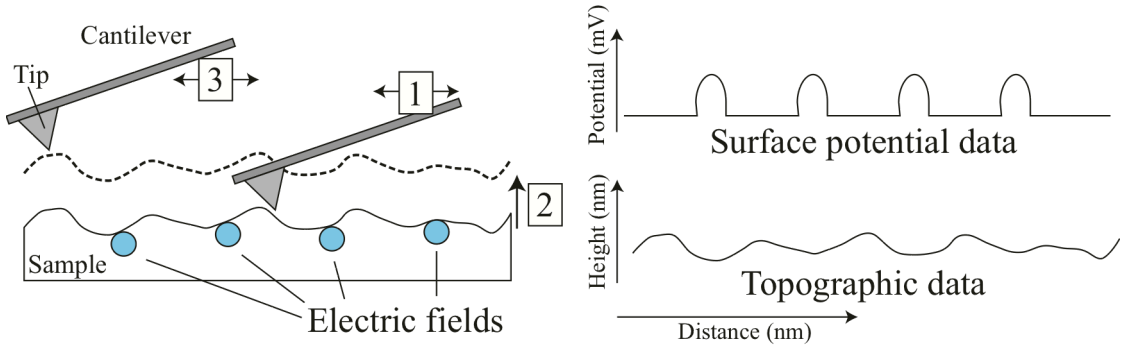

Figure 4. 1. Schematic of Kelvin probe force microscopy configuration. (1) Tip measures topography of sample surface in initial scan. (2) Scanner raises the tip above the sample surface, and (3) the surface is scanned a second time while measuring the potential difference between the sample and tip and maintaining a constant distance between the tip and the sample.

2.2. X-ray photoelectron spectroscopy (XPS)

Changes in the composition of surface atoms before and after treatment with HMDS were determined using x-ray photoelectron spectroscopy. Shifts in electron binding energies were measured using a Kratos Axis Ultra XPS with an Al Kα x-ray radiation source (1486.6 eV). Samples were degassed overnight under a vacuum pressure of $<10^{-5}$ Torr, and analyzed at a pressure of $<10^{-8}$ Torr. The x-ray emission current and anode voltage used during spectra acquisition were 8 mA and 14 keV, respectively. Charge neutralization was constantly applied due to the weak conductivity of the samples. Spectra were acquired using a hybrid lens and slot aperture (700 × 300 Å). Survey scans were collected in the BE range –5 to 1200 eV at 4 sweeps (dwell time = 100 ms) and at a pass energy of 160 eV. Narrow scans of C, N, O, and Si were collected for all calcite samples under the same analyzer conditions, 20 eV pass energies, 240 ms dwell time, and 10 to 20 sweeps to better resolve photopeak energy differences between clean and reacted calcites.

2.3. Computational modeling

Total energy calculations and geometry optimizations were performed on periodic and cluster models using the software package Dmol[3] (Local Density Functional

Calculations on Molecules) (Delley, 1990). The GGA-PBE exchange-correlation potential was used (Perdew et al., 1996), and core electrons were treated with effective core potentials. Double Numerical plus *d*-functions (DND) were used to describe atomic orbitals. COSMO (COnductor-like Screening MOdel) was used to consider the effect of hydration (Klamt and Schuurmann, 1993). For periodic calculations, the reaction energies of HMDS adsorption to flat terraces and straight edges (both polar and non-polar) were calculated with and without COSMO. A cluster model was employed in conjunction to analyze HMDS adsorption on additional calcite surface sites, including acute and obtuse monoatomic step edges, cation and anion kink sites, and cation and anionic corner sites. To create the cluster, a 2×2 unit cell slab was cleaved on the $\{10\bar{1}4\}$ surface from an optimized bulk calcite crystal. From the top layer of the slab, Ca-CO_3 groups were selectively removed so that a 4 molecule × 4 molecule island remained in the center of the slab. The result was a $Ca_{72}(CO_3)_{72}$ calcite cluster, which has 4×4 small island and 8×8 two layer underneath the island (360 atoms). The geometry of the calcite substrate was fixed. In order to allow for electrons to distribute themselves to the correct orbitals rather than be trapped in the wrong ones after the initial guess, thermal smearing was used with a smearing parameter of 0.005 Ha (0.14 eV which is equivalent to an electronic kinetic temperature of about 1500 K). Since density functional calculations do not accurately describe van der Waals interactions (vdW) that arise due to fluctuations in charge density between adjacent atoms, van der Waals dispersion corrections were applied (Tkatchenko and Scheffler, 2009). With this correction, an additional term with adjustable parameters is fitted to the vdW radius and charge density is included in the functional to account for dispersion energy.

In order to interpret the surface potential determined by KPFM experiments, the surface potential of the calcite model was calculated before and after adsorption of HMDS; however, instead of evaluating the potential difference between the surface and a conducting tip, we compute the work function (WF) of the surface, which is defined as the difference between the electrochemical potential of the electrons in the surface atoms (μ or the Fermi level E_F) and the electrostatic potential of a point in vacuum immediately outside of the surface (V_{vacuum}): $\Phi = -eV_{vacuum} - E_F$. Work function is a fundamental electronic property of a surface, and is a measure of the energy required to remove an electron with zero atomic binding energy (i.e., at the Fermi level) away from the sample. It can also be interpreted as stability or removal resistance of an electron in a surface atom/molecule (Kahn, 2016). The WF of a material can be conceptualized as the result of two indivisible components: the first is the electrochemical potential from surface electrons and the second is the surface dipole, which is the result of the redistribution of charges at the surface. The relative change in WF before and after a change in wettability may provide insight into the stability of the adsorbate and the movement of electrons on the surface. To calculate WF, the calcite $\{10\bar{1}4\}$ surface is modeled as a slab (~12 Å in thickness), and a vacuum gap separating a periodic array of slabs to preserve three-dimensional periodic boundary conditions. While typically, such vacuum gaps are 10-15 Å thick, here the vacuum layer is approximately 40 Å thick to ensure that electrostatic interactions between two neighboring slabs are negligible and that there is enough space to do the WF evaluation. The electrostatic potential is then calculated and averaged in planes parallel to the surface. With this method, the WF is evaluated as the difference

between the Fermi energy and the electrostatic potential of the vacuum away from the surface.

3. Experimental results

3.1. Calcite surface potential measurements

In order to compare surface structures and the surface potential distribution between water-wet and oil-wet calcite, KPFM experiments were first performed on freshly-cleaved calcite in air. As previously mentioned, because minerals at ambient

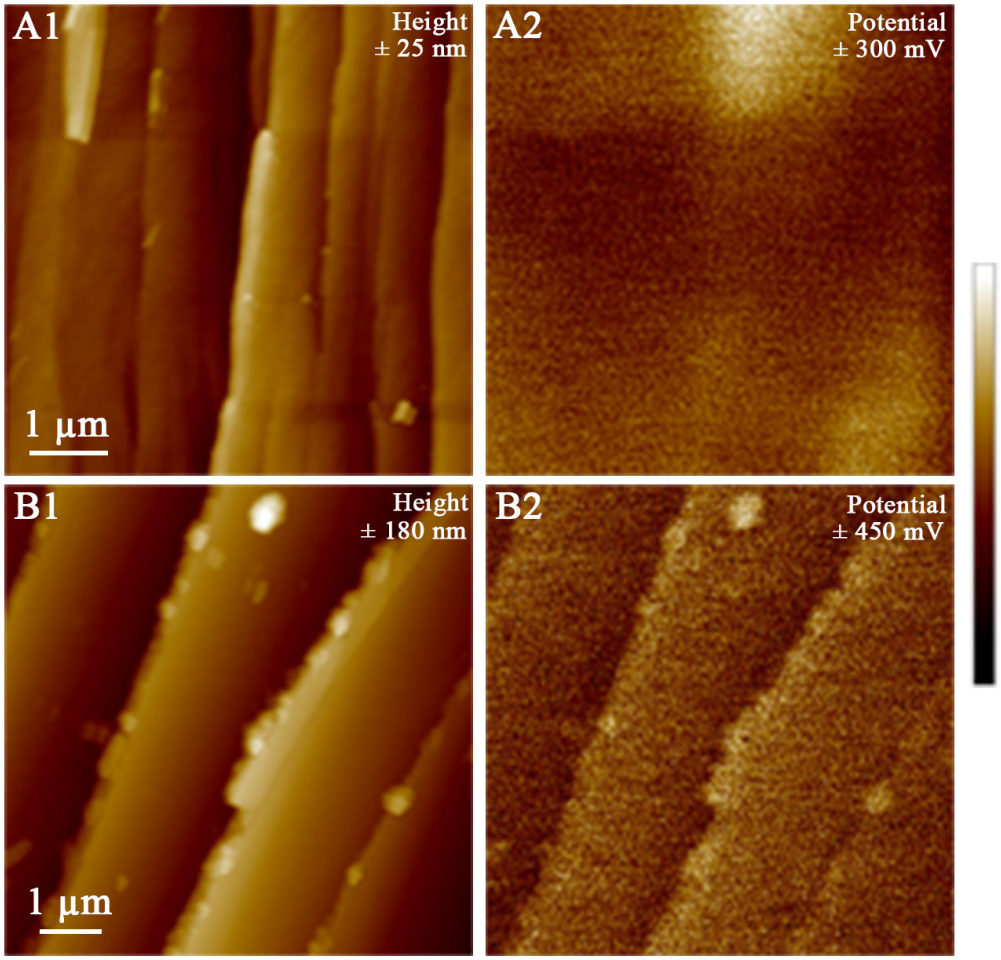

Figure 4. 2. Height and surface potential maps of calcite before (A1 and A2) and after treatment with HMDS (B1 and B2). Before reaction with HMDS, surface potential shows no correlation to the sample's relief.

temperature and pressure have a thin film of water adsorbed to their surfaces, this initial step allows us to characterize the topography and the surface potential of water-wet calcite surface. (Surface potential measurements cannot be performed in aqueous fluids.) Water-wet calcite shows well-developed terraces approximately 2-10 nm tall and spaced between 100 and 800 nm apart. These steps were likely created during cleaving. The surface potential of the water-wet sample shows very minor correlation with the edges of its terraces and is only apparent for terraces larger than 10 nm in height (Figure 4. 2A). This initial scan also enabled us to test the efficiency of the plasma cleaning procedure. In a few cases, the surface was contaminated with irregular, nanometer-sized mounds during the cleaning processes. These particular samples were not used.

Calcite samples reacted with HMDS, which we will refer to as treated samples (*vs.* the untreated, water-wet samples), were also analyzed with KPFM. On the treated samples, hemispherical features tens to hundreds of nanometers in height are present over the entire area of the sample and are particularly concentrated on step edges of the terraces (Figure 4. 2B, Figure 4. 3). Because the reaction with HMDS was the only difference in the preparation of the untreated and the treated samples, we interpret these features on the treated calcite surfaces as HMDS adsorbates. Al-Anssari et al. (Al-Anssari et al., 2016) have previously demonstrated through contact angle experiments that HMDS adsorption on calcite changes the wetting preference from water-wet to oil-wet; therefore, the presence of discrete adsorbate patches is a characteristic of oil-wet calcite surfaces under these conditions. Treatment with HMDS also changes the magnitude and distribution of the electrostatic potential on the calcite surface (Figure 4. 2B). HMDS adsorbates appear as bright spots on the surface potential image, which indicates that

surface potential is higher in the areas where HMDS is adsorbed relative to the calcite substrate (Figure 4. 2B); because KPFM corrects for difference in height between surface features, the surface potential image would appear as one color if there were no differences in potential. This was the case on a large proportion of the treated calcite samples analyzed according to statistical analyses, which are discussed in more detail later in this section. Additional height and potential images of both water-wet and oil-wet calcite are shown in the Supporting Information.

Figure 4. 3 presents another example of a treated calcite sample. In this particular experiment, HMDS was diluted to 0.1 mM and reacted with a freshly-cleaved calcite surface. This image of the calcite surface was taken *in situ*, *i.e.*, in the HMDS fluid. HMDS adsorbates approximately tens of nanometers in height form a well-defined rim along a step feature. HMDS adsorbates are also present on two sides of the etch pits on either side of the step.

HMDS adsorption and an increase in surface potential also occurred on flat portions of the calcite sample (*i.e.*, areas not associated with terraces, Figure 4. 4). These particular adsorbate patches are 0.5-1 μm in diameter and on the order of 5 nm in height. While it is likely that the terrace edges serve as more favorable adsorption sites for HMDS under certain conditions (discussed further with computational modeling), these images illustrate that adsorption can still occur in the absence of surface relief and that an edge is not necessary for HMDS to adsorb onto the surface. Another possibility is that the "flat" regions of the surface may have steps, kinks, or other surface features that are not resolved at this resolution. These smaller scale irregularities in the surface might serve as nucleation sites for HMDS micro-droplets form on the surface.

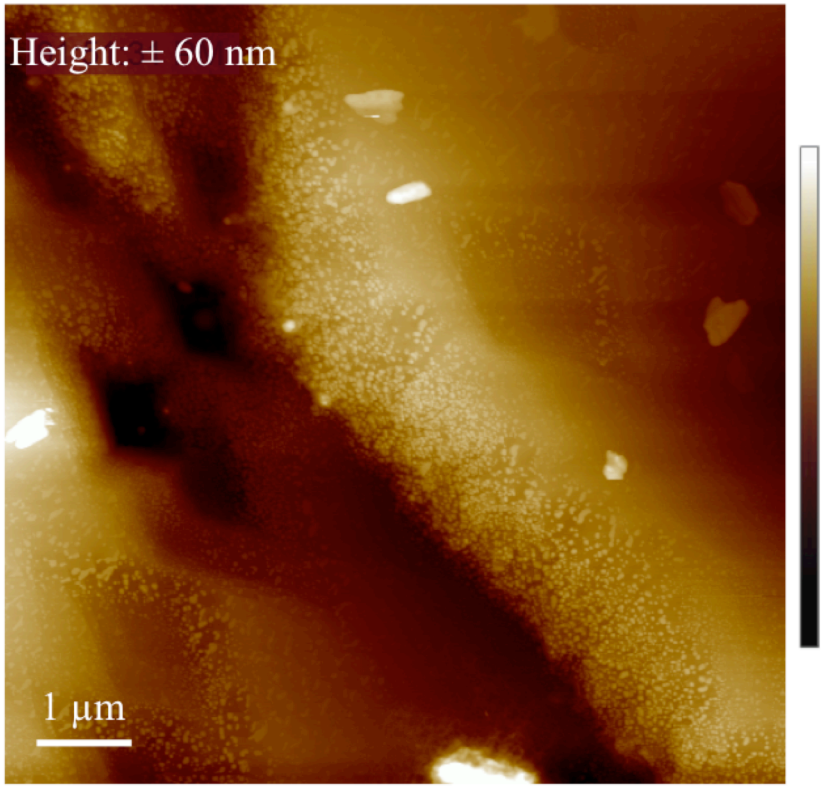

Figure 4. 3. Treated calcite sample with HMDS adsorbed onto edge features. Image taken in fluid (0.1 mM HMDS).

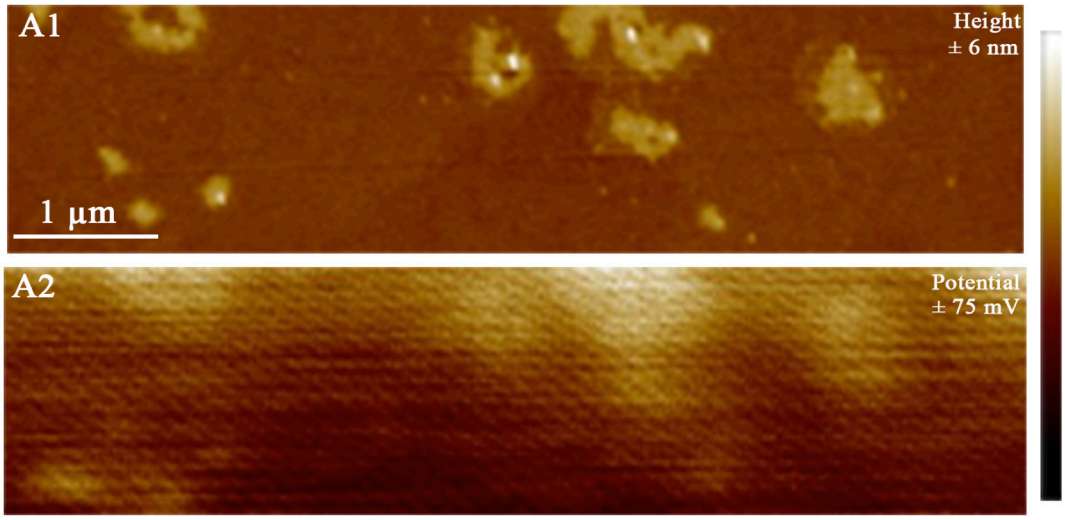

Figure 4. 4. Flat, featureless treated calcite sample with areas of relative higher topography (A) associated to higher surface potential values (B).

At lower magnifications, HMDS adsorbates are visible both on the edge of the terraces and on the flatter portions of the calcite surface; however, the areas of increased surface potential are much larger than the adsorbates themselves (~1 µm in diameter, Figure 4. 5). Here, these higher potential areas are very much associated with the edge of terraces and align almost perfectly with the direction of the edge. One possible explanation for such large-scale surface potential heterogeneities could be the presence of defects in the calcite crystal. Most calcite defects (*e.g.*, ionic substitutions, vacancies, and interstitial impurities) occur at the atomic scale, although there is some evidence that dislocations can produce defects, such as etch pits, on the order of 0.5-1 microns (Hillner et al., 1992; MacInnis and Brantley, 1992). In most cases, these larger defects should be evident with irregularities in the surface topography, yet episodic growth of the crystal can result in surface overgrowth on top of defective material, which, topographically, may appear smooth at lower resolutions (although can be much rougher at high resolution). This phenomenon has been described as a "memory" of surface defects

imbedded in subsequent crystal growth (MacInnis and Brantley, 1992). These slightly deeper defects disrupt the regular bulk mineral structure and could produce variations in the surface potential and possibly affect the reactivity of the surface. This hypothesis, however, needs to be tested further.

In order to obtain a more quantitative and statistically relevant correlation between HMDS adsorption and surface potential, we analyzed a larger set of images collected and found that there is a relationship between higher relief and higher surface potential for oil-wet calcite. Surface potential of HMDS-treated samples showed a higher correlation to relief than untreated samples as revealed by the linear least squares fitting results (Figure 4. 6). The least absolute residuals (LAR) method reduces the impact of outliers and helps reveal correlations on scattered data. Despite some scatter, there is a correlation in the treated samples ($R^2 = 0.92$, $N = 32$), yet no significant linear relationship between potential and relief for the untreated samples ($R^2 = –0.11$, $N = 30$). All samples with topographic ranges above 400 nm were excluded to minimize relief influence on the surface potential.

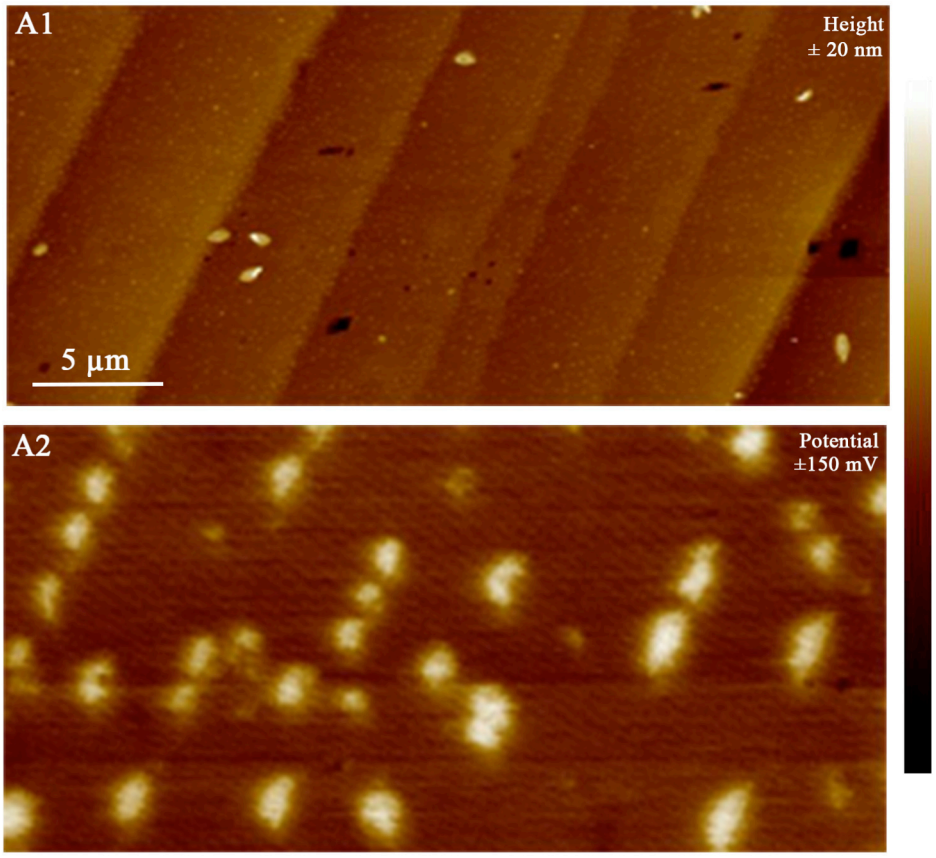

Figure 4. 5. HMDS-treated calcite sample topographic (A1) and surface potential (A2) image. Discrete areas of high surface potential follow the edge of the sample surface terraces. At reduced magnification, high potential features are not discernable on the relief image.

An attempt to quantify differences in surface potential was made using a freshly-cleaved highly-ordered pyrolytic graphite (HOPG) to calibrate the tip. This method utilizes the contact potential difference between the sample and the tip, which is included in the V_S term nullified by the KPFM applied voltage. Each KPFM tip is calibrated against the work function of HOPG, which is always assumed to be 4.6 eV. Work function of the analyzed samples may be estimated as the sum of the tip's work function and the potential measured with KPFM ($WF_{sample} - WF_{tip} = \Delta WF_{measured}$). This procedure, however, proved to be problematic. The expected work function of the Pt/Ir tip was between 5.1 eV and 5.9 eV. However, identical new tips (*i.e.*, same conductive metal, same manufacturer) produced work function estimates that varied from 3.77 eV to 4.59 eV. The tape-peeling technique used to produce a fresh surface of HOPG may not

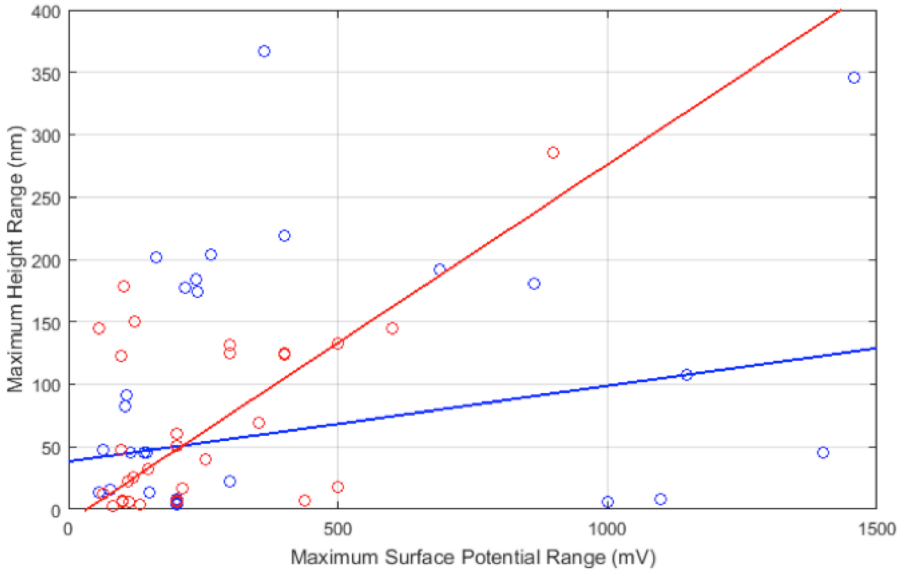

Figure 4. 6. Plot of height range versus surface potential range for all calcite samples analyzed. Blue symbols are sample before reaction with HMDS. Red symbols are samples after reaction with HMDS. Blue and red lines are the robust linear least-square fits for each group. Untreated: N = 30, $R^2 = -0.11$; treated: N = 32, $R^2 = 0.92$.

always result in a clean, compact exposed surface that would reliably correspond to the published value. Even if the freshly peeled graphite surface looks smooth and flat, layers immediately below the surface may be disturbed by the peeling method, creating unexpected potential behavior at the surface. Therefore, we instead emphasize relative differences in surface potential and corresponding charge distribution between the water-wet and oil-wet calcite samples. A more positive surface potential means that electron density is redistributed away from the HMDS adsorbate (and vice versa). This concept is explored in more detail in the computation section.

3.2. Calcite XPS analyses

XPS spectra were collected for water-wet and oil-wet calcite samples in order to understand the changes in the elemental composition and the local bonding environments that occur through wettability alteration on the calcite surface. Although AFM and KPFM offer topographic and surface potential data at nanometer resolution, these techniques do not provide any chemical information about the surface. Therefore, we employ XPS to explore the composition of the surface and interpret the chemical state of surface atoms. XPS is a surface-sensitive spectroscopic technique in which the sample is irradiated with x-rays under ultra-high vacuum conditions to generate photoelectrons from the first few nanometers of the sample surface. A detector then counts and measures the photoelectron kinetic energies from which characteristic electron binding energies (that are atom and orbital specific) are derived.

XPS survey spectra of untreated and treated samples are generally very similar with the exception of N, F, and C peaks (Figure 4. 7). N and F peaks are present on the treated calcite surface, but absent from the untreated calcite. The F likely comes from the

Teflon beaker (polytetrafluoroethylene, PTFE) used for the HMDS reaction. Both the treated and untreated samples were dried in N for similar amounts of time, so while some of this N may be attributed to the N drying environment, the lack of a N peak on the untreated calcite surface means that some N contribution comes from the HMDS molecule on the surface of the treated calcite. The main difference, however, between the two spectra appears in the C peak.

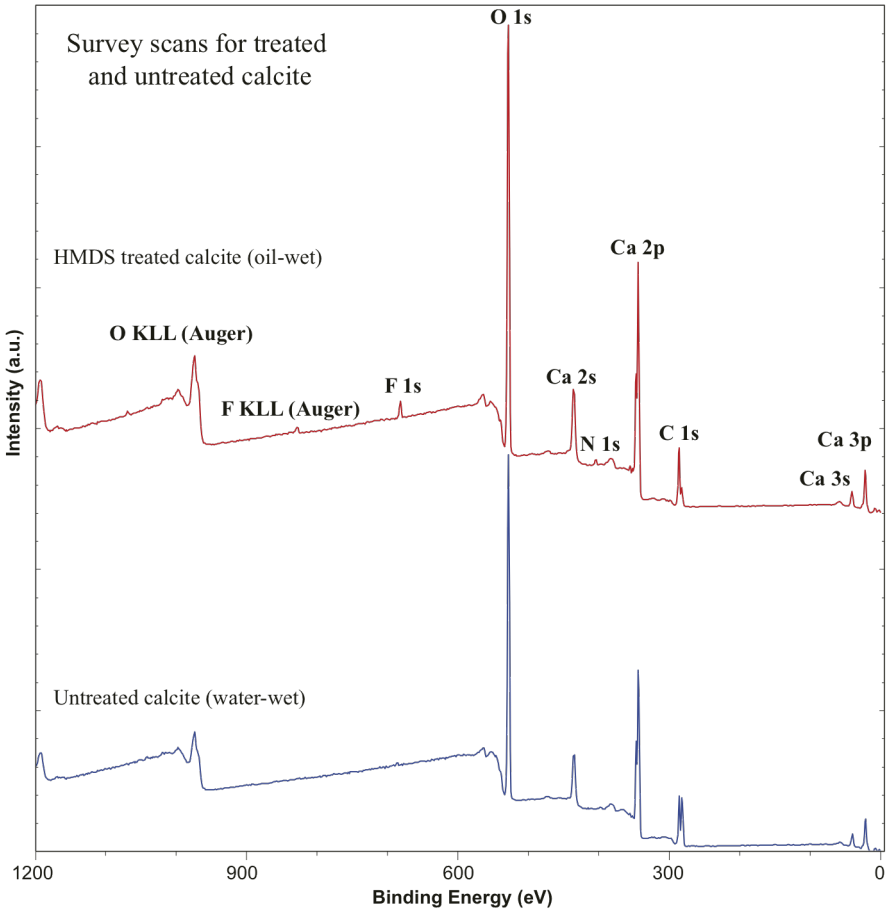

Figure 4. 7. XPS representative spectra of treated (red – above) and untreated (blue – below) calcite samples. Only small differences exists in the treated sample compared to the pure calcite: (1) a peak of F likely derived from the Teflon beaker used for the reaction, and (2) a very small peak that corresponds to N. Analyses conditions: Al Kα monochromated source, 4 sweeps, 100 ms dwell time, 160 eV pass energy.

In the XPS analyses, C peak position and peak morphology vary between the water-wet and the oil-wet calcite samples (Figure 4. 8). While the nominal binding energy of the adventitious C 1s peak is 284.6 eV, differences in bonding partners (*e.g.*, C-O in the carbonate group *vs.* C-H) or bond hybridization can produce subtle shifts in the binding energy peak position, an effect known as chemical shift. By fitting known C peaks to the shifted peaks in the calcite spectra, we can identify which atoms of the surface bond to C and attempt to determine their relationship to the wetting state of the calcite surface.

Four components were used to model C peaks (collected from C core scans ~276-300 eV) using Gaussian-Lorentzian curves and Shirley background subtraction (CasaXPS software version 2.3.17PR1.1): adventitious C (C-C, C-H) at 284.6 eV, aliphatic plus alcohol-ether C at 286.3 eV (C-OH, C-O-C), carbonate C at 289.1 eV (CO_3^{2-}), and bicarbonate C at 289.9 eV (HCO_3^-). The residual standard deviation for both the untreated and treated peak fitting was very close to one, which suggests the difference between the measured and the synthetic data is truly random (CasaXPS 2.3.17PR1.1).. The C peaks show a change in the relative proportion of aliphatic plus alcohol-ether C components to the carbonate and bicarbonate C component. Adventitious C and aliphatic C accounts initially for about 80% of the C signal on the untreated sample. After treatment, this contribution decreases to less than 40%. HMDS adsorbed onto the surface prevents adventitious carbon from the atmosphere and the vacuum chamber to accumulate on the treated calcite, while the untreated sample even after plasma cleaning show substantial accumulation of adventitious carbon after a short exposure to atmosphere and overnight rest in vacuo. Adventitious C is ubiquitous and will be present

unless the surface is never exposed to solutions or the atmosphere, or even to a vacuum chamber, for any period of time (Stipp and Hochella Jr, 1991). The difficulty of adventitious C to repopulate the treated calcite at a rate comparable to that of the water-wet surface along with the reduction of the contribution to the O peak from the hydrated Ca component shows how the oil-wetting mechanism drastically reduces the availability of surface sites for adsorption and hydration.

Comparing XPS peak areas is one way to determine the relative abundance of elements on the sample surface. Compositional abundance ratios were calculated for the untreated and treated samples using the Ca $2p_{1/2}$, C 1s, and O 1s peaks from survey scan spectra (rather than core spectra to ensure comparable analytical conditions, *i.e.*, number of scans, scan range, acquisition time). Untreated calcite produced a Ca:C:O ratio of 1.0:1.1:2.6 while treated samples resulted in 1.0:1.2:2.5 (compared with the ideal calcite stoichiometric ratio 1.0:1.0:3.0). Only the contribution of the carbonate C component was considered. These results suggest that a change in wettability does not significantly affect the average composition of the surface, although the O peak for the untreated, water-wet sample is larger than that of the treated, oil-wet sample, which we interpret as the presence of water molecules (or OH^-) adsorbed onto the water-wet calcite surface. In comparison, the oil-wet, treated calcite has a smaller O peak due to the lack of water molecules present on the surface. A smaller O peak would account for a slightly larger C:O ratio in the treated sample in comparison with untreated sample. The presence adventitious C does not allow a more detailed assessment of the compositional changes exerted over the calcite surface by the HMDS adsorption.

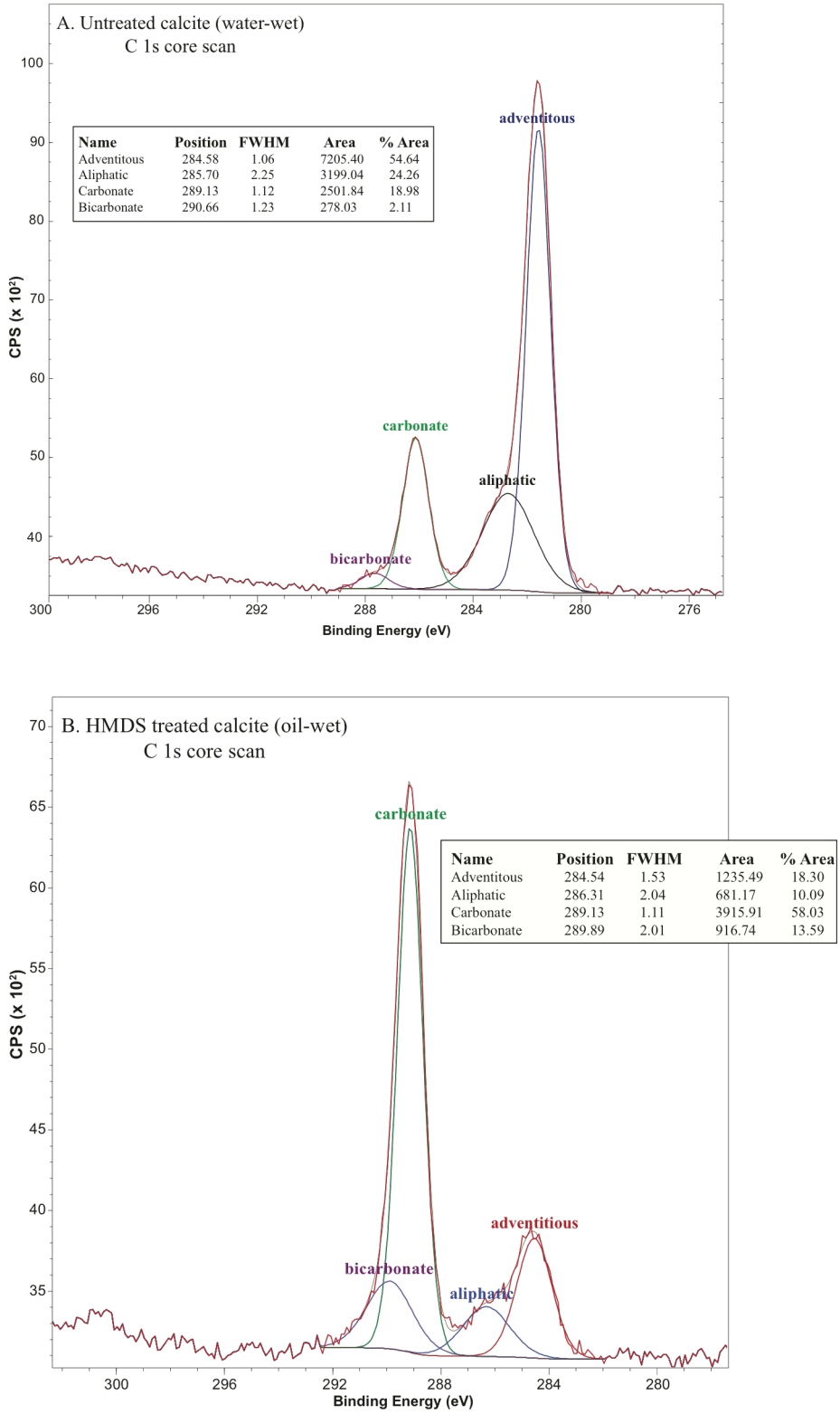

Figure 4. 8. Peak models fitted to the C narrow scans of untreated (A) and treated (B) calcite samples.

3.3. Computational results

3.3.1. Calculations on infinite surface slabs using periodic boundary conditions

The surface potential of a solid, which is dependent on the work function (see Methods section), is highly sensitive to the presence of contamination and adsorbates. Depending on the charge distribution and the electronegativity of the adsorbed species, the work function can either increase or decrease. In some cases, adsorbates on the surface bind with surface electrons, which can make it more difficult to remove these electrons (*i.e.*, the work function often increases with contamination). This behavior is observed in our experiments with calcite and HMDS. After reacting the calcite sample with HMDS, the surface becomes oil-wet, and the work function increases from approximately 5.29 eV to 5.50 eV. Discussed previously, the procedure used to obtain these values proved to be problematic, and we emphasize the increase in WF rather than the actual values.

Thus, the first task of the quantum-mechanical calculations described here is to test if this increase in work function can be reproduced computationally, what its magnitude is, and what changes in density of state or surface states/orbitals may be causing these changes in work function. In addition, these calculations help us understand which surfactant has a high affinity to specific mineral surfaces, which is often dependent on epitaxial and polarity match of functional groups of surfactants and specific surface sites, which are often steps and kinks.

An increase in work function is observed in quantum mechanical calculations between a pristine calcite $\{10\bar{1}4\}$ surface and one with HMDS adsorbed. The average work function increases from 5.39 eV to 5.52 eV (for one HMDS molecule per calcite

slab, which consists of 2×2 calcite supercell, 12 Å thick). Although both the experimentally-determined and calculated WFs are very close in value, the WF of a surface can change with external parameters that can be difficult to control in a laboratory setting, such as temperature, relative humidity, AFM tip geometry, or adventitious carbon surface contamination. For these reasons, we emphasize the relative increase in WF rather than the exact value. Because KPFM observations show that HMDS is preferentially associated to edges, we utilize computational modeling to take a closer look at these specific features and explore HMDS adsorption behavior on different calcite surface sites.

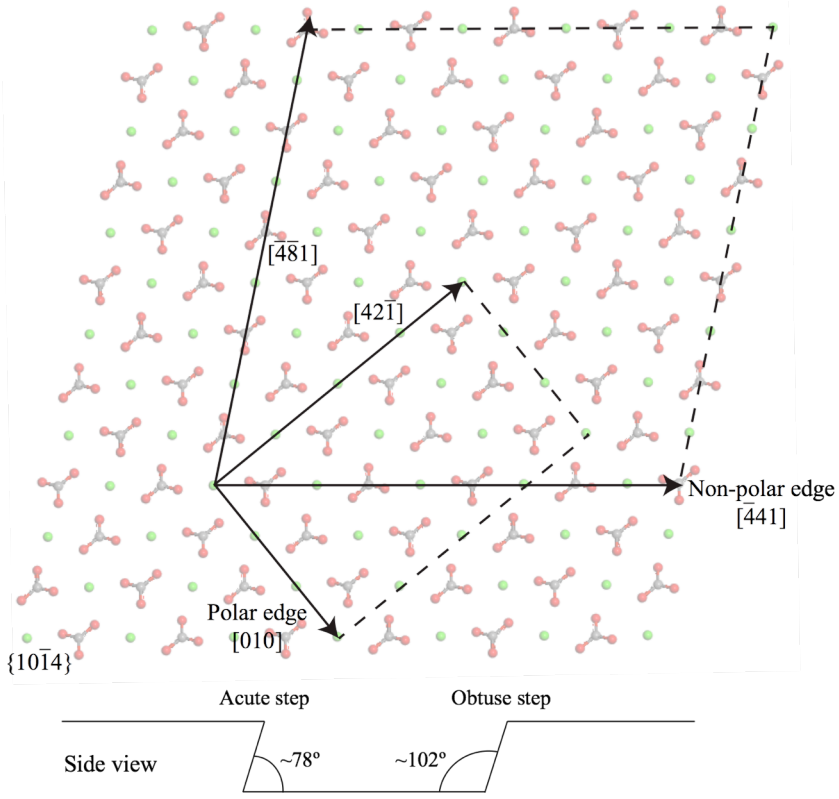

Figure 4. 9. Model of the $\{10\bar{1}4\}$ calcite surface indicating the crystallographic directions for the polar and non-polar edges. Only the top surface layer of atoms is drawn. The side view showing acute and obtuse steps is also shown.

Much evidence suggests that 'perfect' mineral surfaces (such as a stoichiometric $\{10\bar{1}4\}$ surface) are relatively unreactive and that adsorption is primarily promoted by surface defect sites such as edges, kinks, and vacancies (Henrich and Cox, 1996). For this reason, the adsorption energies for HMDS on the $\{10\bar{1}4\}$ surface and on non-polar and polar step edges were calculated using periodic models to simulate these extended linear features. (Other defect sites are discussed in the next section.) The non-polar edges run parallel to the $[\bar{4}41]$ and $[\bar{4}\bar{8}1]$ crystallographic directions and consist of alternating cations and anions known as periodic bond chains (PBCs). The polar edges, bound by $[42\bar{1}]$ and $[010]$, have rows of either all cations or all anions (Figure 4. 9). Additionally, calcite has a hexagonal lattice structure, and when cleaved, a set of $\{10\bar{1}4\}$ planes intersect to form a rhombohedron. On this rhombohedron (looking at a side view), two possible steps can form: a step with an obtuse angle (102º) between the higher and lower $\{10\bar{1}4\}$ planes and a step with an acute angle (78º) (Figure 4. 9) (Kristensen et al., 2004). These steps are referred to as the obtuse and acute steps in our model. Both non-polar and polar edges may form either acute or obtuse angles with the underlying layer, and the polar edge may consist of either Ca atoms or CO_3 molecules. This variability leaves quite a few choices (crystallographic direction, acute or obtuse angle, and for the polar side, Ca^{2+}or CO_3^{2-}), which we systematically explored using a periodic, monoatomic step model. HMDS adsorption energies were calculated for each calcite edge configuration from the following equation: $CaCO_{3(slab)}$ + HMDS ⇔ $CaCO_{3(slab)}$_HMDS (Table 4. 1).

Table 4. 1. HMDS adsorption energies onto flat calcite surface, polar, and non-polar step edges.

Surface site	Adsorption energy (eV)	
Terrace	-0.81	
Polar edge	**Acute**	**Obtuse**
Ca [$\mathbf{42\bar{1}}$]	-0.22	0.22
Ca [**010**]	-0.65	-0.33
CO_3 [$\mathbf{42\bar{1}}$]	-0.0038	-0.0038
CO_3 [**010**]	-0.0049	-0.17
Non-polar edge	-0.59	-0.54

In general, HMDS adsorption onto the flat terrace site resulted in the most favorable adsorption energy, followed by the non-polar edges, the Ca-dominated edges, and finally the CO_3-dominated edges. There are, however, a few exceptions to this trend. The acute Ca [**010**] edge produced the second most favorable HMDS adsorption energy (-0.65 eV). Calculations reveal that, at this site, the HMDS molecule bends, and the two trimethylsilyl groups [$Si(CH_3)_3$] move away from the surface, while the central N atom moves closer to the Ca atoms on the calcite edge (N-Ca bond distance = 2.6 Å). The Si-N-Si bond angle decreases from 133.5º to 127.9º, which allows the HMDS amine group to donate electron density to the Ca (and produce a more positive surface potential). The polar NH functional group favoring the calcite step helps to explain how HMDS alters the wettability of the calcite from water-wet to oil-wet. HMDS acts as a bridging molecule between the charged surface and the non-polar hydrocarbon fluid. To make the surface oil-wet, the NH group "attacks" the surface, while the aliphatic methyl groups reach out to the bulk fluid side.

Another exception to the trend is the Ca $[42\bar{1}]$ obtuse polar edge, which produces the least favorable HMDS adsorption energy (0.22 eV). Here, the HMDS molecule is pushed up and away from the Ca edge, so that the final N-Ca distance is 4.8 Å. Comparing the structure of the $[42\bar{1}]$ and the $[010]$ steps, the Ca-Ca spacing on the $[42\bar{1}]$ edge is smaller than that of the $[010]$ edge (4.0 *vs*. 4.9 Å), meaning that there is a higher density of Ca atoms per $[42\bar{1}]$ unit cell. Additionally, the obtuse angle between the step and the substrate exposes an underlying row of Ca atoms beneath the HMDS molecule. This abundance of Ca atoms both on the edge and in the substrate prevents the HMDS N from bonding with Ca edge atoms. As the methyl groups approach the surface, they experience electrostatic repulsion from excess Ca atoms.

The steric effects associated with polar and non-polar steps bring to light the influence of the substrate in these monoatomic step configurations. Compared to the flat terrace site, HMDS adsorption onto the step edges was in general more positive; however, this result is likely due to repulsion of the HMDS molecule from the substrate beneath the step. The monolayer step model is representative of relatively flat areas of calcite surfaces with small steps; however, some of the edges observed in AFM/KPFM experiments were much larger than a single atomic monolayer. In order to simulate a taller step (*i.e.*, a step that has multiple atomic layers above the substrate), we use a cluster model to create Ca and CO_3 edges along the $[42\bar{1}]$ and $[010]$ directions. These results are discussed in the next section.

3.3.2. Cluster calculations

Models with periodic boundary conditions are useful for studying extended linear features; however, in order to investigate HMDS adsorption on additional calcite surface

sites, such as kink sites and corners of islands, we employ a cluster model that includes acute and obtuse step edges as well as cation and anionic corner sites. Nine different sites were used to calculate HMDS adsorption energies: the center of the island terrace, an acute step edge (a non-polar edge), a Ca^{2+} kink site on the acute edge, a CO_3^{2-} kink site on the acute edge, an obtuse edge (also a non-polar edge), Ca^{2+}/CO_3^{2-} kink sites on the obtuse edge, a Ca^{2+} corner site, and finally CO_3^{2-} corner site. The kink sites were prepared using the calcite $\{10\bar{1}4\}$ slab (4 × 4 units) with one layer (8 × 8 units) substrate underneath the slab (total 200 atoms). Two molecules in the $[\bar{4}\bar{8}1]$ direction were cut out from the corner of calcite island to make an acute kink site with CO_3^{2-} (CO_3 acute kink). Four different kink sites were made using the four different corners in the same manner, so that both the acute and obtuse edges have a Ca^{2+} kink and a CO_3^{2-} kink. For these calculations, the geometry of the calcite island and substrate was fixed, and the initial orientation of the HMDS molecule was tested so that the NH group was pointing either towards the calcite island or away from the calcite island. In every case, the NH group pointing towards the calcite generated consistently more favorable adsorption energies; therefore, we only report those values (Table 4. 2).

Table 4. 2. Adsorption energies for calcite island model with HMDS (with and without hydration effects). The sites with the four lowest adsorption energies (bold) are as follows: Ca corner (-1.17) < Ca acute kink (-1.05) < Ca obtuse kink (-0.92) < Terrace (-0.59).

Position	COSMO (eV)	Without COSMO (eV)
Terrace	-0.59	-1.22
Non-polar edges		
Acute edge	-0.54	-1.71
Obtuse edge	-0.58	-1.92
Corner sites		
Ca corner	**-1.17**	**-2.75**
CO_3 corner	-0.46	-1.74
Kink sites		
Ca acute kink	**-1.05**	**-2.74**
Ca obtuse kink	**-0.92**	**-2.46**
CO_3 acute kink	-0.37	-2.23
CO_3 obtuse kink	-0.51	-2.20

The site most energetically favorable for HMDS adsorption is a Ca^{2+} corner site both for calculations using COSMO to simulate the effect of hydration ($\Delta E = -1.17$ eV) and without COSMO (–2.75 eV, Table 4. 2). Adsorption energies at sites that were calculated with and without periodic boundary conditions (*i.e.,* the terrace, and acute/obtuse non-polar edges) are in very good agreement with each other. In general, Ca^{2+} sites are more favorable than CO_3^{2-} sites. As would be expected, adsorption energies not considering the effect of hydration (those without COSMO) are more negative than those with COSMO. This net shift towards more positive energies is due to the partial loss of the HMDS hydration sphere. In an aqueous fluid (which is approximated with a dielectric continuum model in these calculations), HMDS is completely surrounded with

water molecules; however, in order for the HMDS to adsorb onto the calcite surface, some of the water molecules must break their bonds with the HMDS, which results in an energy penalty. At the Ca corner site, the HMDS molecule is centered on the Ca corner ion, and the H of the NH group is pointed inward towards the calcite island, but the H tips upward away from the Ca. The bond distance between the N and the Ca is 2.54 Å (which is very similar to the N-Ca distance at the Ca polar edge calculated with periodic boundary conditions). The two trimethylsilyl groups flex away from the corner site and move away from the calcite island. The Si-N-Si bond angle decreases from 133.5° (for an isolated optimized HMDS molecule) to 126.2°. Orbital projections show that there is a high degree of covalency between the N from the HMDS and the Ca from the calcite corner (Figure 4. 10); two lobes of the Ca and N *2p* orbitals overlap to form a π bond at the corner site. The formation of π bonds and π stacking (or π-π bonding) is an important interaction between aromatic rings, particularly for benzene dimers (Hunter and Sanders, 1990). This mechanism helps explain the geometry and bonding of molecules without net dipolar moments (but strong quadrupole moments), such as those found in oil. The propensity of HMDS to form π bonds with Ca^{2+} on the calcite and potentially with aromatic components of oil may be significant for HMDS as a wettability modifier.

As described in the previous section, adsorption energies onto monoatomic polar steps may be influenced by rows of cations or anions in the underlying calcite substrate. To eliminate any possible interactions between the HMDS and the substrate, we calculated HMDS adsorption energies using a rotated 4 × 4 calcite island to simulate taller step edges (Table 4. 3). Among these calculations, adsorption onto the Ca [010] step was the most favorable (N-Ca distance = 2.6 Å). This same result was achieved

using periodic step models (Table 4. 1). Adsorption onto the CO_3-dominated steps is generally less favorable, likely because of the strong interaction between the central N atom of the HMDS and the Ca atoms available on Ca-dominated steps. In context with the other calcite surface sites, the Ca [010] step is the third most favorable type of site behind the Ca corner and Ca kink sites.

Table 4. 3. HMDS adsorption energies for polar edges without calcite substrate.

Position	Adsorption energy (eV)
Ca 421 edge	-0.48
Ca 010 edge	-0.82
CO_3 421 edge	-0.11
CO_3 010 edge	-0.07

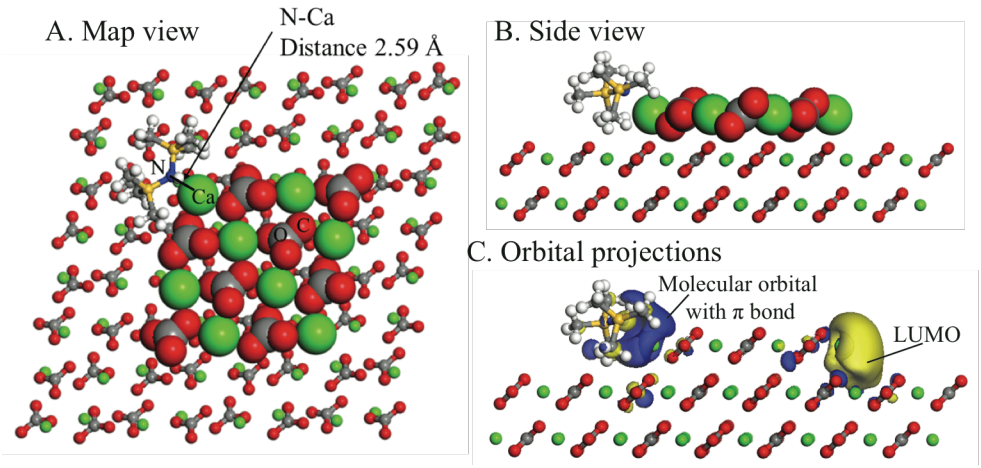

Figure 4. 10. Optimized geometry and electronic structure of HMDS adsorption onto a calcite Ca^{2+} corner site (A) and (B). Predicted geometry of HMDS on a calcite island corner site. The atoms of the island are shown as larger spheres for clarity. (C) Projections of the lowest occupied molecular orbital (LUMO) and a π-bonding orbital 0.82 eV above the LUMO.

As mentioned in the introduction, the surface charge of calcite (and all other minerals) is highly dependent on the pH of the surrounding fluid. Excess H^+ adsorbed onto the surface causes a net positive surface charge at pH conditions below the PZC (and *vice versa* with excess OH^- above the PZC). Because calcite's PZC is relatively basic, calcite surfaces are positively charged at most pH conditions (pH < 9.5). Therefore, we couple HMDS adsorption with protonation and hydroxylation of the calcite surface (H^+ and OH^- adsorption, respectively) to account for excess ions present at different pH conditions. For H^+ coadsorption, the acute edge was the most favorable site for adsorption of HMDS, while the Ca obtuse kink site was more favorable with OH^- coadsorption (*vs.* the Ca corner site for HMDS adsorption only) (Table 4. 4). Geometry optimizations indicate that H^+ serves as a link between the O from a calcite CO_3 group and the N from the HMDS. The HMDS once again bends so that a methyl group bends away from the surface out into the bulk fluid (as a potential linker for other hydrophobic molecules to bond with). The other methyl group moves towards and centers on a Ca atom adjacent to the H-CO_3.

With HMDS + OH^- coadsorption at the Ca obtuse kink site, the OH^- is situated between the two adjacent Ca^{2+} at and near the kink, with its O pointing towards the CO_3^{2-} in between the adjacent Ca atoms (Figure 4. 11). A closer look at this optimized structure shows that hydroxide is closer to the Ca^{2+} at the calcite kink with a distance of 2.37 Å. HMDS adsorbs on top of the Ca^{2+} at the kink as one side of its trimethylsilyl group slightly tilted to the surface of calcite substrate layer. The distance between the hydrogen of NH group in HMDS and the oxygen of hydroxide is 1.96 Å. Unlike the proton coadsorption case, hydroxide does not locate between the HMDS and calcite cluster.

These results confirm KPFM observations that HMDS preferentially adsorbs to calcite step edges, especially at pH < 9.5 where more H^+ is expected to be present on the surface. At pH > 9.5 and more surface OH^- is available, Ca kink sites, specifically those on obtuse edges, are more likely to be the site of HMDS adsorption and nucleation.

Table 4. 4. Adsorption energies for HMDS adsorption only and with H^+ and OH^- on various calcite surface sites. All reaction energies here include the effects of hydration. The bolded lines indicate the most favorable positions and coadsorption energies.

Coadsorbate	Position	HMDS only (eV)	HMDS with coadsorbate (eV)	Difference (eV)
H^+	CO_3 corner	-0.46	-0.53	-0.07
	Acute edge	**-0.54**	**-1.10**	**-0.56**
	Terrace	-0.59	-0.35	+0.24
	CO_3 obtuse kink	-0.51	-0.85	-0.35
	CO_3 acute kink	-0.37	-0.59	-0.22
OH^-	Ca corner	-1.17	-0.79	+0.38
	Acute edge	-0.54	-0.46	+0.08
	Terrace	-0.59	-0.87	-0.28
	Ca obtuse kink	**-0.92**	**-1.17**	**-0.25**
	Ca acute kink	**-1.05**	**-1.00**	**+0.05**

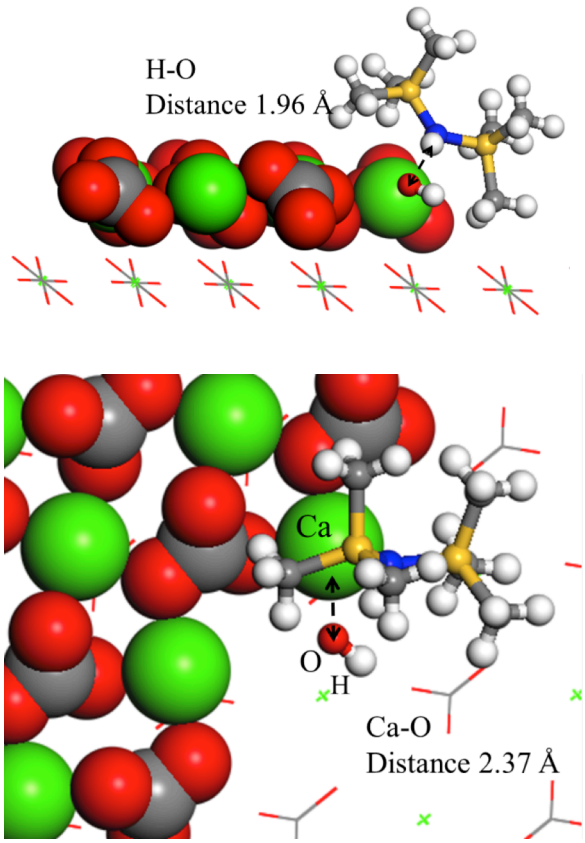

Figure 4. 11. HMDS adsorption with OH^- on the Ca obtuse kink site.

An additional set of calculations was performed using the hybrid B3LYP functional in combination with Lee-Yang-Parr correlation functional in order to test the dependency of the exchange correlation of our results (Lee et al., 1988; Becke, 1993). These calculations were implemented with the Gaussian 09 package with LANL2DZ (Los Alamos with effective core potential and polarization function on Ca) and 6-31G* basis sets. Here, a smaller $Ca_8(CO_3)_8$ cluster with 40 atoms was used to minimize computational expense. All atoms in calcite clusters were once again fixed for both structures, and the geometry of HMDS was allowed to optimize. Water solvated models were calculated with the most widely used solvation models, Polarizable Continuum Model (PCM) and Conductor-like Polarizable Continuum Model (CPCM) model

(Miertuš et al., 1981; Barone and Cossi, 1998; Tomasi et al., 2005). CPCM model is a variation of PCM model which considers the dielectric continuum as a conductor-like continuum. These results support our initial calculations where HMDS only prefers the corner site of Ca on calcite relative to all other surface sites ($\Delta E = -1.74$ eV without solvation effects, -0.24 eV with PCM, and -0.25 eV with CPCM with LANL2DZ basis set). Results were very similar to these using the 6-31G* basis set (-1.67 eV w/o solvation and -0.36 eV with CPCM). While the overall reaction energy from B3LYP calculations is on the order of 1 eV more positive than those for GGA-PBE, the overall trend remains the same.

4. Conclusions

Surface potential measurements and XPS analyses indicate that the adsorption of hexamethyldisilazane changes the wetting preference of calcite surfaces from water-wet to oil-wet. AFM observations of preferential HMDS adsorption onto edge features are confirmed with molecular simulations, which suggest that Ca-dominated edges, Ca corners, and Ca kink sites are the most favorable sites for adsorption. This adsorption is coupled with an increase in surface potential wherever there are HMDS adsorbates on the surface, which implies that electron density moves from HMDS to Ca. Molecular simulations also reveal that the HMDS molecule is amphoteric and capable of interacting with both H^+ and OH^- surface groups, meaning that this molecule may function as an efficient wettability modifier at a range of pH conditions.

The observation that oil adsorption occurs at the edges of minerals has implications what types of surfaces may be prone to wettability alteration. Freer et al. (Freer et al., 2003) suggest that the edges of minerals destabilize the water film on

hydrophilic surfaces by penetrating through the film to allow for direct contact between the mineral and oil (or other hydrocarbon fluids). Therefore, calcite substrates with higher densities of edges and corner features, such as very fine grained chalk formations, may be more likely to become mixed-wet or oil-wet after hydrocarbon migration. While this work was limited to one particular wettability modifier and substrate, we extrapolate further that amines or other ammonia derivatives might attach themselves to mineral surfaces when these surfaces come into contact with non-aqueous fluids. To our knowledge, this study is the first application of KPFM on mineral surfaces to study wettability. With further development through the use of other mineral substrates (*e.g.,* quartz, pyrite, or clay minerals) and wettability modifiers, like commercial surface-active compounds and/or in the presence of brines, KPFM has the potential to reveal how interactions between specific functional groups and surface sites modifies the electronic structure of the mineral surface and produce changes in hydrophobicity.

Appendix 4.A

4.A.1 Additional KPFM images of water-wet and oil-wet calcite

Additional images of water-wet and oil-wet calcite are shown in Figure 4.A 1. The water-wet calcite surface has no correlation with topography and surface potential. In the oil-wet sample, terraces approximately 10 nm tall are shown in the center of the height image (B1), and a well-defined line of hemispherical particles is visible on the edge of each terrace. The brighter spots indicate an increase in surface potential.

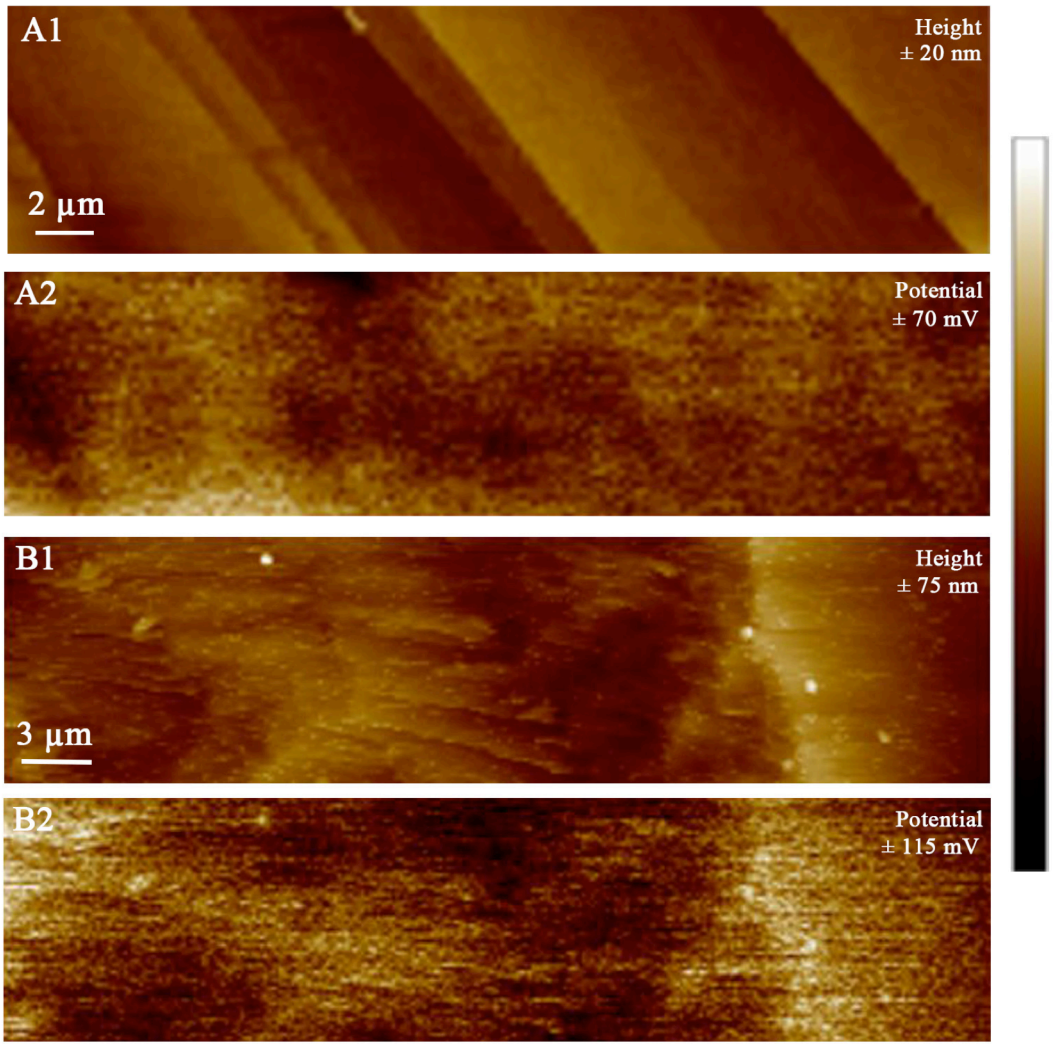

Figure 4.A 1. Figure S1. Topographic and surface potential images of untreated calcite surface with well-developed clean surface terraces (A1 and A2). Height (B1) and surface potential (B2) of calcite treated with HMDS.

References

Abdallah W., Buckley J. S., Carnegie A., Edwards J., Herold B., Fordham E., Graue A., Habshy T., Seleznev N., Signer C., Hussain H., Montaron B. and Ziauddin M. (2007) Fundamentals of wettability. *Oilf. Rev.* **19**, 44–63.

Al-Anssari S., Barifcani A., Wang S. and Iglauer S. (2016) Wettability alteration of oil-wet carbonate by silica nanofluid. *J. Colloid Interface Sci.* **461**, 435–442.

Anderson W. (1986a) Wettability literature survey-Part 1: Rock/oil/brine interactions and the effects of core handling on wettability. *J. Pet. Technol.* **39**, 121–125.

Anderson W. (1986b) Wettability literature survey-Part 2: Wettability measurement. *J. Pet. Technol.* **38**, 241–246.

Barone V. and Cossi M. (1998) Quantum calculation of molecular energies and energy gradients in solution by a conductor solvent model. *J. Phys. Chem. A* **102**, 1995–2001.

Becke A. D. (1993) Density-functional thermochemistry. III. The role of exact exchange. *J. Chem. Phys.* **98**, 5648–5652.

Bohr J., Wogelius R. A., Morris P. M. and Stipp S. L. S. (2010) Thickness and structure of the water film deposited from vapour on calcite surfaces. *Geochim. Cosmochim. Acta* **74**, 5985–5999.

Delley B. (1990) An all-electron numerical method for solving the local density functional for polyatomic molecules. *J. Chem. Phys.* **92**, 508–517.

Freer E. M., Svitova T. and Radke C. J. (2003) The role of interfacial rheology in reservoir mixed wettability. *J. Pet. Sci. Eng.* **39**, 137–158.

Henrich V. E. and Cox P. A. (1996) *The Surface Science of Metal Oxides*., Cambridge University Press.

Hillner P. E., Gratz A. J., Manne S. and Hansma P. K. (1992) Atomic-scale imaging of calcite growth and dissolution in real time. *Geology* **20**, 359–362.

Hunter C. A. and Sanders J. K. M. (1990) The nature of pi-pi interactions. *J. Am. Chem. Soc.* **112**, 5525–5534.

Kahn A. (2016) Fermi level, work function and vacuum level. *Mater. Horizons* **3**, 7–10.

Klamt A. and Schuurmann G. (1993) COSMO: a new approach to dielectric screening in solvents with explicit expressions for the screening energy and its gradient. *J. Chem. Soc. Perkin Trans. 2* **0**, 799–805.

Kristensen R., Stipp S. L. S. and Refson K. (2004) Modeling steps and kinks on the surface of calcite. *J. Chem. Phys.* **121**, 8511–8523.

Lee C., Yang W. and Parr R. G. (1988) Development of the Colle-Salvetti correlation-energy formula into a functional of the electron density. *Phys. Rev. B* **37**, 785–789.

Liu J., Gaikwad R., Hande A., Das S. and Thundat T. (2015) Mapping and quantifying surface charges on clay nanoparticles. *Langmuir* **31**, 10469–10476.

MacInnis I. N. and Brantley S. L. (1992) The role of dislocations and surface morphology in calcite dissolution. *Geochim. Cosmochim. Acta* **56**, 1113–1126.

Mélin T., Zdrojek M. and Brunel D. (2010) Electrostatic force microscopy and kelvin force microscopy as a probe of the electrostatic and electronic properties of carbon nanotubes. In *Scanning Probe Microscopy in Nanoscience and Nanotechnology* (ed. B. Bhushan). Springer Berlin Heidelberg, Berlin, Heidelberg. pp. 89–128.

Melitz W., Shen J., Kummel A. C. and Lee S. (2011) Kelvin probe force microscopy and its application. *Surf. Sci. Rep.* **66**, 1–27.

Miertuš S., Scrocco E. and Tomasi J. (1981) Electrostatic interaction of a solute with a continuum. A direct utilizaion of AB initio molecular potentials for the prevision of solvent effects. *Chem. Phys.* **55**, 117–129.

Moro D., Ulian G. and Valdrè G. (2016) Nanoscale cross-correlated AFM, Kelvin probe, elastic modulus and quantum mechanics investigation of clay mineral surfaces: The case of chlorite. *Appl. Clay Sci.* **131**, 175–181.

Morrow N. R. (1990) Wettability and its effect on oil recovery. *J. Pet. Technol.* **42**, 1471–1484.

Na C., Kendall T. A. and Martin S. T. (2007) Surface-potential heterogeneity of reacted calcite and rhodochrosite. *Environ. Sci. Technol.* **41**, 6491–6497.

Osthoff R. C. and Kantor S. W. (1957) Organosilazane Compounds. In *Inorganic Syntheses* John Wiley & Sons, Inc. pp. 55–64.

Perdew J. P., Burke K. and Ernzerhof M. (1996) Generalized gradient approximation made simple. *Phys. Rev. Lett.* **77**, 3865–3868.

Plueddemann E. P. (1982) *Silane Coupling Agents*., Springer US.

Stipp S. L. and Hochella Jr M. F. (1991) Structure and bonding environments at the calcite surface as observed with X-ray photoelectron spectroscopy (XPS) and low energy electron diffraction (LEED). *Geochim. Cosmochim. Acta* **55**, 1723–1736.

Stipp S. L. S. (1999) Toward a conceptual model of the calcite surface: hydration, hydrolysis, and surface potential. *Geochim. Cosmochim. Acta* **63**, 3121–3131.

Tkatchenko A. and Scheffler M. (2009) Accurate molecular Van der Waals interactions from ground-state electron density and free-atom reference data. *Phys. Rev. Lett.* **102**, 73005.

Tomasi J., Mennucci B. and Cammi R. (2005) Quantum Mechanical Continuum Solvation Models. *Chem. Rev.* **105**, 2999–3094.

Valdre G. (2007) Nanomorphology and surface potential of layer silicates by scanning probe microscopy. *Acta Crystallogr. Sect. A* **63**, s84.

Zhang P., Tweheyo M. T. and Austad T. (2007) Wettability alteration and improved oil recovery by spontaneous imbibition of seawater into chalk: Impact of the potential determining ions Ca^{2+}, Mg^{2+}, and SO_4^{2-}. *Colloids Surfaces A Physicochem. Eng. Asp.* **301**, 199–208.

CHAPTER 5
Conclusions

Investigations of the nanometer-scale phenomena at the mineral-fluid interface have provided us with a wealth of information about the reactions that occur at the mineral-fluid interface. These interactions play an essential role in moderating the solubility and mobility of potentially harmful contaminants in surface water and groundwater systems. Because of the small scale of these processes, special methods are needed to probe mineral surface reactions. The goal of the chapters in this dissertation is to describe the development and application of new techniques to investigate processes that ultimately affect the mobility of contaminants in contact with mineral surfaces. With this information and with other novel ways to study these interactions, we are better equipped to explain observations in the field and predict much larger scale geochemical processes and events.

Chapter 2 presents a new strategy to model how radionuclides are incorporated into carbonate and sulfate minerals. Incorporation reactions can trap contaminant species into mineral phases and control immobilization/release pathways for chemical species in low-temperature and near-surface environments. This approach combines different types of quantum-mechanical models (periodic and cluster configurations) to describe how hydrated, ionic species replace components of a host mineral and to calculate thermodynamic properties independently from experimental parameters, the latter of which may not reflect long-term equilibrium conditions. Along the way, we learn that

using cluster models and including the effects of hydration lowers the incorporation energy on the order of 1.5 eV and that incorporation occurs preferentially at defect sites such as vacancies and impurities. While the computational methodology applied here allows us to evaluate the overall thermodynamic stability of the final incorporated phase, one way to further expand upon this approach would be to include the kinetic effects of incorporation, *i.e.*, the precise pathway of the incorporated ion. To be specific, our calculations do not consider if an ion first adsorbs to the mineral surface and diffuses into the bulk mineral or if true coprecipitation occurs. In order to calculate the chemical rate constants for these reactions, we would need to integrate additional methods such as transition state theory or collision theory. Additionally, other types of incorporation processes, such as trace element enrichment in ore deposit minerals, frequently occur in high-temperature geologic settings such as magmatic or hydrothermal systems. Modeling these high temperature and high pressures systems with first principles would require a quantum-mechanical molecular-dynamics model using large unit cells, which can be extremely expensive computationally, but nevertheless an important future direction for the work presented here.

The reductive precipitation of Cr(VI) to Cr(III) described in Chapter 3 is an important mechanism for reducing Cr(VI) concentrations in surface and groundwater environments. The primary contribution of this study was to combine electrochemical methods with atomic force microscopy in order to image the deposition of Cr on the surface of magnetite at variable Eh and pH conditions and to quantify this information with detailed analyses of the resulting images. Our experimental setup allows for the precise controls of redox conditions and solution chemistry (pH, ionic strength), and

observations of the mineral surface can be made *in situ*. The redox transitions between Cr(III) and Cr(VI) at pH 7 were in agreement with the Eh conditions predicted from thermodynamic calculations, yet these predictions broke down at more extreme pH conditions where perhaps less thermodynamic information on Cr speciation is available (highlighting the need for more robust thermodynamic databases of contaminant speciation). Although growth was observed in the EC-AFM images at pH 11, no Cr was detected on the surface with XPS, and elevated Fe(II)/Fe(III) and Fe(III) satellite structures indicate that the magnetite surface at pH 11 is slightly oxidized. Therefore, we interpret this surface oxidation as a passivating layer that inhibits further Cr(VI) reduction, even though reductants are available. EC-AFM may be a helpful tool for studying the deposition and dissolution of redox-active contaminants on minerals surfaces. A limitation of this method, however, is that only semiconducting minerals may function as working electrodes, yet some of these minerals (*e.g.*, pyrite FeS_2 and certain clay minerals with sufficient Fe) are often abundant in sulfide-rich reducing environments. In addition, it is often the semiconducting transition metal oxides and sulfides that catalyze redox reactions of geochemical or environmental importance. Other semiconducting sulfide minerals like galena (PbS), realgar (AsS), cinnabar (HgS), and sphalerite (ZnS) are composed of metal or metalloid species that themselves are considered contaminants at high concentrations. Therefore, EC-AFM can be used to carefully verify the stability of these minerals and the conditions at which their dissolution products may be released into the environment.

In Chapter 4, the relationship between surface structure, surface potential, and wettability alteration are explored through Kelvin probe force microscopy and molecular

simulations of calcite surfaces. By using an oil-proxy, HMDS, we learn that this molecule preferentially adsorbs onto edges and Ca corner sites on the surface, which causes a heterogeneous increase in surface potential. This result is perhaps an indication that other amine-based or ammonia-derived molecules may react with specific sites on calcite to render the surface oil-wet and that carbonate formations (or carbonate-rich soils) with small grains and small pores (*i.e.,* higher surface areas and higher densities of steps and corner sites) may be potentially more predisposed to wettability alteration. With KPFM, we can generate very high resolution maps of heterogeneities in the surface potential, which may be relevant for surface reactivity. Combining this application with computational modeling is a powerful way to investigate changes in the electronic structure of mineral surfaces in the context of contaminant adsorption. Furthermore, the work function of a material (which is related to surface potential) is quite often described in the literature as a single value; however, it is more likely that this parameter varies laterally with the surface structure of a surface, a concept that can be explored further with KPFM. Although limited to scanning surfaces in air, KPFM may be a useful for studying other processes that depend on the charge of a mineral surface, such as cation exchange capacity in soils, flotation processes in mineral separation, and electrokinetic decontamination of soils.

In summary, this thesis has developed new methods that the geochemical community will be able to use to study the properties of mineral surfaces in the presence of dissolved contaminants in solution.